The Precambrian-Cambrian (R)Evolution – Insights from the Kazakh Microcontinent

Author:

Jessica Alexandra STAMMEIER

Supervisor	Ass. Prof. Dr. Dorothee Hippler
	Graz University of Technology
	Institute of Applied Geosciences
	Rechbauerstrasse 12
	8020 Graz
	Austria
Primary Reviewer	Univ.-Prof. Dr. Martin Dietzel
	Graz University of Technology
	Institute of Applied Geosciences
	Rechbauerstrasse 12
	8010 Graz
	Austria
Secondary Reviewer	Dipl. Chem. Dr. Albrecht Leis
	JR-AquaConSol GmbH
	Steyrergasse 21
	8010 Graz
	Austria
Tertiary Reviewer	Univ.-Prof. Dr. Oliver Nebel
	Monash University
	School of Earth, Atmosphere and Environment
	Clayton/Melbourne
	Victoria 3800
	Australia

Statutory Declaration

I, Jessica Alexandra STAMMEIER, declare that I have authored this thesis titled, "The Precambrian-Cambrian (R)Evolution – Insights from the Kazakh Microcontinent" and the work presented independently, and that I have not used other than the declared sources/ resources, and that I have explicitly marked all material which has been quoted either literally or by content from the used sources. The text document uploaded to TUGRAZonline is identical to the printed version.

_____   _____

Signature   Date

Eidesstattliche Erklärung

Ich, Jessica Alexandra STAMMEIER, erkläre an Eides statt, dass ich die vorliegende Arbeit mit dem Titel, "The Precambrian-Cambrian (R)Evolution – Insights from the Kazakh Microcontinent" selbstständig verfasst, andere als die angegebenen Quellen/ Hilfsmittel nicht benutzt, und die den benutzten Quellen wörtlich und inhaltlich entnommenen Stellen als solche kenntlich gemacht habe. Das in TUGRAZonline hochgeladene Textdokument ist mit der vorliegenden Dissertation identisch.

_____   _____

Signature   Date

*"Es ist nicht das Wissen, sondern das Lernen,
nicht das Besitzen, sondern das Erwerben,
nicht das Dasein, sondern das Hinkommen,
was den größten Genuß gewährt."*

Carl Friedrich Gauss

GRAZ UNIVERSITY OF TECHNOLOGY

Abstract

The Precambrian-Cambrian (R)Evolution – Insights from the Kazakh Microcontinent

by Jessica Alexandra STAMMEIER

The Precambrian-Cambrian transition is a critical period in Earth's history, marking a global bio-geochemical revolution that culminates in an unique bio-radiation. This revolutionary period is characterized by extreme geodynamic and vital changes, such as continental re-organization, progressive oxygenation, enhanced element cycling, novel biomineralization, agronomic changes and evolutionary leaps. Yet, despite decades of research, causal relations and respective timing remain a matter of debate. This study focuses on early Cambrian phosphate-rich sedimentary sequences from Kazakhstan as a key archive for paleo-environmental reconstruction.

For the investigated location, a continuous chemical (main, trace and rare earth elements), radiogenic and stable isotope record ($^{87}Sr/^{86}Sr$, $\delta^{13}C$, $\delta^{18}O$, $\delta^{26}Mg$) across the Pc-C transition is presented. Trace and ΣREE contents and a linear co-variation of $\delta^{13}C$ and $\delta^{18}O$ characterize these sedimentary samples as near-primary shallow-water deposits. The investigated samples record the basal Cambrian negative $\delta^{13}C$ excursion. $^{87}Sr/^{86}Sr$ values are similar to the global seawater $^{87}Sr/^{86}Sr$ system, implying that paleo-Kazakhstan was part of the global seawater evolution. $^{87}Sr/^{86}Sr$ from this study together with literature data produces a refined seawater $^{87}Sr/^{86}Sr$ evolution, highlighting a distinct positive $^{87}Sr/^{86}Sr$ excursion at the Precambrian-Cambrian boundary at ca. 541 Ma. Together with high $\delta^{26}Mg$ signatures this indicates a time of enhanced crustal reworking during the Gondwana assembly. The observed isotope excursions are of relatively short duration and unprecedented in the geologic record. In conclusion it seems plausible, that an unprecedented collision of continental landmass during the Gondwana assembly caused a period of extreme continental reworking of evolved continental crust. The associated release of nutrients caused the formation of massive phosphorite deposits and ultimately led to a sudden change in marine biota.

The analytical procedure for analysis of Mg and Sr isotopes was validated in a parallel study by analyzing several certified reference materials for their respective isotope composition. The study included element separation and subsequent analysis and yielded an intermediate precision of -2.64 ± 0.10 ‰ of $\delta^{26}Mg$ for CAM-1 (2s, n=23), and 0.709197 ± 0.000011 of $^{87}Sr/^{86}Sr$ for seawater (2s, n=19). Additionally, a set of combined stable Mg and radiogenic Sr isotope values for certified reference materials SARM 43, SRM 1B, and SRM 88A, and radiogenic Sr isotope values for SARM 40 are presented.

x

Kurzfassung

Die Precambrisch-Cambrische (R)Evolution – Einblicke aus Kazakhstan

von Jessica Alexandra STAMMEIER

Der Prekambrisch-Kambrische Übergang stellte eine kritische Phase der Erdgeschichte dar. Er markiert eine globale biologische-geologische Revolution, die in einer einzigartigen biologischen Diversifikation endet. Diese revolutionäre Zeit ist charakterisiert von extremen geodynamischen und umweltbezogenen Veränderungen, so wie kontinantale Re-organisation, fortschreitende Oxygenierung, Verbesserung der Elementkreisläufe und Biomineralisation, sowie agronomische Veränderungen und evolutionäre Sprünge. Doch trotz jahrzehntelanger Forschung sind die kausalen Beziehungen und das jeweilige Timing immer noch nicht klar. Die vorliegende Studie untersucht phosphatreiche Sedimente aus dem frühen Kambrium aus Kasachstan als Schlüsselarchiv für Paläoumwelt-Rekonstruktionen. Für das untersuchte Studiengebiet wird ein umfassender Datensatz von Proben entlang des Prekambrisch- Kambrischen Übergangs präsentiert, mit Haupt-, Spurenelementen, inklusive seltener Erden (SEE), so wie radiogenen und stabilen Isotopen (^{87}Sr/^{86}Sr, δ^{13}C, δ^{18}O, δ^{26}Mg). Spuren- und ΣSEE-Gehalte, so wie eine lineare Co-Variation von δ^{13}C und δ^{18}O charakterisieren diese sedimentären Proben als nahezu unveränderte Flachwasserablagerungen. Die untersuchten Proben erfassen die basale Kambrische negative δ^{13}C Exkursion. Die ^{87}Sr/^{86}Sr Werte sind ähnlich der globalen ^{87}Sr/^{86}Sr Meerwasserentwicklung, was darauf hindeutet, dass Paleo-Kasachstan Teil der globalen (Meerwasser-) Entwicklung war. ^{87}Sr/^{86}Sr aus dieser Studie wurden mit ^{87}Sr/^{86}Sr aus der Literatur kombiniert und eine neue, verfeinerte Meerwasser ^{87}Sr/^{86}Sr -Entwicklung konstruiert. Diese zeigt eine deutliche positive ^{87}Sr/^{86}Sr - Exkursion an der Prekambrium- Kambrium Grenze vor ca. 541 Ma. Zusammen mit ebenfalls hohen δ^{26}Mg - Signaturen deutet dies auf eine Zeit verstärkter Krustenaufarbeitung während der Gondwana-Assimilierung hin. Die positiven Exkursionen bei den Isotopendaten sind von relativ kurzer Dauer und erstmalig in der geologischen Geschichte. Zusammenfassend scheint es plausibel, dass eine Kollision der kontinentalen Landmassen während der Gondwana-Assimilierung eine Periode extremer, kontinentaler Krustenaufarbeitung von alter, kontinentalen Kruste verursachte. Die damit verbundene Freisetzung von Nährstoffen begünstigte die Formation massiver Phosphorit Vorkommen und führte schließlich zu der plötzlichen Veränderung der Meeresbiota.

In einer Parallelstudie wurde das analytische Verfahren zur Bestimmung von Mg und Sr Isotopen überprüft indem die Isotopenzusammensetzung von mehreren zertifizierten Referenzmaterialien analysiert wurde. In dieser Studie wurden sowohl die

Elementseparation als auch die darauf folgende Messung getestet. Die gemittelte Prezision ergab eine Genauigkeit von -2.64 ± 0.10 ‰ δ^{26}Mg für CAM-1 (2s, n = 23) und 0.709197 ± 0.000011 ^{87}Sr/^{86}Sr für Meerwasser (2s, n = 19). Zusätzlich wurde ein Datensatz mit Mg und Sr Isotopenwerte für die Referenzmaterialien SARM 43, SRM 1B und SRM 88A und radiogene Sr Isotopenwerte für SARM 40 präsentiert.

Acknowledgements

Contents

List of Figures

List of Tables

Dedicated to my Family

Chapter 1

Introduction

1.1 The Precambrian-Cambrian Transition

The Precambrian-Cambrian (Pc-C) transition is a key interval for the biologic evolution in Earth's history (Morris, 2006; Geyer and Landing, 2017; Marshall, 2006; Shu, 2008). The Pc-C boundary marks the transition from the Neoproterozoic Ediacaran period to the Phanerozoic Cambrian period. The boundary is defined by the first appearance datum (FAD) of the trace fossil *Treptichnus/Trichophycus pedum* (Landing, 1994) at the type location Fortune Head, Newfoundland, Canada (Brasier, Corfield, et al., 1994) and set to 541 ± 1.0 Ma (Cohen et al., 2013).

The Cambrian is characterized by an extensive ecosphere revolution. This is accompanied by the stepwise increase in animal diversity that commences with the occurance of small shelly fossils (SSF) and culminates in the so called "Cambrian Explosion". This "explosion" refers to the unique radiation of Cambrian fauna, in which a rapid diversification and the evolution of metazoan life took place (Morris, 1989). This radiation follows the mass extinction of the Ediacaran fauna and drastic changes to the ecosystem (X. Zhang et al., 2014). The Ediacaran fauna consists of simple, soft-bodied and mostly immobile organisms (Darroch et al., 2015). They feed on microbial mats that seal the underlying sediment from a mostly anoxic to euxinic ocean (Fox, 2016). With the beginning of the Cambrian this ecosystem gains complexity. The Ediacaran fauna gives way to complex, skeletal metazoans (R. Wood and Zhuravlev, 2012). Along with the innovation of predation, biomineralization and improved bioturbation, they colonize the sediment and pelagic zones in a progressively oxidized ocean (Wallace et al., 2017; Wang et al., 2012).

The Pc-C transition is set in the aftermath of several (global) glaciations that caused massive perturbation to carbon cycling in the Ediacaran (Kaufman, Knoll, and Narbonne, 1997; Kasemann et al., 2014; Young, 2015). Among the most prominent glaciations are the Sturtian (740-700 Ma), Marinoan (665-635 Ma) und Gaskiers glaciation (ca. 580 Ma, M. Zhu, J. Zhang, and Yang, 2007; Kaufman, Knoll, and Narbonne, 1997; Halverson et al., 2010). At the same time, continental fragments, remnants of the break-up of the supercontinent Rodinia (ca. 750 Ma), re-organized to form the next supercontinent Gondwana (ca. 540 Ma, Maruyama et al., 2014). This

continent amalgamation is accompanied by several orogenic events, e.g., Pan-African orogeny (650-500 Ma, Miller, 1983) and Cadomian orogeny (750-540 Ma, Linnemann et al., 2014). Both events, glaciations and continental re-organization, contributed to a significant rise of weathering and erosion rates during the Neoproterozoic (Halverson et al., 2010; Kasemann et al., 2014).

Whether an individual cause or a combination of several causes triggered this explosion of life has yet to be determined. Hypotheses are diverse and include evolutionary, ecologic and/or geologic/geochemical theories (Fox, 2016; Smith and Harper, 2013; X. Zhang et al., 2014). Among the geologic processes, enhanced weathering is one of the most dominant forces in the Late Neoproterozoic, e.g., recorded by the steady increase in seawater $^{87}Sr/^{86}Sr$ (Halverson et al., 2010). High seawater $^{87}Sr/^{86}Sr$ values indicate enhanced contribution from old continental crust, while low $^{87}Sr/^{86}Sr$ values are derived from hydrothermal alteration. Further, the role and respective timing of oceanic and atmospheric oxygenation remains a matter of hot debate. Theories include that (i) bottom waters remained anoxic until the Cambrian period (Sperling et al., 2015); a (ii) intermittent, stepwise oxygenation began well before the Pc-C transition (Lyons, Reinhard, and Planavsky, 2014; Tostevin et al., 2016); and (iii) oxygen levels were already elevated above a certain threshold before the Pc-C boundary (Canfield, Poulton, and Narbonne, 2007; Mills and Canfield, 2014). Studies focused on paleo-microcontinents that were situated at low-latitudes, including locations on the Siberian craton (e.g., Derry et al., 1994; Brasier, Corfield, et al., 1994), Tarim block (e.g., C. L. Zhang et al., 2013; Dong et al., 2009), and South China block (incl. Yangtze platform; e.g., Pirajno, 2013; Weber, Steiner, and M. Y. Zhu, 2007; Li, 2010), India (e.g., Banerjee et al., 1997; Franz et al., 2014), Kazakhstan (e.g., Weber, Steiner, Evseev, et al., 2013; Dzik, 2003) and Namibia (e.g., R. A. Wood, Grotzinger, and Dickson, 2002; Geyer, 2005), covering locations all over the world. The stratigraphic correlation of Neoproterozoic to Cambrian strata of these locations is well constrained by stratigraphic similarities (e.g., Levashova, Kalugin, et al., 2010, and references therein), chemostratigraphy (e.g., Halverson et al., 2010) and fossil assemblages (e.g., Brasier, 1982).

1.2   Study Area

Among the above mentioned key locations of the Pc-C location Kazakhstan constitutes a promising study section for Early Cambrian strata. Up to the present day, Kazakhstan holds massive minable phosphorous occurrences distributed in 45 deposits located in the NE part of the Karatau mountain range (see below, Levine, 2011). This phosphate rock is mainly used for fertilizer production. However, the mining industry broke down about 25 years ago, leaving several, easily accessible open pit mines.

The Karatau mountain range is located in south Kazakhstan and stretches in NW-SE direction and is part of the Central Asian Orogenic Belt (CAOB). The post-Cambrian Main Karatau Fault (<480 Ma, Allen, Alsop, and Zhemchuzhnikov, 2001) divides the mountain range into the NE Malyi Karatau and the SW Bolshoi Karatau. The Malyi Karatau comprises well-preserved Pc-C strata that is considered to have undergone few thermal and tectonic events (Alexeiev et al., 2009; Heubeck, Ergaliev, and Evseev, 2013; Weber, Steiner, Evseev, et al., 2013). The herein investigated Koksu section is located in the Malyi Karatau, few kilometres from Zhanatas (Figure 1.1).
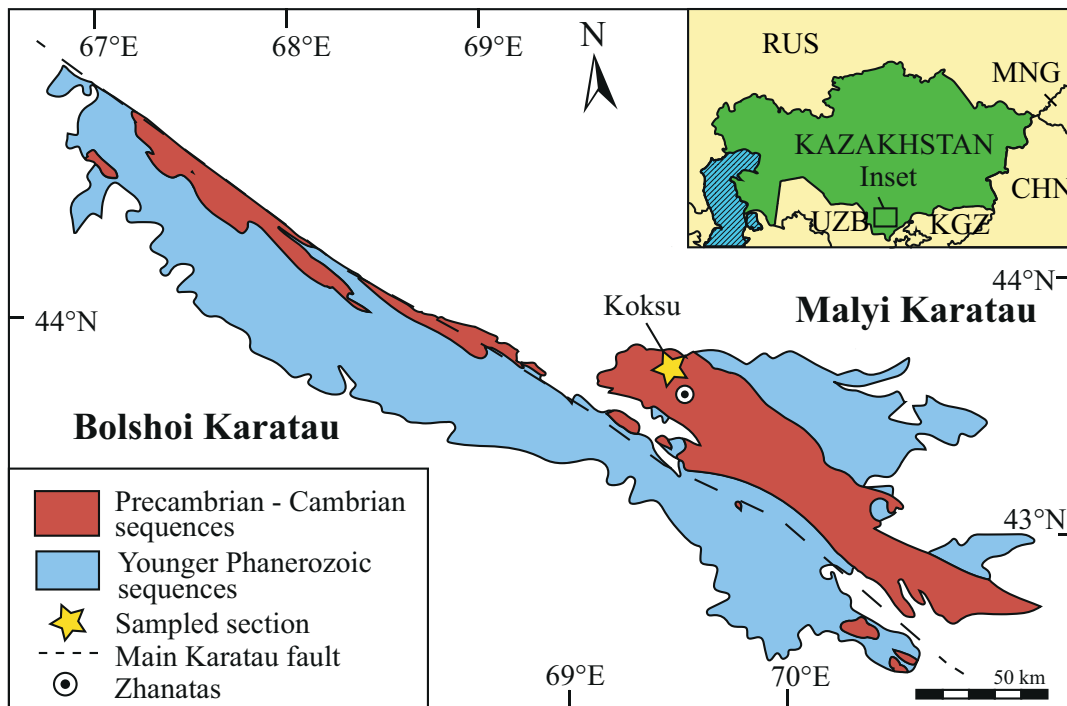
FIGURE 1.1: Schematic geologic map of the Malyi and Bolshoi Karatau Mountain range located in southern Kazakhstan (simplified after Eganov and Sovetov, 1986). The investigated Koksu sections is located at the margin of a former shallow water basin (Eganov, Sovetov, and Yanshin, 1986).

The exact paleogeographic position of the Kazakh microcontinent is subject to discussion for the Ediacaran and Cambrian time. Estimates for the mid- Neoproterozoic (ca. 770 Ma) suggest a paleolatitude of ca. 34°N or S (Levashova, Meert, et al., 2011). Weber, Steiner, Evseev, et al. (2013) propose that during the early Cambrian period the microcontinent was positioned in between 20°N and 20°S. These views are supported by the apparent similarities of ichnofacies and depositional environments of the Kazakh microcontinent and the Yangtze platform (Li et al., 2013; Weber, Steiner, Evseev, et al., 2013), which was positioned at ca.15-30°S (Baojun and Sitian, 1997).

The investigated Koksu section is located in one of the former open pit mines. The stratigraphic and fossiliferous record and the thermal history of the Koksu section have previously been described by Weber, Steiner, Evseev, et al. (2013) and Heubeck,

Ergaliev, and Evseev (2013). These works describe the sedimentary record including ichno assemblages and establish stratigraphic correlation with the well-investigated Yangtze platform. At Koksu, a ca. 50 m exploration trench provides access to a continuous record of the Chuluktau Formation (Fm.), which constitutes the earliest Cambrian period. The Chuluktau Fm. comprises a succession of shallow water sediments, including from base to top (1) Aksai Chert, (2) Lower Phosphorite, (3) Shale Member, (4) Upper Phosphorite, (5) Fe-Mn Horizon, and (6) Brown Dolomite (Heubeck, Ergaliev, and Evseev, 2013). The Chert horizon comprises dark-coloured bedded cherts, siliceous sedimentary rocks, with thin layers of mudstone phosphorite. The phosphorite horizons consist of siliceous mudstone to grainstone phosphorite. While the Lower Phosphorite (P_1C) has a dolomite matrix, the Upper Phosphorite (P_2C) has a phosphatic matrix. The latter has several conglomeratic phosphorite layers, indicating an increase of depositional energy towards the upper part of the profile. The intercalated Shale Member consists of thinly layered siliceous siltstones with phosphatic interlayers. The Upper Phosphorite is followed by a dolomite horizon with abundant Fe-Mn crusts, and topped by a dolostone horizon.

1.3   Phosphorites in a Nutshell

One of the sedimentological key features of the Pc-C transition is the widespread occurrence of phosphorite deposits. Phosphorites (s.s.) are sedimentary deposits with >18. wt. % P_2O_5 (whole rock; Jarvis et al., 1994). The main P-bearing mineral phase is Carbonate-Fluorapatite (CFA, sometimes also referred to as francolite). The mineral CFA is part of the apatite group, with abundant F and CO_3 and the chemical formular $Ca_5(PO_4,CO_3)_3F$. Common paragenetic mineral assemblages are silicates, silica, carbonates and organic matter (Trappe, 1998). Classification of phosphorites is based on the carbonate classification of Dunham (1962) which was developed by Cook and colleagues and published in Cook and Shergold (1986). Element substitution and incorporation of the respective isotope composition, e.g., REE, $\delta^{13}C$, $^{87}Sr/^{86}Sr$ is common. Geochemical and isotope analysis of the sediments thus allow reconstruction of the depositional environment.

Sedimentary phosphorites usually form at the sediment-water interface in (epi-) continental shelf settings (Föllmi, 1996). Trappe (1998) distinguished two main processes of phosphorite formation: (1) phosphogenesis, and (2) phosphorite genesis. The former refers to primary processes resulting in authigenic (orthochemical) phosphate precipitation, the latter to secondary mechanisms producing clastic (allochemical) phosphate grains. Generally speaking, primary processes occur through P concentration and subsequent precipitation due to apatite supersaturation, either as an

inorganic process or through microbial mediation. Mechanisms involved in this process include the (i) "iron redox pump", referring to the transport of P absorbed on iron (hydr-) oxides through a redox barrier and the release of P during iron reduction (Crosby and Bailey, 2012); (ii) accumulation of polyphosphates by sulfide-oxidizing or sulfate-reducing bacteria in cell-vacuoles and the subsequent release to ambient pore waters (H. N. Schulz and H. D. Schulz, 2005; Goldhammer et al., 2010; Arning, Birgel, et al., 2008); (iii) extracellular conditions such as influences on pH, nucleation sites or charged cell walls (Ferris, 1989). These primary processes usually occur in sediment pore fluids, on microbial mats or associated extrapolymeric substances (EPS) or as concretionary growth. Secondary processes are those that mechanically rework authigenic sediments. This may occur though (a) sediment reworking, (b) winnowing, or (c) phosphatization of allochemical minerals, with either carbonate or phosphate composition (Sheldon, 1981; Trappe, 1998).

The exact mechanisms involved in phosphogenesis in either modern or ancient phosphorites still remain a matter of hot debate (e.g.: Bailey et al., 2007; Crosby and Bailey, 2012). For example, recent studies suggest that precipitation of apatite minerals occurs via a metastable amorphous phase (LeGeros, 1993; Kim et al., 2005). Investigations of the stability and kinetics of such transient phases open up new perspectives on e.g. mineral or fossil preservation (Arning, Lückge, et al., 2009). Further, while in modern phosphorites the active role of microbes such as sulfur-bacteria is certain, in ancient phosphorites their role remains controversial. However, microfossils and fossilized microbial mats e.g.: found in Proterozoic phosphorites from South China suggest microbes play an important and active role during the Pc-C phosphogenic event (Bailey et al., 2007; Crosby and Bailey, 2012).

The oldest phosphorite deposits are documented from the Paleoproterozoic (Baturin, 1982; Papineau, 2010; Lepland et al., 2013). Proterozoic phosphorites are mostly composed of microbial mats and are often associated with Fe-Mn concretions and pyrite (Baturin, 1982). However, their occurrence is limited. Deposition of so called "phosphate giants" (cf. Trappe, 1998), i.e., large quantities of mineable, sedimentary phosphorite, begins with the Pc-C transition (Cook and Shergold, 1986; Shen, Schidlowski, and Chu, 2000; Brasier, Magaritz, et al., 1990). The Phanerozoic is marked by several of such global phosphogenic events (Cook and Shergold, 1986; Cook and Shergold, 1984; Föllmi, 1996). The first and possibly largest one was deposited during the Cambrian (Cook and McElhinny, 1979; Trappe, 1998), concomitant with the rise of metazoan life. Thus, Cambrian phosphorites are an important archive of this biologic revolution, as they constitute the link between bio- and geosphere.

1.4   Research Goals and Concept

1.4.1   Research goals

This PhD project is an extension of the DFG research group 736 (DFG FOR 736), entitled "Precambrian- Cambrian ecosphere (R)Evolution: Insights from Chinese Microcontinents". This Sino-German research project aims to decipher the evolutionary developments and environmental processes that lead to the ecologic revolution at the Pc-C boundary (Fatka et al., 2012). The tasks of this project therefore comprise a multidisciplinary approach on sedimentary sequences of key localities on the Yangtze platform.

As an attributed project, the scope of the current PhD project is extended to the Kazakh microcontinent. The thesis focuses on the geochemical reconstruction of Cambrian seawater and paleoenvironments in the light of geological processes that contribute to the "Precambrian- Cambrian ecosphere (R)Evolution". Samples were provided by Ass. Prof. D. Hippler and were collected prior to this PhD project in two field trips in 2010 and 2011. For geochemical analysis, a subset of samples was selected, comprising representative samples from early Cambrian strata.

Kazakhstan was chosen as a study area as it provides access to well exposed Pc-C sedimentary records including several Cambrian phosphorite deposits. During the Pc-C transition the paleo-microcontinent was in juxtaposition with the well investigated Yangtze platform. This justifies a comparison of the paleo-environmental condition of both paleo-microcontinents (compare section 1.2).

The overall research goal of this study is to constrain the depositional environment in which these Cambrian sequences were deposited. This was evaluated by investigating the geochemical composition of the samples, including main, trace and rare earth elements. Further, these local findings are correlated with related paleo-continents to construct a common $^{87}Sr/^{86}Sr$ seawater evolution. The results were placed in a broader geographic context in order to identify a critical global event driving the Cambrian ecosphere revolution.

1.4.2   Concept

To achieve the above research goals (section 1.4.1), the samples are analysed for their element and isotope composition. Element analyses are conducted on an ICP OES (Main elements) and ICP MS (trace and REE). Radiogenic Sr isotopes and non-traditional stable Mg isotopes are performed after chemical separation on a MC-ICP

MS. For method validation, separation protocols are developed and tested by chemically separating and subsequently measuring Sr and Mg isotopes of several carbonate bearing certified reference materials. These results are presented in chapter 2.

In order to justify drawing legitimate conclusions from old (>500 Ma) sedimentary samples it is crucial to ensure chemical preservation. An initial evaluation of the petrographic and mineralogical preservation of the samples was conducted during the course of a bachelor thesis prior to this PhD project. The results of this bachelor work characterized these samples as petrographically (near-) pristine with primary internal structures. On the basis of this, further geochemical investigations were conducted. All chemical analyses are performed on the acid soluble fraction (asf) of the samples. This asf represents the phosphate and carbonate fraction and excludes siliceous fractions. Chemical preservation was evaluated by investigating rare earth and trace elemental compositions, stable oxygen and carbon isotopes. Further, two exemplary samples are investigated in detail for their element and Sr isotope distribution among the different mineral phases. This is achieved by collecting quantitative element distribution images by electron microprobe analysis (EMPA). The Sr isotope distribution is determined by a two-step leaching study, in which contribution of post-sedimentary calcite veins or cements are separated from syn-sedimentary phosphate phases. The findings of this are discussed in detail in section 3.5.1 "diagenetic constraints" of chapter 3.

(Near-) pristine samples justify further evaluation of the Sr isotope composition of the samples. The Sr isotope composition of sedimentary carbonate and phosphate samples captures the Sr composition of the seawater during deposition. The Sr composition of the global ocean is considered to be homogenous. Thus, Sr isotope results can be used to reconstruct a global $^{87}Sr/^{86}Sr$ seawater evolution. For this study, literature data is compiled and added to the results from the present study in order to construct a refined $^{87}Sr/^{86}Sr$ seawater evolution for the Pc-C transition. These results are presented in chapter 3.

In order to identify causes that impact the habitability of marine environments, perturbations to global elements cycling has to be considered. To distinguish different influences on the seawater composition, a time-dependent dynamic state box-model is developed. This model is tested employing two fundamentally different isotope systems with different properties: (i) stable Mg-isotopes are sensible to kinetic fractionation, and (ii) radiogenic Sr isotopes are sensible to provenance of Sr. The model thus reveals quantitative and qualitative information about flux imbalances between continental and ocean reservoirs. These results are presented in chapter 4.

In two parallel and independent studies inorganic precipitation experiments are conducted. In these projects, inorganic precipitation of Ca-phosphates are monitored. These experiments were designed in order to contribute to the understanding of transformation kinetics and precipitation mechanisms of Ca-P mineral phases. Information about the precipitated mineral, such as composition or shape may help to identify different formation mechanisms involved in natural surroundings. The conditions of the experiments are chosen in order to resemble simplified Cambrian seawater. In this manner, observations from these experiments can be compared to natural sediments. In the first study, the experiment is performed in solution and monitored *in-situ* using Raman Spectroscopy. This experiment is conducted in order to monitor the stability of the precursor phase. The stability of transient phases is crucial to the preservation of phosphatic minerals, either fossils or in inorganic sediments. This experiment is presented in chapter 6. In the second set of experiments, precipitation is induced in a gel medium in the presence of different elemental additives. This is designed to resemble Ca-P precipitation within microbial mats. Microbial mats covered the seafloor during the Pc-C transition and are thought to constitute media for phosphogenesis. These experiments were performed during a COST STSM grant at the Institute of Chemistry, University of Potsdam. The results of this are presented in the official *Scientific Exchange report (STSM)* report in Appendix D.

During the course of this PhD project, a contribution to the Encyclopedia of Geochemistry, a book by Springer International Publishing is made. This Encyclopedia is 'A Comprehensive Reference Source on the Chemistry of the Earth' (White, 2017) that contains chapters on relevant geochemical topics. For this Encyclopedia, a chapter on Sr isotopes is written, in which different aspects and applications of Sr isotopes in geosciences are described. This chapter, entitled *Strontium Isotopes* is introduced in chapter 5 and attached in appendix C.

The main findings of this PhD thesis are reported in chapter 2, chapter 3, chapter 4, chapter 5 and chapter 6. All of these chapters are prepared as manuscripts for publication in scientific journals. Chapter 3 and chapter 6 have been submitted and are currently under review. Chapter 2 and chapter 4 will be submitted shortly. Chapter 5 has already been published in the Encyclopedia of Geochemistry in January 2016.

References

Alexeiev, D. V., H. E. Cook, V. M. Buvtyshkin, and L. Y. Golub (2009). "Structural evolution of the Ural–Tian Shan junction: A view from Karatau ridge, South Kazakhstan". In: *Comptes Rendus Geoscience* 341. DOI: 10.1016/j.crte.2008.12.004.

Allen, M. B., G. I. Alsop, and V. G. Zhemchuzhnikov (2001). "Dome and basin refolding and transpressive inversion along the Karatau Fault System, southern Kazakstan". In: *Journal of the Geological Society* 158. DOI: 10.1144/jgs.158.1.83.

Arning, E. T., a. Lückge, C. Breuer, N. Gussone, D. Birgel, and J. Peckmann (2009). "Genesis of phosphorite crusts off Peru". In: *Marine Geology* 262. DOI: 10.1016/j.margeo.2009.03.006.

Arning, E. T., D. Birgel, H. N. Schulz-Vogt, L. Holmkvist, B. B. Jorgensen, A. Larson, and J. Peckmann (2008). "Lipid Biomarker Patterns of Phosphogenic Sediments from Upwelling Regions". In: *Geomicrobiology Journal* 25. DOI: 10.1080/01490450801934854.

Bailey, J. V., S. B. Joye, K. M. Kalanetra, B. E. Flood, and F. a. Corsetti (2007). "Evidence of giant sulphur bacteria in Neoproterozoic phosphorites". In: *Nature* 445. DOI: 10.1038/nature05457.

Banerjee, D. M., M. Schidlowski, F. Siebert, and M. D. Brasier (1997). "Geochemical changes across the Proterozoic-Cambrian transition in the Durmala phosphorite mine section, Mussoorie Hills, Garhwal Himalaya, India". In: *Palaeogeography, Palaeoclimatology, Palaeoecology* 132. DOI: 10.1016/S0031-0182(97)00060-6.

Baojun, L. and L. Sitian (1997). *Proceedings of the 30th International Geological Congress : Beijing, China, 4-14 August 1996.* Ed. by L. Baojun and L. Sitian. Utrecht: International Geological Congress, p. 225.

Baturin, G. N. (1982). *Phosphorites on the sea floor : origin, composition, and distribution.* Elsevier Scientific, p. 343.

Brasier, M. D. (1982). "Sea-level changes, facies changes and the late Precambrian—Early cambrian evolutionary explosion". In: *Precambrian Research* 17. DOI: 10.1016/0301-9268(82)90050-X.

Brasier, M. D., R. M. Corfield, L. A. Derry, A. Y. Rozanov, and A. Y. Zhuravlev (1994). "Multiple δ13C excursions spanning the Cambrian explosion to the Botomian crisis in Siberia". In: *Geology* 22. DOI: 10.1130/0091-7613(1994)022<0455:MCESTC>2.3.CO;2.

Brasier, M. D., M. Magaritz, R. Corfield, L. Huilin, W. Xiche, O. Lin, J. Zhiwen, B. Hamdi, H. Tinggui, and A. G. Fraser (1990). "The carbon- and oxygen-isotope record of the Precambrian–Cambrian boundary interval in China and Iran and their correlation". In: *Geological Magazine* 127. DOI: 10.1017/S0016756800014886.

Canfield, D. E., S. W. Poulton, and G. M. Narbonne (2007). "Late-Neoproterozoic deep-ocean oxygenation and the rise of animal life." In: *Science (New York, N.Y.)* 315. DOI: 10.1126/science.1135013.

Cohen, K. M., S. C. Finney, P. L. Gibbard, and J. X. Fan (2013). "The ICS International Chronostratigraphic Chart". In: *Episodes* 36.

Cook, P. J. and M. W. McElhinny (1979). "A reevaluation of the spatial and temporal distribution of sedimentary phosphate deposits in the light of plate tectonics". In: *Economic Geology* 74. DOI: `10.2113/gsecongeo.74.2.315`.

Cook, P. J. and J. H. Shergold (1984). "Late Proterozoic - Cambrian Phosphorites and Phosphogenesis". In: *Non-Metallic Mineral Ores*. Ed. by P. J. Cook and J. H. Shergold. Canberra: VNU Science Press, pp. 397–444.

– (1986). "Phosphate Deposits of the World. Volume 1. Proterozoic and Cambrian Phosphorites". In: *Geological Magazine*. Ed. by P. J. Cook and J. H. Shergold. Vol. 124. Cambridge: Cambridge University Press, p. 487. DOI: `10.1017/S0016756800017106`.

Crosby, C. H. and J. V. Bailey (2012). "The role of microbes in the formation of modern and ancient phosphatic mineral deposits". In: *Frontiers in Microbiology* 3. DOI: `10.3389/fmicb.2012.00241`.

Darroch, S. A. F., E. A. Sperling, T. H. Boag, R. A. Racicot, S. J. Mason, A. S. Morgan, S. Tweedt, P. Myrow, D. T. Johnston, D. H. Erwin, and M. Laflamme (2015). "Biotic replacement and mass extinction of the Ediacara biota". In: *Proceedings of the Royal Society B: Biological Sciences* 282. DOI: `10.1098/rspb.2015.1003`.

Derry, L. A., M. D. Brasier, R. Corfield, A. Y. Rozanov, and A. Zhuravlev (1994). "Sr and C isotopes in Lower Cambrian carbonates from the Siberian craton: A paleoenvironmental record during the 'Cambrian explosion'". In: *Earth and Planetary Science Letters* 128. DOI: `10.1016/0012-821X(94)90178-3`.

Dong, L., S. Xiao, B. Shen, C. Zhou, G. Li, and J. Yao (2009). "Basal Cambrian Microfossils from the Yangtze Gorges Area (South China) and the Aksu Area (Tarim Block, Northwestern China)". In: *Journal of Paleontology* 83. DOI: `10.1666/07-147r.1`.

Dunham, R. J. (1962). *Classification of Carbonate Rocks According to Depositional Textures*, pp. 108–121. DOI: `10.1306/M1357`. arXiv: `arXiv:0807.1760v1`.

Dzik, J. (2003). "Early Cambrian lobopodian sclerites and associated fossils from Kazakhstan". In: *Palaeontology* 46. DOI: `10.1111/1475-4983.00289`.

Eganov, E. A., K. Y. Sovetov, and A. L. Yanshin (1986). "Proterozoic and Cambrian phosphorite deposits: Karatau, southern Kazakhstan, USSR". In: *Phosphate Deposits of the World*. Ed. by P. J. Cook and J. H. Shergold. Vol. 1. Cambridge University Press, pp. 175–189.

Fatka, O., M. Steiner, B. Weber, and M. Zhu (2012). "The Precambrian-Cambrian biosphere (r)evolution: Insights from the Chinese Yangtze Platform". In: *Bulletin of Geosciences* 87. DOI: `10.3140/bull.geosci.1346`.

Ferris, F. G. (1989). "Metallic ion interactions with the outer membrane of gram-negative bacteria". In: *Metal Ions and Bacteria*. Ed. by T. J. Beveridge and R. J. Doyle. New York: Wiley.

Föllmi, K. (1996). "The phosphorus cycle, phosphogenesis and marine phosphate-rich deposits". In: *Earth-Science Reviews* 40. DOI: 10.1016/0012-8252(95)00049-6.

Fox, D. (2016). "What sparked the Cambrian explosion?" In: *Nature* 530. DOI: 10.1038/530268a.

Franz, G., D. Hippler, D. Rhede, R. Wirth, D. M. Banerjee, and N. Mahlstedt (2014). "Diagenetic formation of interlayer-deficient fluorophlogopite as a clay mineral in Early Cambrian phosphorite (Lesser Himalaya, India): The trioctahedral analog of illite". In: *American Mineralogist* 99. DOI: 10.2138/am-2014-4852.

Geyer, G. (2005). "The Fish River Subgroup in Namibia: Stratigraphy, depositional environments and the Proterozoic-Cambrian boundary problem revisited". In: *Geological Magazine* 142. DOI: 10.1017/S0016756805000956.

Geyer, G. and E. Landing (2017). "The Precambrian–Phanerozoic and Ediacaran–Cambrian boundaries: a historical approach to a dilemma". In: *Geological Society, London, Special Publications* 448. DOI: 10.1144/SP448.10.

Goldhammer, T., V. Brüchert, T. G. Ferdelman, and M. Zabel (2010). "Microbial sequestration of phosphorus in anoxic upwelling sediments". In: *Nature Geoscience* 3. DOI: 10.1038/ngeo913.

Halverson, G. P., B. P. Wade, M. T. Hurtgen, and K. M. Barovich (2010). "Neoproterozoic chemostratigraphy". In: *Precambrian Research* 182. DOI: 10.1016/j.precamres.2010.04.007.

Heubeck, C., G. Ergaliev, and S. Evseev (2013). "Large-Scale Seismogenic Deformation of A Carbonate Platform Straddling the Precambrian-Cambrian Boundary, Karatau Range, Kazakhstan". In: *Journal of Sedimentary Research* 83. DOI: 10.2110/jsr.2013.76.

Jarvis, I., W. C. Burnett, Y. Nathan, F. S. M. Almbaydin, A. K. M. Attia, L. N. Castrol, R. Flicoteaux, M. E. Hilmy, V. Husain, A. Qutawna, A. Serjani, and Y. N. Zanin (1994). "Phosphorite geochemistry: state-of-the-art and environmental concerns". In: *Eclogae geologicae Helvetiae* 87.

Kasemann, S. A., P. A. Pogge von Strandmann, A. R. Prave, A. E. Fallick, T. Elliott, and K. Hoffmann (2014). "Continental weathering following a Cryogenian glaciation: Evidence from calcium and magnesium isotopes". In: *Earth and Planetary Science Letters* 396. DOI: 10.1016/j.epsl.2014.03.048.

Kaufman, A. J., A. H. Knoll, and G. M. Narbonne (1997). "Isotopes, ice ages, and terminal Proterozoic earth history". In: *Proceedings of the National Academy of Sciences* 94. DOI: 10.1073/pnas.94.13.6600.

Kim, S., H.-S. Ryu, H. Shin, H. S. Jung, and K. S. Hong (2005). "In situ observation of hydroxyapatite nanocrystal formation from amorphous calcium phosphate in calcium-rich solutions". In: *Materials Chemistry and Physics* 91. DOI: 10.1016/j.matchemphys.2004.12.016.

Landing, E. (1994). "Precambrian-Cambrian boundary global stratotype ratified and a new perspective of Cambrian time". In: *Geology* 22. DOI: 10.1130/0091-7613(1994)022<0179:PCBGSR>2.3.CO;2.

LeGeros, R. Z. (1993). "Biodegradation and bioresorption of calcium phosphate ceramics". In: *Clinical Materials* 14. DOI: 10.1016/0267-6605(93)90049-D.

Lepland, A., V. A. Melezhik, D. Papineau, A. E. Romashkin, and L. Joosu (2013). "The Earliest Phosphorites: Radical Change in the Phosphorus Cycle During the Palaeoproterozoic". In: *Frontiers in Earth Sciences.* Vol. 8. Springer, Berlin, Heidelberg, pp. 1275–1296. DOI: 10.1007/978-3-642-29670-3_7.

Levashova, N. M., J. G. Meert, A. S. Gibsher, W. C. Grice, and M. L. Bazhenov (2011). "The origin of microcontinents in the Central Asian Orogenic Belt: Constraints from paleomagnetism and geochronology". In: *Precambrian Research* 185. DOI: 10.1016/j.precamres.2010.12.001.

Levashova, N. M., V. M. Kalugin, A. S. Gibsher, J. Yff, A. B. Ryabinin, J. G. Meert, and S. J. Malone (2010). "The origin of the Baydaric microcontinent, Mongolia: Constraints from paleomagnetism and geochronology". In: *Tectonophysics* 485. DOI: 10.1016/j.tecto.2010.01.012.

Levine, R. M. (2011). "The Mineral Industry of Kazakhstan". In: *2009 Minerals Yearbook.*

Li, D., H. F. Ling, G. A. Shields-Zhou, X. Chen, L. Cremonese, L. Och, M. Thirlwall, and C. J. Manning (2013). "Carbon and strontium isotope evolution of seawater across the Ediacaran–Cambrian transition: Evidence from the Xiaotan section, NE Yunnan, South China". In: *Precambrian Research* 225. DOI: 10.1016/j.precamres.2012.01.002.

Li, D. (2010). "Paleo-environment reconstruction from the south margin of Yangtze Platform in Late Neoproterozoic-early Cambrian interval: multi-proxy geochemical studies". PhD thesis. Nanjing University.

Linnemann, U., A. Gerdes, M. Hofmann, and L. Marko (2014). "The Cadomian Orogen: Neoproterozoic to Early Cambrian crustal growth and orogenic zoning along the periphery of the West African Craton—Constraints from U–Pb zircon ages and Hf isotopes (Schwarzburg Antiform, Germany)". In: *Precambrian Research* 244. DOI: 10.1016/j.precamres.2013.08.007.

Lyons, T. W., C. T. Reinhard, and N. J. Planavsky (2014). "The rise of oxygen in Earth's early ocean and atmosphere." In: *Nature* 506. DOI: 10.1038/nature13068. arXiv: 1402.3243.

Marshall, C. R. (2006). "Explaining the Cambrian "Explosion" of animals". In: *Annual Review of Earth and Planetary Sciences* 34. DOI: 10.1146/annurev.earth.33.031504.103001.

Maruyama, S., Y. Sawaki, T. Ebisuzaki, M. Ikoma, S. Omori, and T. Komabayashi (2014). "Initiation of leaking Earth: An ultimate trigger of the Cambrian explosion". In: *Gondwana Research* 25. DOI: 10.1016/j.gr.2013.03.012.

Miller, R. M. (1983). *Evolution of the Damara Orogen of South West Africa/Namibia.* Geological Society of South Africa, p. 515.

Mills, D. B. and D. E. Canfield (2014). "Oxygen and animal evolution: Did a rise of atmospheric oxygen "trigger" the origin of animals?" In: *BioEssays* 36. DOI: `10.1002/bies.201400101`.

Morris, S. C. (1989). "Burgess Shale Faunas and the Cambrian Explosion". In: *Science* 246. DOI: `10.1126/science.246.4928.339`.

– (2006). "Darwin's dilemma: the realities of the Cambrian 'explosion'". In: *Philosophical Transactions of the Royal Society B: Biological Sciences* 361. DOI: `10.1098/rstb.2006.1846`.

Papineau, D. (2010). "Global Biogeochemical Changes at Both Ends of the Proterozoic: Insights from Phosphorites". In: *Astrobiology* 10. DOI: `10.1089/ast.2009.0360`.

Pirajno, F. (2013). "Yangtze Craton, Cathaysia and the South China Block". In: *The Geology and Tectonic Settings of China's Mineral . . .* DOI: `10.1007/978-94-007-4444-8`.

Schulz, H. N. and H. D. Schulz (2005). "Large sulfur bacteria and the formation of phosphorite." In: *Science (New York, N.Y.)* 307. DOI: `10.1126/science.1103096`.

Sheldon, R. P. (1981). "Ancient Marine Phosphorites". In: *Annual Review of Earth and Planetary Sciences* 9. DOI: `10.1146/annurev.ea.09.050181.001343`.

Shen, Y., M. Schidlowski, and X. Chu (2000). "Biogeochemical approach to understanding phosphogenic events of the terminal Proterozoic to Cambrian". In: *Palaeogeography, Palaeoclimatology, Palaeoecology* 158. DOI: `10.1016/S0031-0182(00)00033-X`.

Shu, D. (2008). "Cambrian explosion: Birth of tree of animals". In: *Gondwana Research* 14. DOI: `10.1016/J.GR.2007.08.004`.

Smith, M. P. and D. T. Harper (2013). "Causes of the Cambrian Explosion". In: *Science* 341. DOI: `10.1126/science.1239450`.

Sperling, E. A., C. J. Wolock, A. S. Morgan, B. C. Gill, M. Kunzmann, G. P. Halverson, F. Macdonald, A. H. Knoll, and D. T. Johnston (2015). "Statistical analysis of iron geochemical data suggests limited late Proterozoic oxygenation". In: *Nature* 523. DOI: `10.1038/nature14589`.

Tostevin, R., R. A. Wood, G. A. Shields, S. W. Poulton, R. Guilbaud, F. Bowyer, A. M. Penny, T. He, A. Curtis, K. H. Hoffmann, and M. O. Clarkson (2016). "Low-oxygen waters limited habitable space for early animals". In: *Nature Communications* 7. DOI: `10.1038/ncomms12818`.

Trappe, J. (1998). *Phanerozoic phosphorite depositional systems : a dynamic model for a sedimentary resource system.* Springer, p. 316.

Wallace, M. W., A. S. Hood, A. Shuster, A. Greig, N. J. Planavsky, and C. P. Reed (2017). "Oxygenation history of the Neoproterozoic to early Phanerozoic and the rise of land plants". In: *Earth and Planetary Science Letters* 466. DOI: `10.1016/j.epsl.2017.02.046`.

Wang, J., D. Chen, D. Yan, H. Wei, and L. Xiang (2012). "Evolution from an anoxic to oxic deep ocean during the Ediacaran–Cambrian transition and implications for

bioradiation". In: *Chemical Geology* 306-307. DOI: `10.1016/j.chemgeo.2012.03.005`.

Weber, B., M. Steiner, S. Evseev, and G. Yergaliev (2013). "First report of a Meishucun-type early Cambrian (Stage 2) ichnofauna from the Malyi Karatau area (SE Kazakhstan): Palaeoichnological, palaeoecological and palaeogeographical implications". In: *Palaeogeography, Palaeoclimatology, Palaeoecology* 392. DOI: `10.1016/j.palaeo.2013.08.021`.

Weber, B., M. Steiner, and M. Y. Zhu (2007). "Precambrian-Cambrian trace fossils from the Yangtze Platform (South China) and the early evolution of bilaterian lifestyles". In: *Palaeogeography, Palaeoclimatology, Palaeoecology* 254. DOI: `10.1016/j.palaeo.2007.03.021`.

White, W. M. (2017). *Encyclopedia of Geochemistry A Comprehensive Reference Source on the Chemistry of the Earth.* Springer Verlag.

Wood, R. and A. Y. Zhuravlev (2012). "Escalation and ecological selectively of mineralogy in the Cambrian Radiation of skeletons". In: *Earth-Science Reviews* 115. DOI: `10.1016/j.earscirev.2012.10.002`.

Wood, R. A., J. P. Grotzinger, and J. A. Dickson (2002). "Proterozoic modular biomineralized metazoan from the Nama Group, Namibia". In: *Science* 296. DOI: `10.1126/science.1071599`.

Young, G. M. (2015). "Environmental upheavals of the Ediacaran period and the Cambrian "explosion" of animal life". In: *Geoscience Frontiers* 6. DOI: `10.1016/j.gsf.2014.09.001`.

Zhang, C. L., H. B. Zou, H. K. Li, and H. Y. Wang (2013). "Tectonic framework and evolution of the Tarim Block in NW China". In: *Gondwana Research* 23. DOI: `10.1016/j.gr.2012.05.009`.

Zhang, X., D. Shu, J. Han, Z. Zhang, J. Liu, and D. Fu (2014). "Triggers for the Cambrian explosion: Hypotheses and problems". In: *Gondwana Research* 25. DOI: `10.1016/j.gr.2013.06.001`.

Zhu, M., J. Zhang, and A. Yang (2007). "Integrated Ediacaran (Sinian) chronostratigraphy of South China". In: *Palaeogeography, Palaeoclimatology, Palaeoecology* 254. DOI: `10.1016/j.palaeo.2007.03.025`.

Chapter 2

Stable Magnesium and Radiogenic Strontium Isotopes in Carbonate Bearing Geologic Reference Materials by MC-ICP-MS

Jessica A. Stammeier[1]*, **Oliver Nebel**[2], **Dorothee Hippler**[1], **Martin Dietzel**[1]

[1]Institute of Applied Geosciences, Graz University of Technology, Rechbauerstraße 12, 8010 Graz, Austria

[2]School of Earth, Atmosphere and Environment, Monash University, Clayton VIC 3800, Australia

*corresponding author email: j.stammeier@web.de

Abstract

The distribution of stable Mg and radiogenic Sr isotopes in carbonate bearing material is commonly used as combined (paleo-) environmental and provenances proxies, however reference materials, in particular, where both values are given for distinctly composed materials, are rare. Therefore, $^{87}Sr/^{86}Sr$ was analysed for a range of carbonate bearing reference materials, together with $\delta^{26}Mg$ for a subset of samples with sufficient Mg content. Following chemical purification in a series of chromatographic extractions, isotope ratios were measured by multi-collector inductively coupled plasma-mass spectrometry (MC-ICP-MS) using a Plasma II (Nu Instruments). Magnesium isotope data yielded a whole procedural reproducibility of ± 0.09 ‰ for $\delta^{26}Mg$, relative to DSM3. Strontium isotopes were measured relative to NBS-987 with a whole procedural reproducibility within 100 ppm for $^{87}Sr/^{86}Sr$. Reference values for SRM 88A, SRM 1B, SARM 40, SARM 43, JDO-1, and JLS-1 span a range in $^{87}Sr/^{86}Sr$ ratios from 0.71022 to 0.73724 and from -2.2 to -0.4 ‰ for $\delta^{26}Mg$. This set of reference material can be used for materials with different carbonate mineral and matrix composition for justification and quality control measures of particularly combined stable Mg and radiogenic Sr isotope analyses in carbonate bearing or calcareous sediments and sedimentary rocks.

2.1 Introduction

Studies on stable and radiogenic isotope variations in natural materials have substantially increased over the last decades and, together with technological and scientific development, provide nowadays high precision analyses for a large number of isotopic systems (e.g., Woodhead, 2008; Hoefs, 2015; Teng, 2017). High-precision isotope analyses have become a cornerstone of scientific research with applications in the fields of hydro- and geosciences as well as e.g., forensics, archaeology or medical sciences (Benson et al., 2006; Buncel and Jones, 1991; Slovak and Paytan, 2012). Such analyses, however, require means of testing accuracy and precision as well as newly established methodologies in laboratories.

Among the non-traditional stable isotope systems that of Mg is of particular interest, because it is an important element in most natural surroundings. For low-temperature environmental processes, Mg isotope analyses are traditionally employed to trace source of fluid-borne Mg or to study process related elemental and isotope fractionation mechanisms and kinetics. The latter include (1) fluid-rock interaction, e.g., during weathering, soil formation, mineral surface reactions and dissolution – re-precipitation reactions (Beinlich et al., 2014; Mavromatis, Pearce, et al., 2012; Pearce et al., 2012; B. G. Pokrovsky, Mavromatis, and O. S. Pokrovsky, 2011; Schmitt et al., 2012; E. Tipper et al., 2006) as well as (2) biologically controlled processes, such as formation and decomposition of organic substances, biomineralization or ion transport through cell membrane channels (Bentov and Erez, 2006; Black, Yin, and Casey, 2006; Chang, Williams, et al., 2004; Saenger and Wang, 2014; Wombacher, Eisenhauer, Böhm, et al., 2011). In low-temperature settings, the $^{26}Mg/^{24}Mg$ variation is in the 5 ‰ range (Brenot et al., 2008; Galy et al., 2001; Pogge von Strandmann et al., 2008; E. T. Tipper, Galy, and Bickle, 2008), exceeding reported reproducibility tenfold (Wombacher, Eisenhauer, Böhm, et al., 2011; Wombacher, Eisenhauer, Heuser, et al., 2009).

Among radiogenic isotope systems, $^{87}Sr/^{86}Sr$ is well-established in low-temperature marine research, in particular considering carbonate, phosphate and sulfate minerals. For the latter mineral groups, the incorporated radiogenic Sr in the bivalent ion position of the mineral structure is used as an environmental proxy. Accordingly, radiogenic Sr isotopes have been used to trace Sr sources and mixing behaviour in aquatic bodies. Globally, as to the relatively long residence times in ocean water, Sr isotopes are further considered to be almost homogeneously distributed in global oceans over a million-year time-interval, which has led to the well-established Phanerozoic seawater $^{87}Sr/^{86}Sr$ evolution curve. Recorded variation in past ocean waters from ca. 0.7095 to 0.7065 (Halverson et al., 2007; Veizer et al., 1999) can thus potentially be used to trace silicate weathering versus mid-ocean ridge hydrothermal influx (Palmer and Edmond, 1989), and through Sr chronostratigraphy may provide rough age constraints when compared with seawater $^{87}Sr/^{86}Sr$ evolution (Shields and

Stille, 2001). Combining stable Mg isotope and radiogenic Sr data has great potential as a multi-proxy approach, in particular in low temperature environments due to their high abundance in aquatic systems, solely divalent ion character and complementary stable vs. radiogenic isotope tracer behaviour. Whilst Sr isotopes can routinely be analysed through thermal ionisation mass spectrometry (TIMS), Mg isotopes can be performed to much higher efficiency with a multi-collector inductively couple plasma mass spectrometer (MC-ICP-MS). However, despite pitfalls (Vroon et al., 2008), Sr has also been analysed with MC-ICP-MS providing a much higher sample throughput (Woodhead, 2002).

Chemical separation protocols for both Mg and Sr have been tested and optimised for different matrices, using cation exchange resin, e.g.,: BioRad 50W-X12, for Mg separation and Sr specific chromatographic resin, e.g., from Eichrom, for Sr separation (e.g., Galy et al., 2001; Chang, Makishima, et al., 2003). Some of these protocols facilitate the simultaneous separation of different elements (Chang, Makishima, et al., 2003; Wombacher, Eisenhauer, Heuser, et al., 2009). Among these, simultaneous separation of Mg and Sr (and also Ca) is especially interesting for carbonate bearing materials. Although, the use of combined radiogenic and stable isotope investigations, e.g., in the Proterozoic rock record or in Phanerozoic marine carbonates, requires reference material for quality control measures for testing accuracy and precision, surprisingly little combined δ^{26}Mg-^{87}Sr/^{86}Sr isotope data are available for carbonate bearing and calcareous reference materials.

In this study, we carried out combined stable Mg- radiogenic Sr isotope analyses on natural calcareous and carbonate bearing reference materials using MC-ICP-MS, where separation protocols were modified after Wombacher, Eisenhauer, Heuser, et al. (2009). Our protocols are developed in order to facilitate the near simultaneous or coupled routine analyses of Mg-Sr isotopes in Ca-rich samples. Here, we analysed the HNO$_3$ and HCl soluble leach-fraction of reference materials that include the carbonate minerals calcite, dolomite and magnesite.

2.2 Materials and Methods

2.2.1 Reference materials

For both isotope systems, respective Mg and Sr isotope values were determined on different types of calcareous and carbonate bearing reference materials and seawater. Reference materials SRM 88A, SRM 1B, SARM 40, SARM 43, JDO-1, and JLS-1 were chosen to represent carbonate minerals with varying Ca/Mg (0.02 – 127) and bulk mineral chemistry (see Table 2.1 for a description of the material). Additionally, for Mg isotopes, San Carlo olivine was analysed (a silicate with reported isotope values for Mg). A brief sample description is presented in Table 2.1.

TABLE 2.1: Sample description including selected element abundances of the analysed certified reference materials used in this study.

Reference material	Sample description	Distri-buter	MgO (wt.%)	CaO (wt.%)	Sr ($\mu g\ g^{-1}$)	Ca/Mg	Samplingsite/ References
SRM 88A[1]	Dolomitic limestone	NIST	21.3	30.2	85.0	1.42	Certificate of NIST SRM88A (1982)
SRM 1B[2]	Argillaceous limestone	NIST	0.36	50.9	1,180	127	Certificate of NIST SRM 1B (1966)
SARM 40	Carbonatite	SARM	1.97	49.8	1,600	25.3	(Govindaraju, 1994)
SARM 43	Magnesite	SARM	44.1	0.75	8.00	0.02	(Govindaraju, 1994)
JDO-1	Dolomite	GSJ	18.5	34.0	56,100	1.84	(Imai et al., 1996)
Jls-1	Limestone	GSJ	0.62	55.0	296	88.7	(Govindaraju, 1994)
San Carlos	(gem-quality) Olivine	Natural sample	n.a.	n.a.	n.a.	n.a.	San Carlos, USA
Seawater	Seawater was filtered and acidified prior to analyses						North Sea, Germany

[1] former NBS 88A, [2] former NBS 1B; NIST – National Institute of Standards and Technology (USA), SARM – South African, Bureau of Standards (South Africa), GSJ – Geological Survey of Japan (Japan)

2.2.2   Purification of chemical reagents

Sample digestion and ion (-exchange) chromatographic separation of Mg^{2+} and Sr^{2+} were carried out in laminar flow hoods, using Savillex® PFA beakers. Both HNO_3 and HCl acids (pro analyses quality) used for separation and dilution were purified by sub-boiling distillation in a PFA Savillex® DST-1000. The blanks of the purified acids were tested to be below the detection limits of < 50 ng l^{-1} for both Mg and Sr. Dilution of acids was performed with 18.2 MΩ.cm H_2O (at 25°C with <5 ng ml^{-1} TOC; MilliQ®). Beakers were cleaned in a two-step cleaning process involving both boiling in 5 mol l^{-1} HNO_3 and 6 mol l^{-1} HCl at 120 °C for a minimum of 24 hours each, followed by a final boiling in concentrated Aqua regia overnight. Other used lab materials (e.g., PE bottles, pipette tips) were cleaned in 0.8 mol l^{-1} HNO_3 at 60 °C for at least 48 hours.

Ion chromatographic resins were alternately cleaned in MilliQ water and double-distilled 1 mol l^{-1} HNO_3 or HCl, respectively, and then stored in 0.1 mol l^{-1} double-distilled HNO_3. For Mg separation BioRad AG50X12 resin was used. Columns consist of polypropylene with 5 cm length and 0.5 mm diameter loaded with 1 ml resin and an additional 5 ml reservoir. The columns - including the resin - were cleaned in several millilitres of both acids before use. In each cleaning step the resin was rinsed with several column volumes of MilliQ water. Strontium columns are prepared for each separation individually. Columns and frits were cleaned in 0.45 mol l^{-1} double-distilled HNO_3 and stored in MilliQ until used.

2.3   Instrumentation

2.3.1   Isotope ratios

Isotope analysis was carried out on a Plasma II MC-ICP-MS (Nu instruments, Wexham, UK) at Graz University of Technology, Austria. The instrumental parameters and settings during measurements of the Plasma II are summarized in Table 2.2 for the respective isotopes. Torch position, Ar-gas flow rates and lens set up were optimized to achieve maximum signal intensity and stability of the main beam, ^{88}Sr and ^{24}Mg, for Sr and Mg, respectively. Analyses were typically performed with a sensitivity of 25 V and 12.5 V for 500 μg ml^{-1} Sr and Mg, respectively, on the highest abundant isotopes (^{88}Sr, ^{24}Mg) using a 0.1 mL/min nebulizer flux in wet plasma mode. Data acquisition of Mg and Sr isotopes consisted of 1 block with 25 cycles for Sr and 50 cycles for Mg with an integration time of 5 seconds each.

TABLE 2.2: Operation conditions for Mg and Sr isotope determination with the Plasma II MC-ICP-MS (Nu Instruments).

Parameter	Running conditions	
Analyte	Mg	Sr
RF power	1300	1300
Plasma mode	Wet mode	Wet mode
Coolant gas	13.0 l min^{-1}	13.5 l min^{-1}
Auxiliary gas	0.85 − 0.9 min-1	0.85 - 0.95 l min^{-1}
Nebulizer pressure	32-33.5 psi	32.5 − 34.0 psi
Spray chamber temperature (Peltier)	5 °C	7 °C
Nebulizer flow rate	0.1 ml min^{-1}	0.1 ml min^{-1}

The background was determined by measuring 10 seconds at half masses before each block. To ensure repeatability and reproducibility, repeated analysis of reference materials Cambridge-1 (CAM-1), normalised to DMS3, during Mg isotope measurements and seawater during Sr isotope measurements, were performed. Concentration of reference materials and samples was adjusted to match within 10%, in order to avoid amplification of mass bias induced differences (An and Huang, 2014).

2.3.2   Major elements

Analyses of element concentrations for calibrating columns and testing yields were performed using inductively coupled plasma mass spectrometry (ICP-MS, Agilent 7500cx) with a measurement precision generally better than ± 5 % on element concentrations. Samples for the elution-calibration were taken up in 0.45 mol l^{-1} HNO$_3$. The instrument was tuned to achieve maximum sensitivity while maintaining low oxide production and doubly charged ion ratios with < 1.5% of the total concentrations. The concentration background was determined on a 0.45 mol l^{-1} HNO$_3$ blank solution and automatically subtracted from acquired data. Instrumental drift control

was performed by simultaneously running an internal reference solution with a 1 ng ml^{-1} of Sc, Ge, and Bi.

2.4   Sample Digestion

For the San Carlos olivine, three duplicates of each 5 mg of finely grained powder were digested in 3 ml of a 1:3 HNO$_3$–HF concentrated acid mixture, sealed tight and left to boil on a hot plate at 110 °C for 24 hours. The HNO$_3$–HF was evaporated at 70 °C and the samples were treated with a small amount of concentrated HNO$_3$and concentrated H$_2$O$_2$ as oxidizing agents to eliminate Ca-fluoride complexes. These solutions were then dried and re-dissolved in concentrated HCl to eliminate remaining nitrates. Prior to separation, seawater was filtered through a 0.45μm membrane acetate filter (Sartorius). For chemical separation, 10 ml of seawater was dried down and treated with small amounts of H$_2$O$_2$ and concentrated HNO$_3$to break up organic complexes.

For the reference materials, SRM 88A, SRM 1B, SARM 40, SARM 43, JDO-1, and JLS-1, ca. 100 mg powdered material was digested. From these stock solutions, aliquots were taken (different in volume), each for Mg and Sr separation, aiming for a concentration of ca. 100 μg ml^{-1} of the respective elements (Mg and Sr). Each sample was treated with 3 mol l^{-1} HNO$_3$until no carbonate dissolution reaction was visible. Aliquots were evaporated to dryness and re-digested in the respective acids (2 mol l^{-1} HNO$_3$for Mg and 3 mol l^{-1} HNO$_3$for Sr) for chemical separation protocol (Tables 2.3, 2.5). One procedural blank sample was included per ten samples per separation and treated in the same manner as a sample.

TABLE 2.3: Two-step separation protocol for Mg using Biorad 50W-X12 resin. Both separation steps, Ca separation and Mg purification, can be performed on the same column.

Step	Amount (ml)	Molarity (mol l^{-1})	Reagent	Elution
Ca separation:				
condition	2	2	HNO$_3$	
load	1	2	HNO$_3$	
wash	5	2	HNO$_3$	
wash	10	2	HNO$_3$	Mg
wash	10	7	HNO$_3$	Divalent cations
cleaning	3	-	H$_2$O	
Mg purification:				
condition	2	0.4	HCl	
load	0.5	0.4	HCl	
rinse	30	0.4	HCl	
collect	4	5	HCl	Mg

2.5 Chromatographic Purification

2.5.1 Magnesium separation

For magnesium purification, a two-step ion exchange chemistry was employed using HNO_3 and HCl as eluent, based on the protocol developed by Wombacher, Eisenhauer, Heuser, et al. (2009). This two-step separation is optimized for samples with a high Ca/Mg ratio. The first step ensured the effective separation of Ca from the matrix and can also be employed for a simultaneous isolation of Zn, Fe and Ca ions for subsequent isotope analyses (Wombacher, Eisenhauer, Heuser, et al., 2009; Table 2.3, Figure 2.1). In the second step, Mg was separated from other matrix elements, such as K and Ti (Table 2.4) that have not been efficiently been removed in the first step (Figure 2.2). Both separation steps were performed on the same columns using the BioRad AG50-X12 resin. Between each separation step, the columns were cleaned with one column volume of 7 mol l^{-1} HNO_3 and MilliQ water.
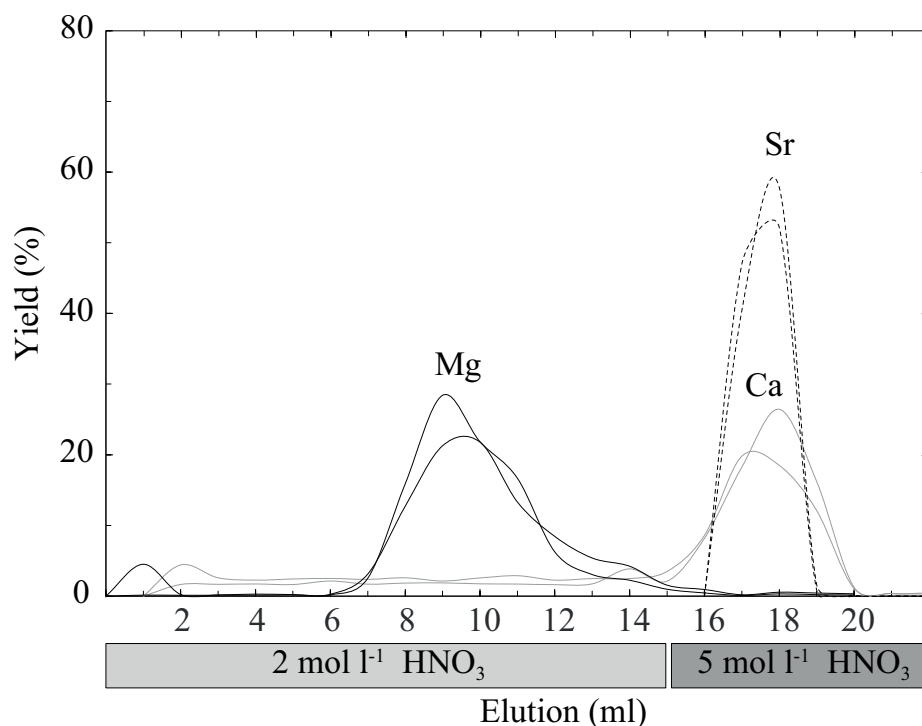
FIGURE 2.1: Magnesium yield during the Ca separation step. Separation was performed with two different replicates yielding identical results. More than 99% of Mg is eluted after 15 ml HNO_3, as is required to avoid Mg fractionation during chemical separation (Chang, Makishima, et al., 2003). Calcium and Sr can effectively be eluted with a higher concentrated acid.

Separation was tested with an artificial solution containing 10 μg ml^{-1} of Mg, Ca, Sr, Na, Al (admixed in equal concentrations from single element MERCK standard solutions) and MERCK multi-element standard solution X. These solutions were chosen to resemble (1) a typical elemental composition obtained e.g., from an experimental

TABLE 2.4: Cup configuration for Mg measurements with a mass discrimination of 0.125 amu. No isobaric interferences from other isotopes are reported for these masses. Spectral interferences, however, can occur from formation of doubly charged ions (e.g., Ca^{++}, Ti^{++}) and various oxides and nitrites.

Cup	L4	H2	H7
Mass	24	25	26
Isotope	^{24}Mg	^{25}Mg	^{26}Mg
Spectral interferences	$^{48}Ti^{++}$, $^{48}Ca^{++}$ $^{12}C^{12}C$	$^{50}Ti^{++}$, $^{50}Cr^{++}$, $^{50}V^{++}$, $^{12}C^{13}C$, $^{9}Be^{16}O$, $^{7}Li^{18}O$	$^{52}Cr^{++}$, $^{12}C^{14}N$, $^{12}C^{13}CH$, $^{10}B^{16}O$, $^{9}Be^{17}O$, $^{40}Ar^{12}C^{++}$

carbonate precipitation set-up, including elements that may cause interferences during Mg isotope measurements, and (2) a solution with a high Ca/Mg ratio including a wide range of matrix elements that resembles those of typical calcareous samples. For the first Ca separation step, the columns were conditioned with 2 ml of 2 mol l^{-1} HNO_3. The sample was subsequently loaded with 1 ml of 2 mol l^{-1} HNO_3. After elution with 5 ml of 2 mol l^{-1} HNO_3, Mg was recovered in 10 ml of 2 mol l^{-1} HNO_3. The remaining divalent cations on the columns were washed off using 7 mol l^{-1} HNO_3. This fraction contained the Sr fraction and was used for further separation of Sr. The collected Mg was evaporated to dryness and re-dissolved in 1 ml of 0.4 mol l^{-1} HCl. In the second step the columns were conditioned with 0.4 mol l^{-1} HCl and loaded with the samples. After washing with 30 ml of 0.4 mol l^{-1} HCl the Mg fraction was recovered in 4 ml of 5 mol l^{-1} HCl.

2.6   Strontium Separation

For the Sr separation a single, well-established extraction ion chromatographic chemistry was employed (Table 2.5, after Pin and Bassin, 1992). A second separation step, sometimes required for high-Rb samples (Nebel, Scherer, and Mezger, 2011) is not required, as calcareous or carbonate bearing material can be expected to have low to very low Rb/Sr. The columns consisted of polypropylene pipette tips (Eppendorf) and 20-60 μm frit material (Porex) and were filled with 100 μl Sr-Specific resin (Eichrom). For Sr separation 3 mol l^{-1} HNO_3 and MilliQ water were required. Dried down samples were re-dissolved in 3 mol l^{-1} HNO_3. The columns were conditioned in 1 ml 3 mol l^{-1} HNO_3 and then loaded with the sample. After washing with 5 ml 3 mol l^{-1} HNO_3, Sr was recovered in 3 ml MilliQ.

To test the yield during the Sr separation, an element reference solution with 10 μg l^{-1} of Mg, Ca, Rb, Sr, Fe and Zn (admixed from Merck single element standard solutions) was prepared (Figure 2.3). The elution curve shows Rb, which forms an isobaric interference with ^{87}Rb on ^{87}Sr during measurements, is effectively separated after 3 ml of washing with 3 mol l^{-1} HNO_3 and Sr should be collected after 5 ml of washing (including the ml of sample loading). Further, Mg is effectively separated from the
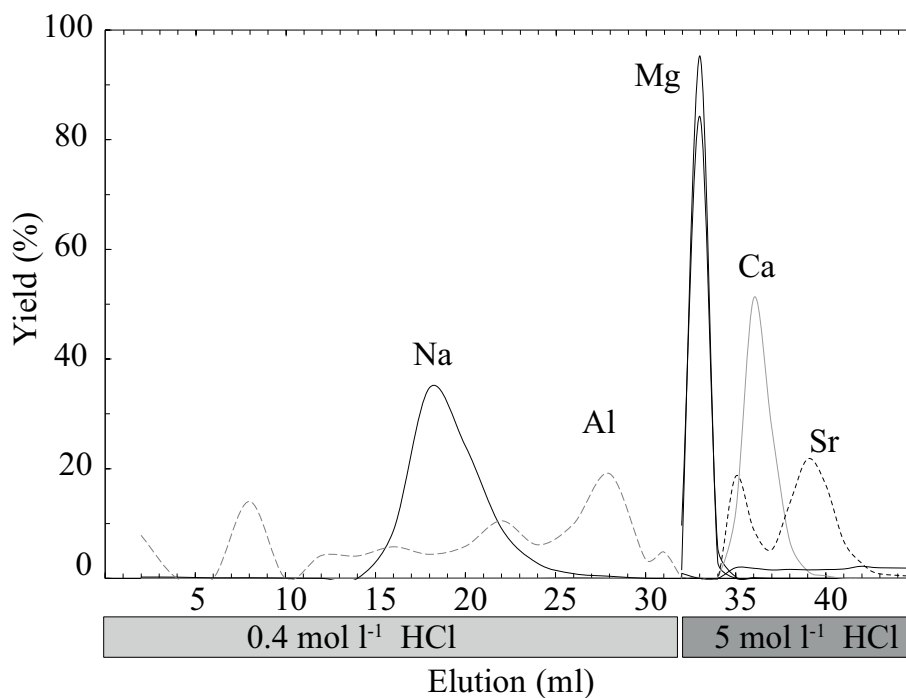
FIGURE 2.2: Second step of the Mg purification. The heterogeneity of the matrix does not affect the efficiency of Mg elution. The elution of Mg in both an artificial solution containing Mg, Ca, Sr, Al and a heterogeneous solution (MERCK X), resembling natural materials, are identical (see text for details).

TABLE 2.5: Strontium separation, modified after (Pin et al., 2014).

Step	Amount (ml)	Molarity (mol l^{-1})	Reagent	Elution
condition	1	3	HNO$_3$	
load	1	3	HNO$_3$	Mg, Ca, Zn, Fe, Rb
wash	4	3	HNO$_3$	
collect	3	-	H$_2$O	Sr, Ca

Sr fraction, potentially facilitating a coupled separation with the Sr separation step in the reverse order. However, due to the high Ca content of most samples, this is not recommended as columns may be overloaded. The bulk Sr was eluted from the columns with MilliQ water. However, minor amounts of Sr were observed to be eluted from the columns after washing with more than 5 ml of 3 mol l^{-1} HNO$_3$, which may be of importance should stable Sr isotope analyses be pursued for which a > 95% yield is necessary.
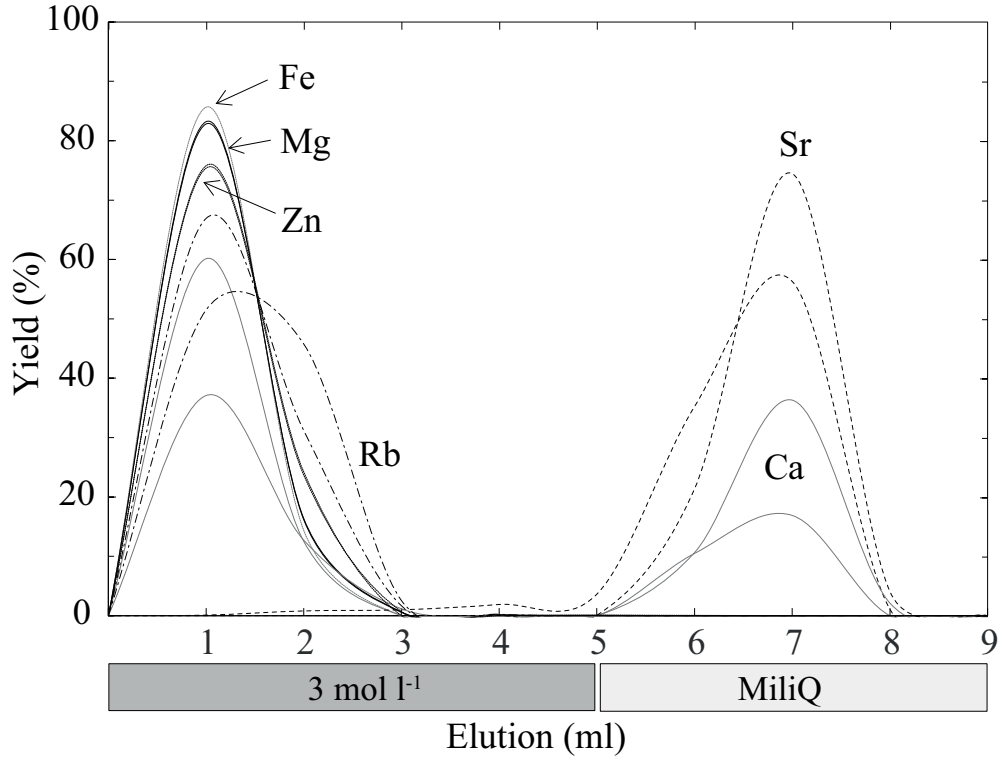
FIGURE 2.3: Elution curve of an artificial solution containing the elements Mg, Ca, Fe, Zn, Rb and Sr (from MERCK single element standard solution). The abscissa refers to the elution in ml with the respective solvents. Note that up to $20-40$ % of Ca is washed off the columns together with Sr.

2.7 Data Acquisition and Reduction

2.7.1 Magnesium isotopes

Instrumental mass bias needs to be adequately corrected for during high-precision stable Mg isotope analyses. For this, the standard sample bracketing (SSB) method normalizing to the DSM3 reference material was used (Hilton et al., 2015). Magnesium isotopes were collected in Faraday cups with a set-up reported in Table 2.1. For each individual measurement, samples and DSM3 standard solution were diluted with 0.45 mol l^{-1} HNO$_3$ to aim at concentration of ca. 0.05 μg ml^{-1}, yielding ca. 25 V per μg ml^{-1} for total Mg in wet plasma mode. Before each measurement a two-step washing protocol using MilliQ and double-distilled 0.45 mol l^{-1} HNO$_3$ was employed. Mg isotopic ratios are reported in the δ–notation calculated relative to DSM3 reference material:

$$\delta^X\text{Mg} = \left(\frac{\left(\frac{^X Mg}{^{24}Mg}\right)_{\text{sample}}}{\left(\frac{^X Mg}{^{24}Mg}\right)_{\text{DSM3}}} - 1 \right) \cdot 1000 \tag{2.1}$$

with X referring to either ^{25}Mg or ^{26}Mg, respectively.

2.7.2 Strontium isotopes

During Sr isotope measurements each isotope was collected in an assigned cup as reported in Table 2.6. All measured Sr isotope ratios were in-run corrected for baseline, interferences (^{87}Rb and ^{86}Kr) and instrumental mass bias. The latter can be corrected by using the observed mass bias factor β of an invariant isotope ratio, in this case a ^{86}Sr/^{88}Srr = 0.1194 (Steiger and Jäger, 1977), and the exponential law. Interference correction is applied by monitoring an isotope of the respective element without isobaric interference, e.g., ^{85}Rb and ^{84}Kr, ^{86}Kr and subtracting the mass bias corrected isotope ratios. Krypton interferences are corrected for using a value of ^{86}Kr/^{84}Kr = 0.3035; Rb interferences are corrected with a value of ^{87}Rb/^{85}Rb=0.3857. Note that through chemical purification of Sr, Rb contents should be negligible and Rb interference correction does not affect the Sr isotope analyses.

TABLE 2.6: Cup configuration for static-cup Sr measurements. Mass discrimination is 0.5 amu.

Cup	L5	L3	L1	H1	H3	H5
Mass	83	84	85	86	87	88
Isotope		Sr		Sr	Sr	Sr
Isobaric	Kr	Kr		Kr		
interferences			Rb		Rb	
	^{38}Ar^{45}Sc	^{36}Ar^{48}Ti	^{36}Ar^{49}Ti	^{40}Ar^{46}Ti	^{40}Ar^{47}Ti	^{36}Ar^{52}Cr
	^{36}Ar^{47}Ti	^{37}Ar^{47}Ti	^{40}Ar^{45}Sc	^{36}Ar^{50}Ti	^{38}Ar^{49}Ti	^{40}Ar^{48}Ti
Spectral	^{40}Ar^{43}Ca	^{40}Ar^{44}Ca	^{69}Ga^{16}O	^{38}Ar^{48}Ti	^{71}Ga^{16}O	^{40}Ar^{48}Ca
interferences	^{67}Zn^{16}O	^{68}Zn^{16}O	^{67}Zn^{18}O	^{68}Zn^{18}O	^{70}Ge^{17}O	^{71}Ge^{17}O
	^{66}Zn^{17}O	^{66}Zn^{18}O	^{68}Zn^{17}O	^{70}Zn^{16}O	^{69}Ga^{18}O	^{70}Ge^{18}O
	^{65}Cu^{18}O			^{69}Ga^{16}O		^{72}Ga^{16}O

The mass bias factor β is determined in an iterative calculation: interference of ^{86}Kr on ^{86}Sr was first subtracted, using a synthetically biased ^{86}Kr/^{84}Kr. For this, a β_0 value was calculated from a non-interference corrected, measured ^{86}Sr/^{88}Sr value and applied to ^{86}Kr/^{84}Kr to simulate mass bias for this ratio. The then corrected ^{86}Sr/^{88}Sr from this first step was used to calculate a new β_1 value and the process was repeated. We found that after ten iterations of consecutive mass bias- and interference-correction β converged to a constant value. The final β_{10} value was then applied to the ^{87}Rb interference corrected ^{87}Sr/^{86}Sr. Samples were measured in blocks of 6, which were bracketed by two consecutive measurements of NBS-987.

2.8 Data Evaluation

2.8.1 Magnesium isotopes

Mass drift of the two bracketing standards may exceed the anticipated repeatability of ± 0.25 ‰ of δ^{26}Mg (Wombacher, Eisenhauer, Heuser, et al., 2009). If so, the sample

measured in-between these standards will be artificially shifted and yield inaccurate results. We thus rejected these individual analyses. Each sample was measured three to six times and the reported isotope ratio constitutes the average of these analyses with the standard deviation being the deviation from this average. Over the course of one month, repeated measurements of a secondary reference solution (CAM-1) yielded an intermediate precision, expressed as 2s, of $\pm$ 0.10 ‰ of $\delta^{26}Mg$ (n=23), exceeding a reproducibility of $\pm$ 0.03 ‰ of $\delta^{26}Mg$, compared to values reported by e.g., Mavromatis, Meister, and Oelkers (2014). Chemical separation and Mg isotope measurements of the reference material JDO-1 yielded a whole procedural reproducibility of $\pm$ 0.09 ‰ of $\delta^{26}Mg$ (2s) compared to previously reported values Mavromatis, Meister, and Oelkers (2014) and Mavromatis, Gautier, et al. (2013).
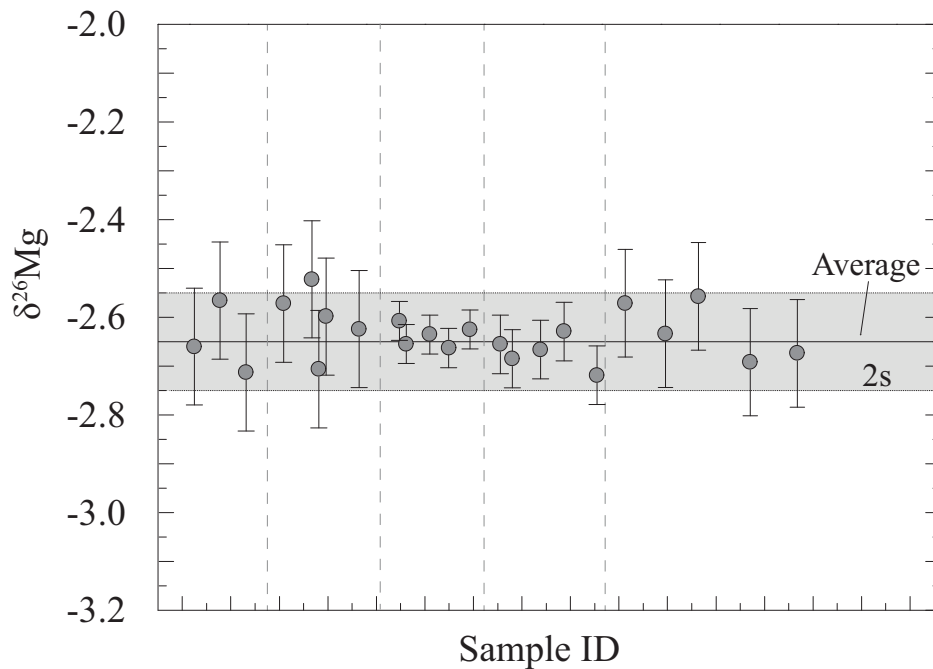
FIGURE 2.4: Results of CAM-1 measurements on different days, i.e., different measurement sessions, each session separated by dashed lines. In between each CAM-1 data point were usually 5-6 measurements of samples bracketed by DSM3. In this manner external reproducibility was ensured, which was found to be $\pm$ 0.03 ‰ for $\delta^{26}Mg$ (2s). Grey area indicates the 2s variation of the whole data set and represents the intermediate precision of $\pm$ 0.10 ‰ for $\delta^{26}Mg$. Range bars represent the repeatability measurement precision within each session and ranges from $\pm$ 0.04 ‰ to $\pm$ 0.12 ‰ for $\delta^{26}Mg$ (2s).

2.8.2   Strontium

Isotope variations in radiogenic Sr isotopes were monitored and corrected for by repeated measurements of NBS-987 in each session. For each session we used a freshly prepared batch of NBS-987 reference solution diluted to 0.5 μg ml^{-1} of Sr. The correction for systematic offsets in analytical sessions was performed by normalizing the acquired data of the average of the bracketing standards measured before and after

each set of samples to a reference value of $^{87}Sr/^{86}Sr = 0.710250$ (Hans, 2013). During three month of Sr isotope measurements, intermediate precision, expressed as 2s, of seawater as a secondary reference yielded an uncertainty of $^{87}Sr/^{86}Sr = \pm 0.000011$. Reproducibility of seawater $^{87}Sr/^{86}Sr$ in each session was typically within 100 ppm (2s) and thus well within reported performances of the Plasma II MC-ICP-MS (Hans, 2013).

2.9 Results and Discussion

2.9.1 Magnesium isotopes

Repeated measurements of reference solution CAM-1 yielded $\delta^{26}Mg$ and $\delta^{25}Mg$, respectively, of -2.64 $\pm$ 0.10 ‰ and -1.36 $\pm$ 0.04 ‰ (2s, n=23; Table 2.7, Figure 2.4). This intermediate precision is identical to a reported measurement precision in the literature for these solutions of $\pm$ 0.1 ‰ for $\delta^{26}Mg$ (2s; Chang, Makishima, et al., 2003; Galy et al., 2001; Pearson et al., 2006; Wombacher, Eisenhauer, Böhm, et al., 2011.
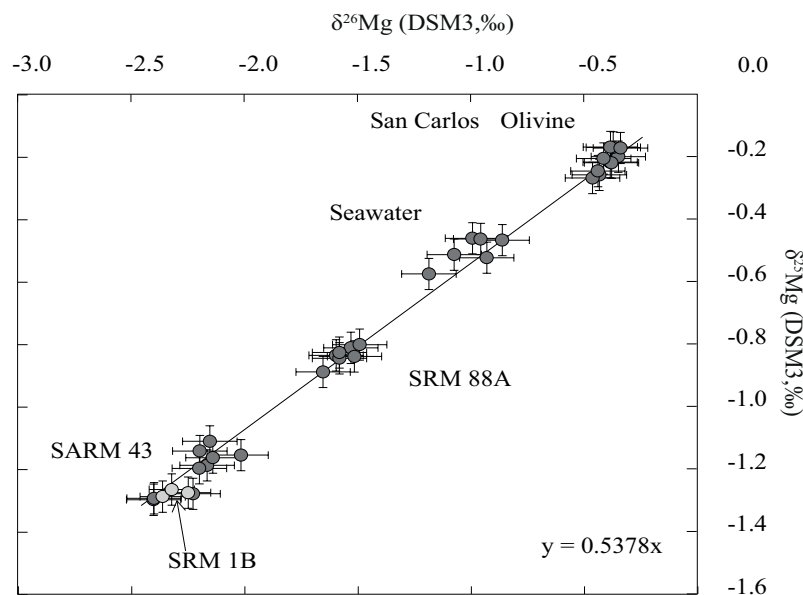
FIGURE 2.5: Three isotope plot displaying the $\delta^{25}Mg$ vs. $\delta^{26}Mg$ with a measured mass-dependent fractionation of 0.5378. Range bars refer to an intermediate precision, expressed as 2s, of $\pm$ 0.10 ‰ for $\delta^{26}Mg$ and $\pm$ 0.04 ‰ for $\delta^{25}Mg$ (DSM3).

San Carlos olivine yielded average values of -0.39 $\pm$ 0.08 ‰ for $\delta^{26}Mg$ (2s, n=10), which is broadly in the range of published values (compare Table 2.7). Heterogeneities in the San Carlos Olivine have previously been reported, including a batch trial that resulted in varying results (Chakrabarti and Jacobsen, 2010). Different causes have been collectively or partly made responsible: (1) sampling biases, (2) Mg isotopic heterogeneity, (3) analytical artefacts (An and Huang, 2014). Seawater $\delta^{26}Mg$ was

found to be -1.00 ± 0.21 ‰ (n=6), slightly higher than previously reported values of ca. -0.8 ‰, yet within measurement precision (e.g., E. T. Tipper, Galy, and Bickle, 2008; Hu et al., 2016.

TABLE 2.7: Magnesium isotope results from this study and published values presented relative to DSM3. SCO = San Carlos Olivine. n refers to the number of repeated measurements used to calculate the average δ-value and respective standard deviation.

Name	$\delta^{25}Mg$ (DSM3,‰)	± (2s)	$\delta^{26}Mg$ (DSM3,‰)	± (2s).	n	Reference
JDO-1	-1.3	0.01	-2.47	0.05	3	This study
JDO-1	-1.25 – -1.21	0.06 – 0.05	-2.4 – -2.36	0.06 – 0.08	3	[1] [2]
SCO	-0.24	0.06	-0.41	0.09	4	This study
SCO	-0.17	0.00	-0.36	0.04	3	This study
SCO	-0.22	0.03	-0.41	0.05	3	This study
Average:	-0.21	0.07	-0.39	0.08	10	This study
SCO	-0.38 – -0.30	0.04	-0.73 – -0.62	0.06 – 0.1	4	[3]
SCO	-0.28	0.1	-0.58	0.15	6	[4]
SCO	-0.38	0.2	-0.64	0.31	10	[4]
SCO	-0.03	0.04	-0.06	0.07	5	[5]
SRM-1B	-1.28	0.02	-2.31	0.09	3	This study
SRM-88A	-0.85	0.06	-1.59	0.09	4	This study
SRM-88A	-0.86	0.12	-1.53	0.07	4	This study
Average:	-0.85	0.09	-1.56	0.10	8	This study
SARM-43	-1.25	0.10	-2.26	0.20	3	This study
SARM-43	-1.14	0.04	-2.12	0.15	4	This study
SARM-43	-1.22	0.11	-2.24	0.22	3	This study
Average:	-1.20	0.13	-2.21	0.23	10	This study
CAM-1	-1.36	0.04	-2.64	0.10	23	This study
CAM-1	-1.32	0.07	-2.61	0.06	12	[2]

[1] Mavromatis et al. 2013, [2] Mavromatis et al. 2014, [3] Teng et al., 2007, [4] Pearson et al., 2006, [5] Wiechert and Halliday, 2007

Magnesium isotope analysis of the three analysed reference materials SARM-43 (magnesite), SRM-88A (dolomitic limestone) and SRM-1B (argillaceous limestone), all without published Mg isotope values, yielded results in the same range as inorganic carbonate bearing material (Fantle and Higgins, 2014). The lowest $\delta^{26}Mg$ value was found in SRM-1B with a $\delta^{26}Mg$ of -2.31 ± 0.09 ‰, closely followed by SARM-43 with -2.21 ± 0.23 ‰ (2s, n=10). SRM-88A, a dolomitic limestone yielded $\delta^{26}Mg$ values of -1.56 ± 0.10 ‰ (n=8). All samples are reported relative to DSM3 and plot on a mass-dependent fractionation line with a slope of $\beta = 0.538$, roughly similar to a theoretically calculated β for equilibrium processes of 0.521 (Figure 2.5; Young and Galy, 2004.

2.9.2 Strontium isotopes

The lowest $^{87}Sr/^{86}Sr$ of this study was analysed for the carbonatite material SARM 40 with a value of 0.702930 ± 0.000031 (n=8, Table 2.8, Figure 2.6). Reference materials SRM 1B argillaceous limestone, JDO-1 pure dolomite, and JLS-1 limestone, all have similar $^{87}Sr/^{86}Sr$ values of 0.707403 ± 0.000001 (n=11), 0.707565 ± 0.000040 (n=19) and 0.707843 ± 0.000018 (n=9), respectively.
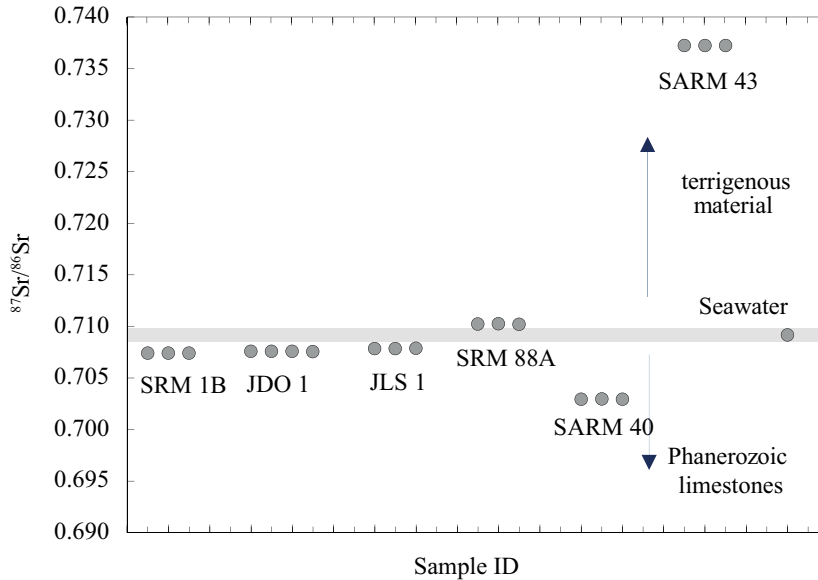
FIGURE 2.6: $^{87}Sr/^{86}Sr$ values of certified reference materials (this study). The analytical uncertainty (2s) is smaller than symbol size. Bright grey line indicates present day seawater $^{87}Sr/^{86}Sr$ value (Elderfield, 1986).

Both $^{87}Sr/^{86}Sr$ values of JLS-1 and JDO-1 were identical within analytical precision to published values by Miura, Asahara, and Kawabe (2004) and Ohno and Hirata (2007). The dolomitic limestone SRM 88A has high $^{87}Sr/^{86}Sr$ of 0.710217 ± 0.000054 (n=7) close to the reference material used for internal normalization NBS-987. The highest value was measured in SARM 43, a magnesite, with an average value of 0.737239 ± 0.000006. The average $^{87}Sr/^{86}Sr$ value of seawater was used as an external control reference and was found to be 0.709197 ± 0.000011 (n=19), identical to reported seawater values of 0.70924 ± 0.00003 (e.g., Elderfield, 1986).

TABLE 2.8: Compiled results from Sr isotope measurements; n refers to the number of analysis. All data from this study are reported relative to NBS-987 ($^{87}Sr/^{86}Sr= 0.710250 \pm 0.000008$ reported by Hans (2013))

Name	$^{87}Sr/^{86}Sr$	$\pm(2s)$	(n)	Reference
SARM-40	0.702935	0.000035	3	This study
SARM-40	0.702946	0.000038	3	This study
SARM-40	0.702909	0.000133	2	This study
Average:	0.702930	0.000031	8	This study
SRM 1B	0.707403	0.000022	2	This study
SRM 1B	0.707402	0.000011	3	This study
SRM 1B	0.707403	0.000023	6	This study
Average:	0.707403	0.000001	11	This study
JDO-1	0.707582	0.000018	3	This study
JDO-1	0.707569	0.000023	4	This study
JDO-1	0.707577	0.000046	6	This study
JDO-1	0.707531	0.000045	6	This study
Average:	0.707565	0.000040	19	This study
JDO-1	0.70752	0.00002		(Ohno and Hirata, 2007)
JDO-1	0.707513	0.000014		(Miura et al., 2004)
JLs-1	0.707837	0.000014	3	This study
JLs-1	0.707836	0.000039	2	This study
JLs-1	0.707856	0.000041	4	This study
Average:	0.707843	0.000018	9	This study
JLs-1	0.70785	0.00006		(Ohno and Hirata, 2007)
SRM 88A	0.710234	0.000063	2	This study
SRM 88A	0.710239	0.000049	2	This study
SRM 88A	0.710180	0.000030	3	This study
Average:	0.710217	0.000054	7	This study
SARM 43	0.737236	0.000013	1	This study
SARM 43	0.737243	0.000050	5	This study
SARM 43	0.737237	0.000025	3	This study
Average:	0.737239	0.000006	9	This study
Seawater	0.709197	0.000011	19	This study

2.10   Summary

In the present study a reliable and fast method was developed to acquire stable Mg and radiogenic Sr isotopes of carbonate bearing materials with a relatively high Ca/Mg. A set of combined stable Mg and radiogenic Sr isotope values for three certified reference materials, SARM 43, SRM 1B, SRM 88A, and radiogenic Sr isotope values for SARM 40 are suggested, which are readily available and can be used as secondary reference material as quality control measures. To date no such values are available and further systematic work is suggested to build up a reliable database of reference material values. Effective chemical separation of both elements from the same dissolution was achieved using ion specific resins BioRad 50W-X12 for Mg separation and Sr specific chromatographic resin from Eichrom for Sr separation. For method verification, JDO-1, JLS-1, Cambridge-1, seawater and a San Carlos olivine were analysed using the developed protocol yielding isotope values similar to reported reference values within the intermediate measurement precision of $\pm\,0.10\,‰$ for δ^{26}Mg and $\pm\,0.000011$ for ^{87}Sr/^{86}Sr, derived from repeated measurements of CAM-1 and seawater, respectively.

Acknowledgements

References

An, Y. and F. Huang (2014). "A review of Mg isotope analytical methods by MC-ICP-MS". In: *Journal of Earth Science* 25. DOI: 10.1007/s12583-014-0477-8.

Beinlich, A., V. Mavromatis, H. Austrheim, and E. H. Oelkers (2014). "Inter-mineral Mg isotope fractionation during hydrothermal ultramafic rock alteration – Implications for the global Mg-cycle". In: *Earth and Planetary Science Letters* 392. DOI: 10.1016/j.epsl.2014.02.028.

Benson, S., C. Lennard, P. Maynard, and C. Roux (2006). *Forensic applications of isotope ratio mass spectrometry - A review.* DOI: 10.1016/j.forsciint.2005.03.012.

Bentov, S. and J. Erez (2006). "Impact of biomineralization processes on the Mg content of foraminiferal shells: A biological perspective". In: *Geochemistry, Geophysics, Geosystems* 7. DOI: 10.1029/2005GC001015.

Black, J. R., Q. Yin, and W. H. Casey (2006). "An experimental study of magnesium-isotope fractionation in chlorophyll-a photosynthesis". In: *Geochimica et Cosmochimica Acta* 70. DOI: 10.1016/j.gca.2006.06.010.

Brenot, A., C. Cloquet, N. Vigier, J. Carignan, and C. France-Lanord (2008). "Magnesium isotope systematics of the lithologically varied Moselle river basin, France". In: *Geochimica et Cosmochimica Acta* 72. DOI: 10.1016/j.gca.2008.07.027.

Buncel, E. and J. R. Jones (1991). *Isotopes in the Physical and Biomedical Sciences: Isotopic applications in NMR studies.* Elsevier Science Pub. Co. Inc.,New York, NY.

Chakrabarti, R. and S. B. Jacobsen (2010). "Silicon isotopes in the inner Solar System: Implications for core formation, solar nebular processes and partial melting". In: *Geochimica et Cosmochimica Acta* 74. DOI: 10.1016/j.gca.2010.08.034.

Chang, V. T. C., A. Makishima, N. S. Belshaw, and R. K. O'Nions (2003). "Purification of Mg from low-Mg biogenic carbonates for isotope ratio determination using multiple collector ICP-MS". In: *Journal of Analytical Atomic Spectrometry* 18. DOI: 10.1039/b210977h.

Chang, V. T. C., R. J. P. Williams, A. Makishima, N. S. Belshawl, and R. K. O'Nions (2004). "Mg and Ca isotope fractionation during CaCO 3 biomineralisation". In: *Biochemical and Biophysical Research Communications* 323. DOI: 10.1016/j.bbrc.2004.08.053.

Elderfield, H. (1986). "Strontium isotope stratigraphy". In: *Palaeogeography, Palaeoclimatology, Palaeoecology* 57. DOI: 10.1016/0031-0182(86)90007-6.

Fantle, M. S. and J. Higgins (2014). "The effects of diagenesis and dolomitization on Ca and Mg isotopes in marine platform carbonates: Implications for the geochemical cycles of Ca and Mg". In: *Geochimica et Cosmochimica Acta* 142. DOI: 10.1016/j.gca.2014.07.025.

Galy, A., N. S. Belshaw, L. Halicz, and R. O'Nions (2001). "High-precision measurement of magnesium isotopes by multiple-collector inductively coupled plasma mass

spectrometry". In: *International Journal of Mass Spectrometry* 208. DOI: `10.1016/S1387-3806(01)00380-3`.

Halverson, G. P., F. Ö. Dudás, A. C. Maloof, and S. A. Bowring (2007). "Evolution of the 87Sr/86Sr composition of Neoproterozoic seawater". In: *Palaeogeography, Palaeoclimatology, Palaeoecology* 256. DOI: `10.1016/j.palaeo.2007.02.028`.

Hans, U. (2013). "High-precision strontium isotope measurements on meteorites: implications for the origin and timing of volatile depletion in the inner solar system". Dissertation. ETH Zürich.

Hilton, R. G., V. Galy, J. Gaillardet, M. Dellinger, C. Bryant, M. O'Regan, D. R. Gröcke, H. Coxall, J. Bouchez, and D. Calmels (2015). "Erosion of organic carbon in the Arctic as a geological carbon dioxide sink." In: *Nature* 524. DOI: `10.1038/nature14653`. arXiv: `ÐóÐżÑŔ1-2`.

Hoefs, J. (2015). *Stable Isotope Geochemistry*. Ed. by J. Hoefs. Cham: Springer International Publishing. DOI: `10.1007/978-3-319-19716-6`. arXiv: `arXiv:1011.1669v3`.

Hu, Y., M. D. Harrington, Y. Sun, Z. Yang, J. Konter, and F. Z. Teng (2016). "Magnesium isotopic homogeneity of San Carlos olivine: a potential standard for Mg isotopic analysis by multi-collector inductively coupled plasma mass spectrometry". In: *Rapid Communications in Mass Spectrometry*. DOI: `10.1002/rcm.7700`.

Mavromatis, V., C. R. Pearce, L. S. Shirokova, I. a. Bundeleva, O. S. Pokrovsky, P. Benezeth, and E. H. Oelkers (2012). "Magnesium isotope fractionation during hydrous magnesium carbonate precipitation with and without cyanobacteria". In: *Geochimica et Cosmochimica Acta* 76. DOI: `10.1016/j.gca.2011.10.019`.

Mavromatis, V., Q. Gautier, O. Bosc, and J. Schott (2013). "Kinetics of Mg partition and Mg stable isotope fractionation during its incorporation in calcite". In: *Geochimica et Cosmochimica Acta* 114. DOI: `10.1016/j.gca.2013.03.024`.

Mavromatis, V., P. Meister, and E. H. Oelkers (2014). "Using stable Mg isotopes to distinguish dolomite formation mechanisms: A case study from the Peru Margin". In: *Chemical Geology* 385. DOI: `10.1016/j.chemgeo.2014.07.019`.

Miura, N., Y. Asahara, and I. Kawabe (2004). *Rare earth element and Sr isotopic study of the Middle Permian limestone-dolostone sequence in Kuzuu area, central Japan: Seawater tetrad sffect and Sr isotopic signatures of seamount-type carbonate rocks.*

Nebel, O., E. E. Scherer, and K. Mezger (2011). "Evaluation of the 87Rb decay constant by age comparison against the U-Pb system". In: *Earth and Planetary Science Letters* 301. DOI: `10.1016/j.epsl.2010.11.004`.

Ohno, T. and T. Hirata (2007). "Simultaneous determination of mass-dependent isotopic fractionation and radiogenic isotope variation of strontium in geochemical samples by multiple collector-ICP-mass spectrometry." In: *Analytical sciences : the international journal of the Japan Society for Analytical Chemistry* 23.

Palmer, M. and J. Edmond (1989). "The strontium isotope budget of the modern ocean". In: *Earth and Planetary Science Letters* 92. DOI: 10.1016/0012-821X(89)90017-4.

Pearce, C. R., G. D. Saldi, J. Schott, and E. H. Oelkers (2012). "Isotopic fractionation during congruent dissolution, precipitation and at equilibrium: Evidence from Mg isotopes". In: *Geochimica et Cosmochimica Acta* 92. DOI: 10.1016/j.gca.2012.05.045.

Pearson, N. J., W. L. Griffin, O. Alard, and S. Y. O'Reilly (2006). "The isotopic composition of magnesium in mantle olivine: Records of depletion and metasomatism". In: *Chemical Geology* 226. DOI: 10.1016/j.chemgeo.2005.09.029.

Pin, C. and C. Bassin (1992). "Evaluation of a strontium-specific extraction chromatographic method for isotopic analysis in geological materials". In: *Analytica Chimica Acta* 269. DOI: 10.1016/0003-2670(92)85409-Y.

Pogge von Strandmann, P. A., R. H. James, P. van Calsteren, S. R. Gíslason, and K. W. Burton (2008). "Lithium, magnesium and uranium isotope behaviour in the estuarine environment of basaltic islands". In: *Earth and Planetary Science Letters* 274. DOI: 10.1016/j.epsl.2008.07.041.

Pokrovsky, B. G., V. Mavromatis, and O. S. Pokrovsky (2011). "Co-variation of Mg and C isotopes in late Precambrian carbonates of the Siberian Platform: A new tool for tracing the change in weathering regime?" In: *Chemical Geology* 290. DOI: 10.1016/j.chemgeo.2011.08.015.

Saenger, C. and Z. Wang (2014). "Magnesium isotope fractionation in biogenic and abiogenic carbonates: implications for paleoenvironmental proxies". In: *Quaternary Science Reviews* 90. DOI: 10.1016/j.quascirev.2014.01.014.

Schmitt, A. D., N. Vigier, D. Lemarchand, R. Millot, P. Stille, and F. Chabaux (2012). "Processes controlling the stable isotope compositions of Li, B, Mg and Ca in plants, soils and waters: A review". In: *Comptes Rendus - Geoscience* 344. DOI: 10.1016/j.crte.2012.10.002.

Shields, G. and P. Stille (2001). "Diagenetic constraints on the use of cerium anomalies as palaeoseawater redox proxies: an isotopic and REE study of Cambrian phosphorites". In: *Chemical Geology* 175. DOI: 10.1016/S0009-2541(00)00362-4.

Slovak, N. M. and A. Paytan (2012). "Applications of Sr isotopes in archaeology". In: *Handbook of Environmental Isotope Geochemistry*. Vol. 2. Berlin, Heidelberg: Springer Berlin Heidelberg, pp. 743–768. DOI: 10.1007/978-3-642-10637-8_35. arXiv: arXiv:1011.1669v3.

Steiger, R. and E. Jäger (1977). "Subcommission on geochronology: Convention on the use of decay constants in geo- and cosmochronology". In: *Earth and Planetary Science Letters* 36. DOI: 10.1016/0012-821X(77)90060-7.

Teng, F.-Z. (2017). "Magnesium Isotope Geochemistry". In: *Reviews in Mineralogy and Geochemistry* 82. DOI: 10.2138/rmg.2017.82.7.

Tipper, E., A. Galy, J. Gaillardet, M. J. Bickle, H. Elderfield, and E. Carder (2006). "The magnesium isotope budget of the modern ocean: Constraints from riverine

magnesium isotope ratios". In: *Earth and Planetary Science Letters* 250. DOI: 10.
1016/j.epsl.2006.07.037.

Tipper, E. T., A. Galy, and M. J. Bickle (2008). "Calcium and magnesium isotope
systematics in rivers draining the Himalaya-Tibetan-Plateau region: Lithological
or fractionation control?" In: *Geochimica et Cosmochimica Acta* 72. DOI: 10.1016/
j.gca.2007.11.029.

Veizer, J., D. Ala, K. Azmy, P. Bruckschen, D. Buhl, F. Bruhn, G. A. Carden, A. Di-
ener, S. Ebneth, Y. Godderis, T. Jasper, C. Korte, F. Pawellek, O. G. Podlaha, and
H. Strauss (1999). "87Sr/86Sr, δ13C and δ18O evolution of Phanerozoic seawater".
In: *Chemical Geology* 161. DOI: 10.1016/S0009-2541(99)00081-9.

Vroon, P. Z., B. van der Wagt, J. M. Koornneef, and G. R. Davies (2008). "Problems
in obtaining precise and accurate Sr isotope analysis from geological materials using
laser ablation MC-ICPMS". In: *Analytical and Bioanalytical Chemistry* 390. DOI:
10.1007/s00216-007-1742-9.

Wombacher, F., A. Eisenhauer, F. Böhm, N. Gussone, M. Regenberg, W.-C. Dullo,
and A. Rüggeberg (2011). "Magnesium stable isotope fractionation in marine bio-
genic calcite and aragonite". In: *Geochimica et Cosmochimica Acta* 75. DOI: 10.
1016/j.gca.2011.07.017.

Wombacher, F., A. Eisenhauer, A. Heuser, and S. Weyer (2009). "Separation of Mg,
Ca and Fe from geological reference materials for stable isotope ratio analyses by
MC-ICP-MS and double-spike TIMS". In: *Journal of Analytical Atomic Spectrom-
etry* 24. DOI: 10.1039/b820154d.

Woodhead, J. D. (2002). "A simple method for obtaining highly accurate Pb isotope
data by MC-ICP-MS". In: *Journal of Analytical Atomic Spectrometry* 17. DOI:
10.1039/b205045e.

– (2008). "Isotope Ratio Determination in the Earth and Environmental Sciences:
Developments and Applications in 2006-2007". In: *Geostandards and Geoanalytical
Research* 32. DOI: 10.1111/j.1751-908X.2008.00919.x.

Young, E. D. and A. Galy (2004). "The Isotope Geochemistry and Cosmochemistry
of Magnesium". In: *Reviews in Mineralogy and Geochemistry* 55. DOI: 10.2138/
gsrmg.55.1.197.

Chapter 3

Radiogenic Sr, Stable C and O Iotopes across the Precambrian-Cambrian Transition in Marine Carbonatic Phosphorites of Malyi Karatau (Kazakhstan) - Implications for Paleo-environmental Change

Jessica A. Stammeier[1]*, Dorothee Hippler[1], Oliver Nebel[2], Albrecht Leis[3], Cyrill Grengg[1], Florian Mittermayr[4], Simone A. Kasemann[5], and Martin Dietzel[1]

[1] Institute of Applied Geosciences, Graz University of Technology, Rechbauerstraße 12, 8010 Graz, Austria

[2] School of Earth, Atmosphere and Environment, Monash University, Clayton VIC 3800, Australia

[3] JR-AquaConSol GmbH, Joanneum Research, Steyrergasse 21, 8010 Graz, Austria

[4] Institute of Technology and Testing of Building Materials, Graz University of Technology, Inffeldgasse 24, 8010 Graz, Austria

[5] MARUM–Center for Marine Environmental Sciences and Faculty of Geosciences, University of Bremen, Leobenerstraße 8, 28359 Bremen, Germany

*corresponding author email: j.stammeier@web.de

Abstract

The Precambrian-Cambrian (Pc-C) transition is a unique period in Earth's history known for the Cambrian Explosion, a revolutionary step for life on Earth. Concomitant with the Pc-C transition was the widespread deposition of continental margin phosphorites. Here, we present a continuous radiogenic and stable isotope (^{87}Sr/^{86}Sr, δ^{13}C$_{carb}$, δ^{18}O$_{carb}$) and elemental (incl. REE) record across the Pc-C transition, preserved in phosphatic and carbonate shallow-water deposits from two sections (Koksu and Kyrshabakty) of the Malyi Karatau, Kazakhstan. Fluctuation of trace and Rare Earth Element concentrations of the carbonate and phosphate phases of the sediment

and δ^{13}C$_{carb}$ data (-12.1 ‰ to 3.3 ‰; VPDB) record a time of rapid perturbations, indicative of geodynamic changes, and the onset of bioturbation. Average δ^{18}O$_{carb}$ values of -11.7 $\pm$ 3.8 ‰ (VPDB) are suggested to represent near primary signals and can be explained by isotopically lighter past sea water and elevated temperature during precipitation compared to present day conditions. ^{87}Sr/^{86}Sr$_{(i)}$ of the carbonate and phosphate fraction of this sedimentary sequence records are in the range of 0.7086 - 0.7112 at the Koksu section and 0.7082 – 0.7136 at the Kyrshabakty section, thus being in general agreement with the proposed seawater ^{87}Sr/^{86}Sr evolution during the early Cambrian. In this study, we present a new and refined ^{87}Sr/^{86}Sr seawater evolution, highlighting an extreme positive Sr isotope excursion at the Pc-C transition, which is suggested to be indicative for enhanced continental weathering accompanied by an increase in nutrient run-off into shallow ocean waters. This extreme geodynamic event may have served as a driving force for enhanced biologic activity in the lead up to the Cambrian Explosion, where phosphatic shallow-water deposits from Kazakhstan act as a valuable archive tracing the paleo-environmental conditions prior to this global event.

Keywords

Precambrian-Cambrian transition, ^{87}Sr/^{86}Sr seawater evolution, δ^{13}C, δ^{18}O, Cambrian Explosion, Phosphorite deposits

3.1 Introduction

The beginning of the Phanerozoic eon was initiated by a globally correlated change of the (bio-) geochemical system (Brasier, 1982; McMenamin, 1988; Morris, 1989; Morris, 1987; Runnegar, 1982). Similar to other stratigraphic transitions, the Precambrian -Cambrian transition (Pc-C) is marked by a mass extinction of the Ediacaran (635-541 Ma) fauna (Laflamme et al., 2013). This was followed by a rapid diversification of metazoan life during the Cambrian (541 – 485 Ma; e.g., Na and Kiessling, 2015), commonly referred to as Cambrian Explosion. While the actual developments during the Cambrian Explosion are well documented, potential causal relations with changes in paleo-ecology or possible geodynamic triggers for this event are still debated (Bengtson and Zhao, 1992; Dalziel, 2014; Filippelli, 2011; Fox, 2016; Sperling et al., 2015; X. Zhang et al., 2014). These may include both abiotic factors, such as changing seawater composition (in particular changes in dissolved Ca^{2+}, salinity, pH), nutrient availability, ocean circulation, enhanced weathering and continental run-off, as well as biotic factors such as the onset of predation or profound changes in biomineralization and bioturbation (Bottjer, 2010; Brasier, 1982; Mills and Canfield, 2014; Chen et al., 2015; Ohnemüller, 2014; Smith and Harper, 2013; X. Zhang et al., 2014).

Concomitant with these extensive changes in environmental conditions and geochemical cycles is the occurrence of massive phosphorite deposits (Cook and Shergold, 1986). Although phosphorite deposits (P_2O_5 > 18 wt. %, e.g. Jarvis et al., 1994) existed prior to the Phanerozoic, their occurrence is far more limited in the geologic record (e.g., Cook, 1992). Phosphorite deposits usually occur complementary to shallow-water deposits marking a transition between oxic (e.g.: carbonates) and anoxic deposits (e.g.: black shales, Cook and Shergold, 2005) and have previously been recognized as a valuable seawater archive (Barfod et al., 2002; Keto and Jacobsen, 1987; Komiya et al., 2008; Li et al., 2013; G. Shields, Stille, and Brasier, 1996; Wen et al., 2011). Deposition mechanisms of phosphorites are versatile and include direct precipitation, replacement of carbonates, microbial mediation or a combination of any of these processes, leading to a variety of depositional facies and rock textures (Bailey et al., 2013; Delaney, 1998; Föllmi, 1996; H. N. Schulz and H. D. Schulz, 2005; Trappe, 2001).

Predating these events was the break-up of the supercontinent Rodinia (ca. 750 Ma.), which led to the reorganization of numerous continental fragments with shallow continental shelves, thereby providing suitable environments for phosphorite deposition. Many of these former microcontinents, associated with records of the Pc-C transition, such as paleo-Kazakhstan, China (e.g. Yangtze Platform), Tarim, Mongolia and Siberia, were paleo-geographically located in close vicinity (Levashova et al., 2011; McKerrow, Scotese, and Brasier, 1992). The Pc-C-transition and its events have been extensively investigated by scientists of all geoscientific fields. Investigations focused mostly on the Yantgze Platform, South China (e.g.: Shen, Schidlowski, and Chu, 2000; Guo et al., 2007; Li et al., 2013; J. Zhang et al., 2016) and to a lesser extent on locations in present day Siberia (Derry et al., 1994; Nicholas, 1996), Mongolia (Brasier, G. Shields, et al., 1996; Goldring and Jensen, 1996) and Kazakhstan (Dzik, 2003; Heubeck, Ergaliev, and Evseev, 2013; Weber et al., 2013). Globally, the Pc-C transition is marked by a distinct negative $\delta^{13}C$ anomaly and high seawater $^{87}Sr/^{86}Sr$ values, which are generally discussed in the view of enhanced weathering rates or reworking of organic carbon (e.g., Derry et al., 1994; Jiedong et al., 1999; Halverson, Wade, et al., 2010; Zhu, Lu, et al., 2013; Li et al., 2013). Seawater $^{87}Sr/^{86}Sr$ reach a maximum at the Pc-C transition as a consequence of enhanced weathering during the Neoproterozoic (Derry et al., 1994; Halverson, Wade, et al., 2010; Halverson, Hurtgen, et al., 2009; Richter, Rowley, and DePaolo, 1992; Sawaki, Ohno, Tahata, et al., 2010). While this is generally accepted, the causality and the respective timing of oxygenation, weathering rates and the Cambrian Explosion is still debated, where increased oxygen contents is either a by-product of the Cambrian Explosion (Chen et al., 2015; Giezen and Lenton, 2012; Maruyama et al., 2014; Saltzman, 2005; Tatzel et al., 2017; J. Wang et al., 2012), or its driving force (Butterfield, 2009; Lenton and Watson, 2004). This carbon anomaly and high $^{87}Sr/^{86}Sr$ has also been recognized at two locations of Cambrian Kazakh strata (Gamper, 2014; A. V. Ilyin, 2004; Meert

et al., 2011; Ohnemüller, 2014), implying paleo-Kazakhstan was also exposed to globally occurring (weathering-related) processes. Although the stratigraphy of Kazakh strata is well constrained by fossil and sedimentological records (Dzik, 2003; Holmer et al., 1997; Popov et al., 2009; Weber et al., 2013), isotope and geochemical data are sparse (A. V. Ilyin, 2004; Meert et al., 2011).

In this study, we present the first continuous $^{87}Sr/^{86}Sr$ isotope record together with stable C and O isotopes and geochemical data for the Kazakh microcontinent covering the Precambrian-Cambrian transition. We investigate a suite of shallow-marine sedimentary successions from the Koksu and Kyrshabakty section, Malyi Karatau Range in Kazakhstan. Within these successions, we employ early Cambrian phosphorites as a seawater archive, aiming for the reconstruction of the depositional environment changes and possible inferences for mechanisms that initiated the Cambrian Explosion.

3.2　Location and Sample Description

Paleogeographic reconstruction for the Pc-C interval and apparent similarities of ichnofacies and depositional environments place the Kazakh microcontinent in lower to mid-latitudes of the northern hemisphere close to the well investigated Yangtze Platform of South China (Levashova et al., 2011; Li et al., 2013; Weber et al., 2013).

The herein investigated sections Koksu (43° 39' 13.0" N, 69° 38' 11.0" E) and Kyrshabakty (43° 32' 2.1" N, 69° 57' 7.7" E) are located in the NW part of the Malyi Karatau mountain range in southern Kazakhstan (Figure 3.1). This part of the mountain range is thought to have undergone few thermal and tectonic events (Alexeiev et al., 2009; Heubeck, Ergaliev, and Evseev, 2013; Weber et al., 2013). Here, the Pc-C boundary (541 Ma.) is defined by the FAD of the index fossil Trichophycus pedum (e.g., Landing, 1994) and co-occuring SSF-assemblages in the early Cambrian Chuluktau Formation and can be correlated to the Meishucunian sequence on the Yangtze platform (Weber et al., 2013). The 50 m profile at Koksu is located within several exploration trenches and an open-pit mining site, providing access to a continuous record of the Chulaktau Formation. Stratigraphically, the Chulaktau Formation follows the Precambrian Kyrshabakty Formations, which are mainly composed of siliciclastics, silicic volcanics and carbonates (Figure 3.1). The Chulaktau Formation is divided into six units, from base to top: (1) Aksai Chert, (2) Lower Phosphorite, (3) Shale Member, (4) Upper Phosphorite, (5) Fe-Mn Horizon and (6) Brown Dolomite (Heubeck, Ergaliev, and Evseev, 2013). Sedimentary rocks comprise a succession of dolostones (cf. Heubeck, Ergaliev, and Evseev, 2013), overlain by bedded, dark-colored cherts, the minable phosphorite units with an intercalated phosphate-bearing siltstone and shale unit. The Upper Phosphorite is topped by a Fe-Mn-carbonate and dolostone horizon, which was deposited in a shallow marine archipelago setting

(Heubeck, Ergaliev, and Evseev, 2013). The Cambrian Shabakty Formation comprising thick dolo- and limestones overlies the Chulaktau Formation. A brief description of the sampled lithology is included in Table 3.1.

The nearby Kyrshabakty section consists of a ca. 500 m thick succession covering Neoproterozoic to Cambrian sedimentary suites, including from base to top the Kyrshabakty, Chulaktau and Shabakty Formation. The Kyrshabakty Formation comprises in the lower part diamictites, pink cap dolomites, an alternating succession of dolomitic sandstones and sandy dolostones, followed by phosphate-bearing sandy limestones in the middle part, topped by the Berkuty Dolomite in the upper part. The successive Chuluktau and Shabakty Formation correspond to the same Formations as at the Koksu section, however, are not continuously exposed at the Kyrshabakty section. Samples from the Kyrshabakty section were investigated in the course of a dissertation by Frank Ohnemüller in 2014. With permission, Sr isotope data and the respective $\delta^{13}C$ and $\delta^{18}O$ will be included into this study. A brief description of the methodology is included. For a more detailed description of location and samples see Ohnemüller (2014).
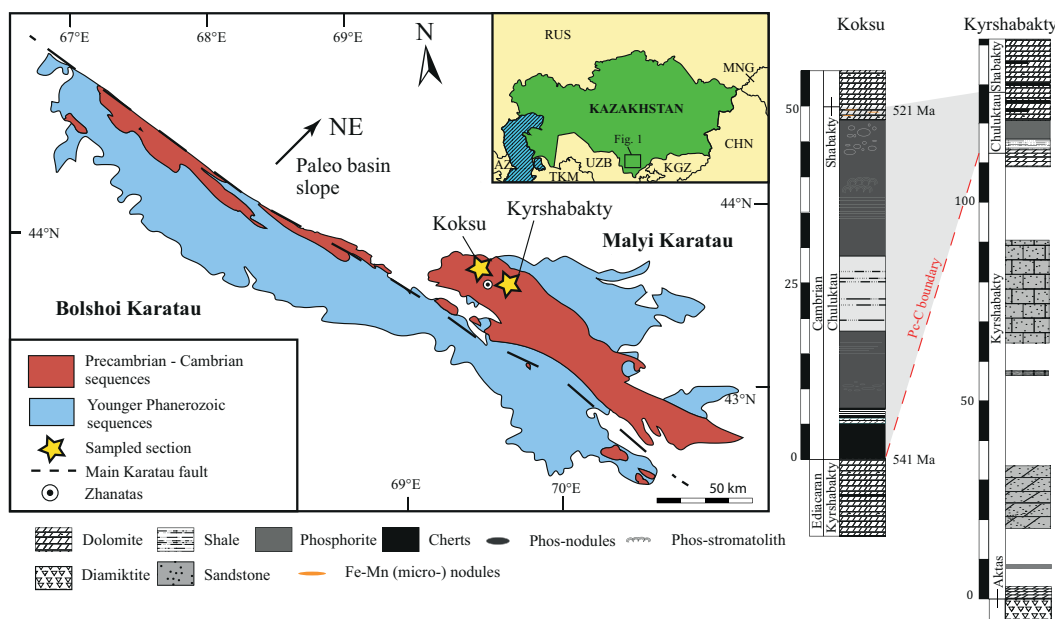
FIGURE 3.1: Schematic geologic map of the Malyi and Bolshoi Karatau Mountain range located in southern Kazakhstan (simplified after Eganov and Sovetov, 1986) and lithostratigraphic columns of the Koksu (left) and Kyrshabakty (right) locations. The black arrow (marked with NE) indicates the direction of the deepening paleo-basin, reaching deep waters in the far NE (central Kazakhstan). The Koksu and Kyrshabakty sections are located at the margin of a former shallow water basin (Eganov, Sovetov, and Yanshin, 1986).

Additionally, we complemented our data with a subset of phosphorite samples from South Chinese sections at Xiaofenghe and Zhangunping. These two sections are part of the Huangling Anticline in the Three Gorges area, located in the NE of the Yangtze Platform and comprise late Neoproterozoic to early Paleozoic marine successions (Figure 3.2). The investigated samples were deposited in shallow-marine

intra-basin settings and are part of the Ediacaran Doushantuo Formation (Xiao et al., 2012; Zhu, J. Zhang, and Yang, 2007).
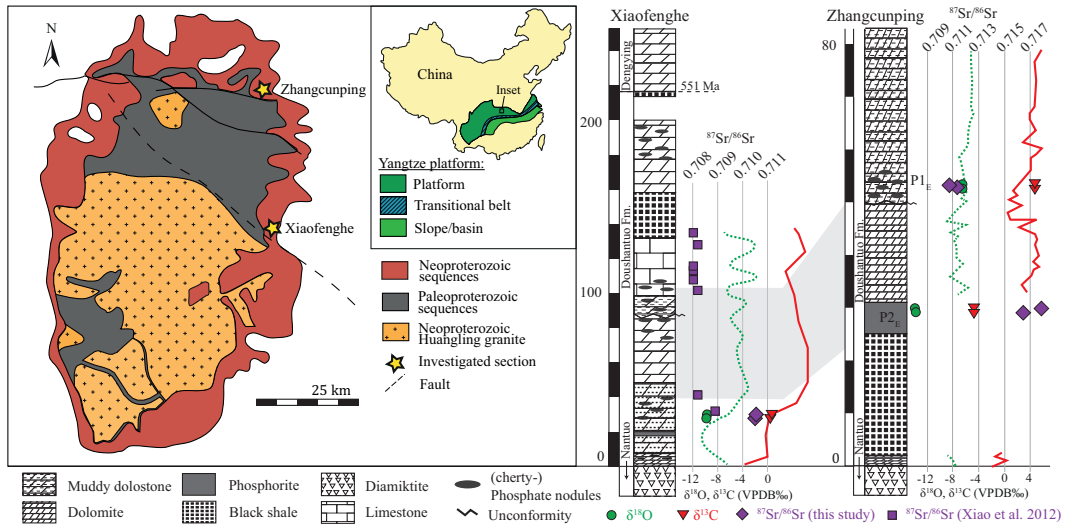
FIGURE 3.2: Schematic geologic map of the Huangling Anticline complex in the northern part of the Yangtze Platform, China. Map, stratigraphic profiles, $\delta^{13}C_{carb}$ (solid line), $\delta^{18}O_{carb}$ (dotted line) and $^{87}Sr/^{86}Sr$ (squares) data after Xiao et al. (2012) and Zhu, J. Zhang, and Yang (2007). $\delta^{13}C_{carb}$ (triangles), $\delta^{18}O_{carb}$ (circles) and $^{87}Sr/^{86}Sr$ (diamonds): this study.

3.3 Methodology

3.3.1 Characterization of the solids and elemental analysis

Bulk mineralogical composition of all samples was determined by petrographic investigations and qualitative X-ray diffraction (XRD) analyses using a PANalytical X'Pert PRO diffractometer, equipped with a Co-tube (40 kV and 40mA), a spinner stage, 0.5° divergence and anti-scattering slits, and a Scientific X'Celerator detector. Randomly oriented preparations were recorded over the range of 4-85°2θ with a step size of 0.0170°2θ. Mineral identifications were carried out using the PANalytical X'Pert HighScore software (version 3.0d). Polished thick sections of two selected samples (KO10 & KO13) were further investigated with electron probe microanalyses (EPMA) using a JEOL JXA-8200 Superprobe. (Semi-) quantitative element distribution images of Ca, Mg, F, P and Si were conducted using the wave dispersive analytical mode, with an accelerating voltage of 15.0 kV and a beam current of 30 nA. In addition, 94 single spot analyses, evenly distributed within the aggregates and the surrounding matrix of the two samples, were carried out at 15 kV and 5 nA. The quantification of individual elemental concentrations in weight % was performed against mineral standards from SPI (dolomite for Mg, celestine for Sr and S, tugtupite for Cl, fluorapatite for F, Ca and P).

For chemical bulk analysis macroscopically pristine samples were chosen and crushed with an industrial jaw crusher to a fine powder. To avoid cross-contamination, the first fractions of each sample was run through the crusher and disposed. For chemical analysis ca. 50 mg powder were weighted and treated with minor amounts of concentrated HNO_3 to drive away the CO_2. The sample was quickly dried down and leached in 3 mol l^{-1} HNO_3 for 24 h. The insoluble residue was separated by centrifugation, dried and weighted again and subtracted from the initial sample weight. The leached acid, further referred to as the acid soluble fraction, was subsequently used for all elemental and Sr isotopic analysis. 10% aliquots of the acid soluble fraction were used to measure main and trace elements including REE. Elemental analyses were performed at the Central Laboratory for Water, Minerals and Rocks, NAWI Graz. Trace elements and REE were analysed using inductively coupled plasma mass spectrometry (ICP-MS, Agilent 7500cx) with an analytical precision generally better than ± 5%. Total main elemental concentrations were analysed by inductively coupled plasma optical emission spectroscopy (ICP-OES) using a PerkinElmer Optima 8300 with an analytical precision of ± 2%. Standardization was performed using single element standards (Merck and Fluka) for main elements and a customized multi element solution (analytik jena) for trace and REE. To ensure reproducibility repeated measurements of reference solution SPS SW1 (Spectrapure Standards) were performed.
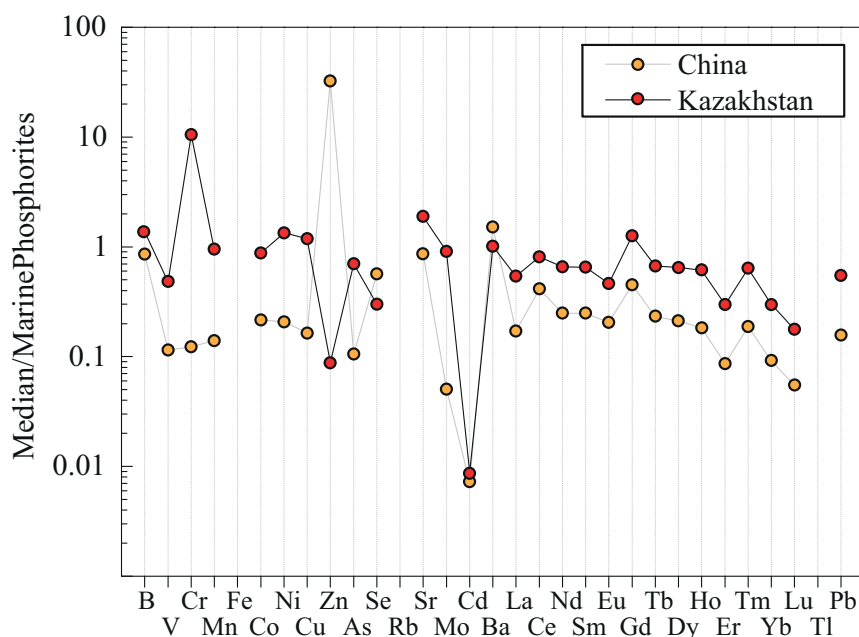
FIGURE 3.3: Median of trace and rare earth elements normalized to average marine phosphorites (compare Table 3.2, Altschuler, 1980; Yuan-Hui, 1991). The Zn enrichment in the Chinese samples is due to abundant pyrite in one sample.

Enrichment factors for trace elements (Figure 3.3) were calculated using the phosphorite composition of Altschuler (1980). Enrichment factors for REE (Figure 3.4, Appendix Table B.3) were calculated relative to PAAS (McLennan, 2001) as $Ce/Ce* =$

$(3 * Ce_N)/((2 * La_N + Nd_N))$ (after G. Shields and Stille, 2001), $MREE/MREE* = (2 * Gd_N)/((Sm_N + Ho_N))$, and $HREE/HREE* = (La_N + Nd_N)/(Tm_N + Lu_N)$.
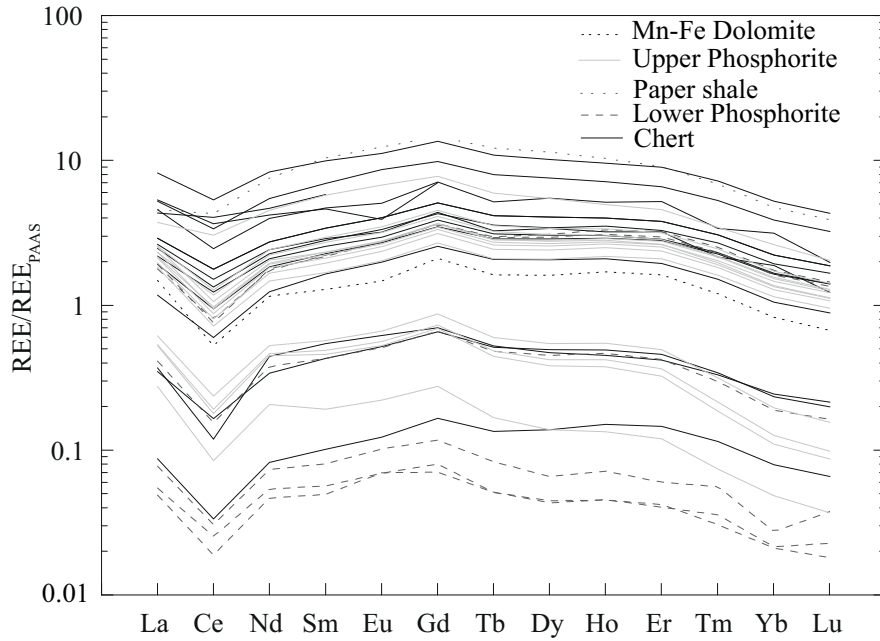
FIGURE 3.4: REE_N pattern of the acid soluble fraction grouped into respective horizons. Generally, REE_N enrichment is more pronounced in the Upper Phosphorite than the Lower Phosphorite. This enrichment likely mirrors the presence of a phosphatic matrix in the Upper Horizon.

3.3.2   Stable carbon and oxygen isotopes

The stable carbonate-carbon and -oxygen isotope ratios of the solid samples from Koksu were determined on a Thermo Fisher Scientific Gas Bench II carbonate preparation device connected to a Finnigan DELTAplus XP isotope ratio mass spectrometer at the JR-AquaConSol GmbH, Joanneum Research. For the analysis ca. 20 μg of bulk sample were dissolved in concentrated phosphoric acid and analysed for their respective oxygen and carbon isotope ratios. Analytical details can be found in Dietzel et al. (2016). The overall precision (2 S.D.) for the measurements of $\delta^{13}C_{carb}$ and $\delta^{18}O_{carb}$ is $\pm$ 0.1 ‰ and $\pm$ 0.08 ‰ determined on reference materials NBS 18 and NBS 19 (NIST), respectively. For the Kyrshabakty section, solid samples were analysed on a Thermo Finnigan Gas Bench I linked to a Thermo Finnigan DELTA Visotope mass spectrometer at the Museum für Naturkunde Berlin. The analytical precision (2 S.D.) for the measurements of $\delta^{13}C_{carb}$ and $\delta^{18}O_{carb}$ was better than $\pm$ 0.2 ‰. Carbon and oxygen isotope ratios are reported in the δ-notation as per mil (‰) deviation relative to the Vienna Pee Dee Belemnite standard (VPDB). Carbonate contents for samples KO 01, 22, 25, 30, 34 were too low to be determined.

3.3.3 Radiogenic strontium isotopes

To investigate the radiogenic Sr isotopic signature of the different phases in phosphorite and evaluate Sr contribution of cemented micro-fractures, a two-step acid leaching approach, using 0.05 mol l^{-1} and 3 mol l^{-1} HNO$_3$, respectively, was employed in a pre-study. The ^{87}Sr/^{86}Sr isotopic composition is systematically higher in the weak acid leachates (0.05 mol l^{-1}), yet identical for the two acid leachates within the analytical precision (2 S.D.). Based on these results we continued leaching with 3 mol l^{-1} HNO$_3$to capture phosphate-carbonate phases, representative for authigenic Sr and avoid dissolution of the detrital silicate cargo, which may carry a distinct radiogenic ^{87}Sr/^{86}Sr isotopic composition.

For the samples of the Koksu section, Sr was separated using Sr-specific extraction chromatographic resin (Eichrom) using 5 ml of 3 mol l^{-1} HNO$_3$for element elution and 1 ml MilliQ for Sr collection (Pin and Bassin, 1992). Strontium isotopic ratios were determined on a Plasma II MC-ICP-MS instrument (Nu Instruments, Wexham, UK) at the Graz University of Technology, Austria. Measurements were performed with a static cup configuration in wet-plasma mode. ^{87}Sr/^{86}Sr are reported relative to a value of 0.710250, the recommended value for NBS 987 (Hans, 2013). The measurement uncertainty of an analytical session was generally $\pm$ 75 ppm, expressed as 2 S.D. Reproducibility of seawater was within 100 ppm (2 S.D.) relative to a ^{87}Sr/^{86}Sr value of 0.70924 $\pm$ 0.00003 (Elderfield, 1986).

For samples from the Kyrshabakty section, samples were dissolved in 2 mol l^{-1} HNO$_3$, corresponding to the carbonate and phosphate fraction of the rock samples. Strontium was separated using the separation method by Pin and Bassin (1992) and Deniel and Pin (2001). Measurements were performed on a Thermo Fisher Scientific TRITON Plus mass spectrometer with Re single filaments with a Ta emitter at the University of Bremen. For Sr isotope measurements at the University of Bremen repeatability of NIST 987 was ^{87}Sr/^{86}Sr = 0.710250 $\pm$ 0.000016 (2 S.D., n=113). The total procedural blank was below 1.2 ng Sr and negligible. Instrumental mass fractionation at both labs was performed in-run in 6 iterative steps to an 86Sr/88Sr value of 0.1194.

3.4 Results

3.4.1 Microstructure and mineralogy

Results from qualitative bulk XRD analysis characterize the main components as carbonate-fluorapatite (CFA), calcite and/or dolomite, quartz and in some cases traces of ankerite (Table 3.1). While the matrix of the Lower Phosphorite member is composed of calcite and/or dolomite, the matrix of the Upper Phosphorite Member mainly consists of CFA. Petrographic investigations (SEM, thin section) show good preservation of CFA nano-crystals and carbonates, indicating a nearly pristine

internal structure. Rock facies is dominated by granular phosphorites, ranging from well-sorted phos-grainstones (e.g., KO 10, Appendix Figure B.1) to poorly sorted flat pebble phos-rudstones (e.g., KO 13, Figure 3.5, Appendix Figure B.1). Phosphate grains within these sedimentary rocks include phosphatic clasts, peloids and coated grains, such as oncoids and ooids (Figure 3.5). In most samples, the dolomite matrix forms a mosaic structure of anhedral grains. Overall, rock fabrics show the characteristics of moderately to high energy, shallow water environment depositions, with pronounced phosphogenesis and hints for bioturbation towards the upper part of the profile. Microfabrics and composition shows an almost primary sedimentary sequence suggesting near-primary preservation.
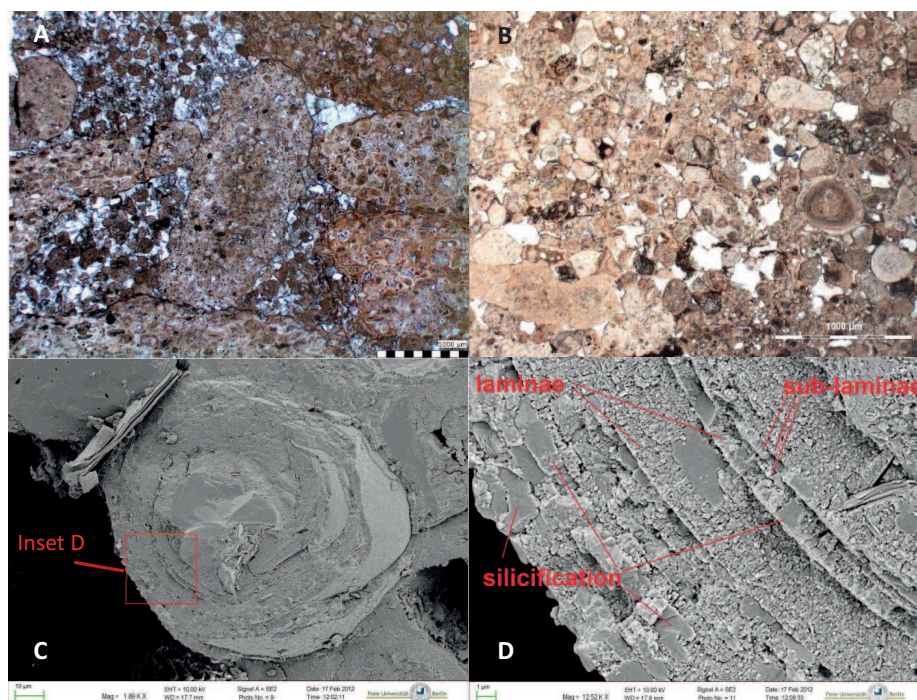
FIGURE 3.5: Microphotographs (transmitted light) and scanning electron microscopy images of phosphorite fabrics. (A) Poorly sorted flat-pebble phos-rudstone (KO 13) exhibiting well-rounded gravel-sized phos-clasts, as well as phos-peloids in sparry dolomite; (B) Moderately-sorted phos-rudstone (KO 58) with phos-clasts, -peloids and -ooids; (C+D) Phos-ooid (KO 44) showing the preservation of CFA nano-crystals indicating a mostly pristine internal structure.

3.4.2   Element abundances

All measured elemental data are summarized in Appendix Table B.1, B.2 and B.3. Note that geochemical analyses reflect results from acid soluble fractions. Element abundances support the above reported mineralogy and additionally indicate the presence of accessory phases not captured by XRD. Element correlations indicate these accessory phases may be Na, Fe-rich glauconite phases, albitic feldspars or

TABLE 3.1: Descriptive lithology of hand specimens and major mineral phases from qualitative XRD results. Note that the order of minerals does not reflect quantitative results. Height refers to position within the profile with 0 m set to the visible profile base. Phosphorite classification after Trappe (2001).

Sample	Height [m]	Lithologic description	Member	Section	Mineralogy	Phosphorite Classification
Kazakhstan:						
KO 01	1.4	phosphatic chert	Aksai Chert	Koksu	quartz, CFA, calcite	
KO 02	1.8	phosphatic chert	Aksai Chert	Koksu	quartz, CFA, calcite	
KO 22	0.8	phosphatic chert	Aksai Chert	Koksu	n.d.	
KO 25	1.4	phosphatic chert	Aksai Chert	Koksu	n.d.	
KO 03	2.1	phosphatic chert	Aksai Chert	Koksu	quartz, CFA, dolomite, calcite	
KO 30	2	phosphatic chert	Aksai Chert	Koksu	n.d.	
KO 34	1.4	phosphatic chert	Aksai Chert	Koksu	n.d.	
KO 04	0	cherty dolomite	Aksai Chert	Koksu	quartz, CFA, dolomite	
KO 05	0	phosphatic dolomite	Aksai Chert	Koksu	quartz, CFA, dolomite	
KO 06	3.6	phosphatic chert	Aksai Chert	Koksu	quartz, CFA, dolomite, calcite	
KO 07	1.0	phosphatic chert	Aksai Chert	Koksu	quartz, CFA, dolomite	
KO 08	5.2	phosphatic banded chert	Aksai Chert	Koksu	quartz, CFA, dolomite, ankerite, calcite	
KO 09	4	phosphatic platy chert	Aksai Chert	Koksu	quartz, CFA, dolomite, calcite	
KO 10	7.8	contact dolomite/phosphorite	Lower Phosphorite	Koksu	quartz, CFA, dolomite, calcite	Phospeloid grainstone
KO 11	8.4	phosphorite	Lower Phosphorite	Koksu	quartz, CFA, dolomite, calcite,	Phospeloid grainstone
KO 12	8.6	dolomitic phosphorite	Lower Phosphorite	Koksu	quartz, CFA, dolomite, calcite,	Phospeloid grainstone
KO 13	9.95	phosphatic. flat pepples	Lower Phosphorite	Koksu	quartz, CFA, dolomite, calcite	Phospeloid rudstone
KO 14	13.2	dense phosphorite	Lower Phosphorite	Koksu	quartz, CFA, calcite	Phospeloid grainstone
KO 15	15.4	platy phosphorite	Lower Phosphorite	Koksu	quartz, calcite, CFA,	Phospeloid grainstone wt phos. bindstone
KO 16	17.5	phosphorite	Lower Phosphorite	Koksu	quartz, CFA, calcite	Phospeloid grainstone
KO 36	25	phosphate –bearing siltstone	Phosphorite - Shale	Koksu	quartz, CFA, orthoclase, muscovite,	
KO 42	32.6	phosphorite	Upper Phosphorite	Koksu	n.d.	
KO 43	34.2	bedded phosphorite	Upper Phosphorite	Koksu	quartz, CFA	Phospeloid grainstone wt phos. bindstone
KO 44	34.6	bedded phosphorite	Upper Phosphorite	Koksu	quartz, CFA	Phospeloid grainstone wt phos. bindstone
KO 45	35.6	dense phosphorite	Upper Phosphorite	Koksu	quartz, CFA	Phospeloid grainstone
KO 46	36.4	phosphorite	Upper Phosphorite	Koksu	quartz , CFA	Phospeloid grainstone
KO 50	39.3	phosphorite	Upper Phosphorite	Koksu	quartz, dolomite, CFA, calcite	Phospeloid grainstone wt phos. bindstone
KO 51	39.6	stromatolithic phosphorite	Upper Phosphorite	Koksu	quartz, CFA, calcite	Phospeloid grainstone wt phos. bindstone
KO 52	40.5	stromatolithic phosphorite	Upper Phosphorite	Koksu	quartz, CFA, dolomite, calcite	Phospeloid grainstone wt phos. bindstone
KO 56	42.5	bedded phosphorite	Upper Phosphorite	Koksu	quartz, CFA, feldspar, illite, magnesite	Phospeloid grainstone
KO 57	44	granular, porous phosphorite	Upper Phosphorite	Koksu	n.d.	Phospeloid grainstone
KO 58	44.8	granular, porous phosphorite	Upper Phosphorite	Koksu	n.d.	Phospeloid grainstone
KO 59	46.8	phosphatic pebbles	Upper Phosphorite	Koksu	n.d.	Phospeloid grainstone
KO 60	47.6	phosphatic pebbles	Upper Phosphorite	Koksu	quartz, CFA, dolomite	Phospeloid rudstone
KO 62	48.3	Dol. wt Mn-Fe (micro-) nodules	Fe-Mn Horizon	Koksu	quartz, CFA, dolomite, calcite	
KO 64	49	Dolomite	Brown Dolomite	Koksu	quartz, dolomite,	
KO 65	51	Dolomite	Brown Dolomite	Koksu	quartz, dolomite, ankerite	
China:						
NXF 1204		phosphatic sandstone		Xiaofenghe		
NXF 1202		phosphatic sandstone		Xiaofenghe		
ZCP 1202		phosphorite pebbles		Zhancunping		
ZCP 1203		phosphorite pebbles		Zhancunping		
ZCP 1217		phosphatic chert		Zhancunping		
ZCP 1215		phosphatic chert		Zhancunping		

Fe-Mn (micro-) nodules (Rothwell, 1989). The presence of the three main minerals calcite, dolomite and CFA was confirmed and quantitatively determined, including chemical formulas, in two samples by EMPA analysis (Appendix Figure B.1, B.1 and Table B.5). The presence of F within CFA was also determined by EPMA with an average of 3.4 wt. %. Strontium concentrations of the acid soluble fraction are ranging from 775 ppm to 7045 ppm. Quantitative element distribution images (Appendix Figure B.1, B.1) and EMP spot analysis show that Sr is predominantly incorporated into CFA and is generally in the range of 0.2 – 0.3 wt. % SrO and below the detection limit of ca. 400 ppm in the calcite and dolomite matrix. The insignificant contribution of dolomite to bulk Sr is further confirmed by the lack of correlation between Sr and MgO contents, assuming near constant Sr/Mg in dolomite (Figure 3.6).
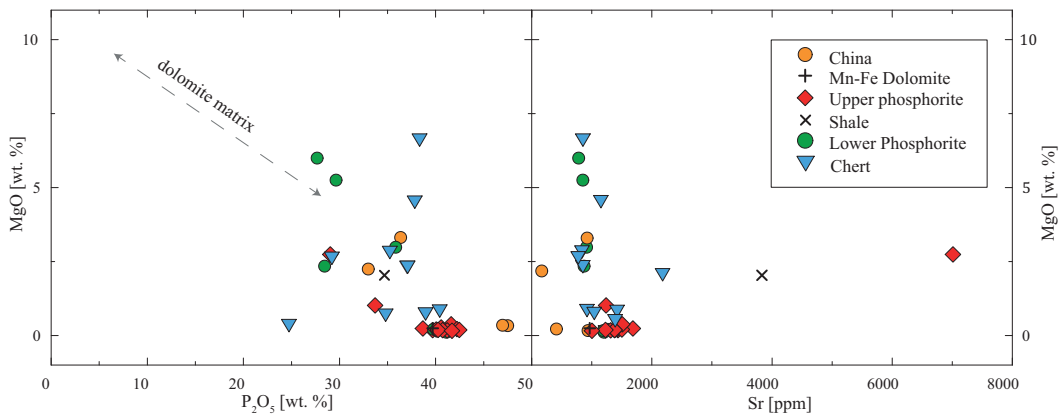
FIGURE 3.6: P_2O_5 contents show no systematic difference between the upper and lower Phosphorite horizon. Three outlier samples with MgO >10 wt.% are outside the presentable ranges. A negative correlation between MgO and P_2O_5, more pronounced for the Chert and the Lower Phosphorite, is in agreement with the presence of a dolomitic matrix. A lack of correlation between MgO and Sr concentrations underlines that Sr is not strongly incorporated into the dolomite matrix compared to CFA components and calcite matrix.

REE abundances (Appendix Table B.3) of the acid soluble fraction are displayed relative to the Post-Archean-Australian Shale (PAAS) composite in Figure 3.4 (McLennan, 2001). Total REE (ΣREE) contents of Kazakh samples show both depletion and up to ten fold enrichment relative to PAAS. ΣREE enrichment of the Upper Phosphorite Horizon (0.2 – 4.7) is generally higher than in the Lower Phosphorite horizon (0.1 – 2.4). Rare Earth element patterns resemble those of typical "old phosphorites" as termed by A. Ilyin (1998) with a typical negative Ce anomaly (0.3 – 0.8), relative MREE enrichment (1.3 – 1.7) and HREE depletion (0.9 – 4.4; Figure 3.4, Appendix Table B.3). ΣREE contents of Kazakh samples, with 282 ppm, are lower than in Chinese samples, with 111 ppm.

3.4.3 Stable carbon and oxygen isotopes of carbonate

Carbonate stable isotope values ($\delta^{13}C_{carb}$ and $\delta^{18}O_{carb}$) are displayed in Figure 3.7 and Figure 3.9 (Appendix Table B.4). At Koksu $\delta^{13}C_{carb}$ values record minor oscillation with a slight decrease at each horizon transition. $\delta^{13}C_{carb}$ (VPDB) range from -1.2 ‰ (Upper Phosphorite Horizon) to -12.1 ‰ (Chert Horizon), $\delta^{18}O_{carb}$ range from -5.7 ‰ to -17.3 ‰ (VPDB), with a positive correlation of $\delta^{13}C_{carb}$ and $\delta^{18}O_{carb}$ (R^2 =0.78, Figure 3.7).
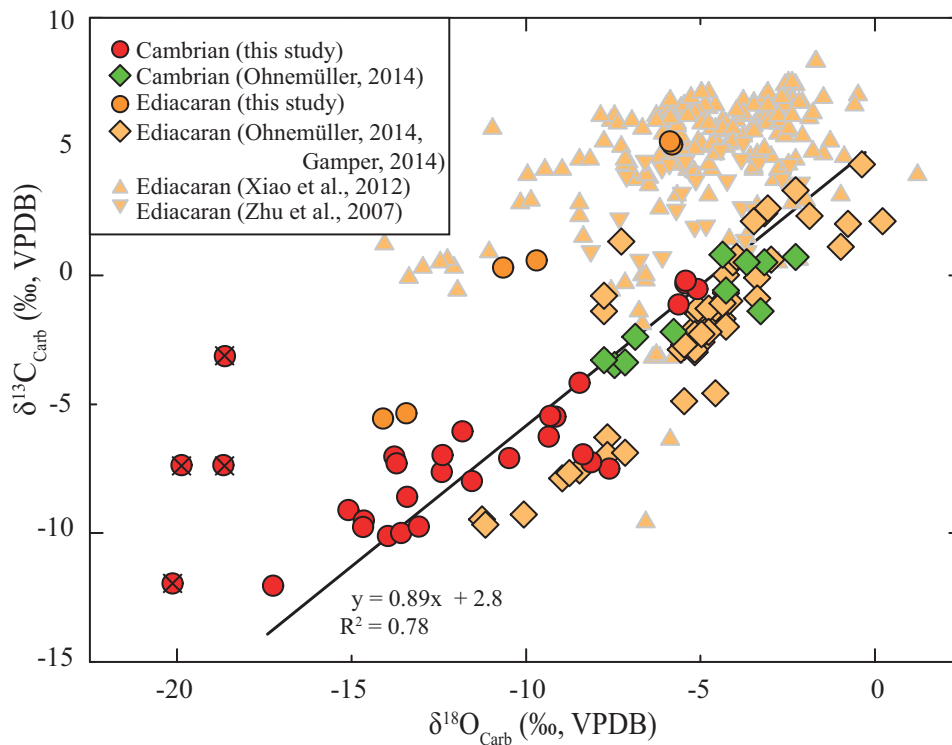
FIGURE 3.7: $\delta^{13}C_{carb}$ and $\delta^{18}O_{carb}$ values of marine sedimentary sequences of Kazakhstan and China. Cambrian data from Koksu section, Kazakhstan (this study) and Kyrshabakty, Kazakhstan (Ohnemüller, 2014). Ediacaran data from Berkuty section, Kazakhstan (Gamper, 2014), Kyrshabakty section, Kazakhstan (Ohnemüller, 2014), Xiaofenghe section, China (Xiao et al., 2012) and Zhancumping section, China (Zhu, J. Zhang, and Yang, 2007). Four samples with abnormal values are omitted from interpretation (this study).

$\delta^{13}C_{carb}$ and $\delta^{18}O_{carb}$ values of the Xiaofenghe and Zhangunping sections (this study) display variable values of -5.6 to 5.1 ‰ for $\delta^{13}C_{carb}$ and -14.1 to -5.8 ‰ for $\delta^{18}O_{carb}$ and correlate with the globally recognized negative $\delta^{13}C$ excursion in the lower Ediacaran (compare Gamper et al., 2015). The two samples from the Xiaofenghe section are identical to reported values of ca. 0 ‰ for $\delta^{13}C_{carb}$ and -6 ‰ for $\delta^{18}O_{carb}$ (Figure 3.2; Xiao et al., 2012). Two samples of the upper phosphorite (P1E) at the Zhangunping section are also identical to values of ca. 4 ‰ for $\delta^{13}C_{carb}$ and -4 ‰ for $\delta^{18}O_{carb}$ (Figure 3.2; Zhu, J. Zhang, and Yang, 2007). In a $\delta^{13}C$ vs. $\delta^{18}O$ diagram, reported values of Chinese Ediacaran phosphorites and carbonates plot in a cluster without any apparent co-variation, which is consistent with a time marked by several global

negative δ^{13}C excursions (Figure 3.7; Xiao et al., 2012; Zhu, J. Zhang, and Yang, 2007).

3.4.4   Radiogenic strontium isotopes

The initial ^{87}Sr/^{86}Sr$_{(i)}$ of the acid soluble fraction from the Koksu profile were corrected to an age of 541 Ma and range from 0.7086 to 0.7112, and are displayed in Appendix Table B.4 and Figure 3.8. ^{87}Sr/^{86}Sr$_{(i)}$ values show a decrease towards less radiogenic ratios after the Pc-C transition (Figure 3.8). The Rb/Sr is low with values ranging from 0.0001 to 0.018, with an average of 0.0028 (Table 3.2).

^{87}Sr/^{86}Sr values from the Kyrshabakty profile range from 0.7083 to 0.7137 (Table 3.2). The highest ^{87}Sr/^{86}Sr values ($>$0.712) are observed in mid-Ediacaran carbonates, with a subsequent drop of ^{87}Sr/^{86}Sr values to ca. 0.709 in terminal Ediacaran and Cambrian sequences. Rb/Sr ratios for this section are not available, however Rb ion concentrations in carbonate and phosphate minerals are expected to be low as it is not compatible in either phase. For calculation of initial ^{87}Sr/^{86}Sr values the average Rb/Sr ratio from the Koksu section was employed. Note, that these ^{87}Sr/^{86}Sr$_{(i)}$ can only be regarded as minimum values. Ediacaran phosphorite samples from the Chinese sections also record high ^{87}Sr/^{86}Sr$_{(i)}$ values from 0.7106 to 0.7174 at the Zhangcunping section and 0.7103 to 0.7110 at the Xiaofenghe section, respectively. Our values for Zhangcunping and Xiaofenghe are thus similar to reported values in the range from 0.7118 to 0.7137 during the coeval Shuram-Wonoka event of the mid-Ediacaran period at the Kyrshabakty section.

3.5   Discussion

3.5.1   Diagenetic constraints

During precipitation and deposition, marine authigenic carbonates and phosphates trap and thereby trace the seawater geochemical and isotope composition. During and after deposition these signatures might be altered during diagenesis through meteoric or post-depositional burial (high-T) and associated fluid-rock interaction. Assessing this alteration is not straightforward as both, the composition of the fluids from which the phases initially precipitated as well as the composition and temperature of the potentially modifying fluids have to be taken into account. During lithification of sediments, i.e., the transformation of meta-stable to stable minerals, authigenic minerals undergo dissolution - (re-)precipitation, accompanied by re-adjustment of their isotope and chemical composition with the ambient pore water (Knauth and Kennedy, 2009).

TABLE 3.2: Summary of average and median contents by location, reported with the respective minimum (min) and maximum (max) values, and the overall variation, expressed as standard deviation. n refers to the number of samples used for the respective calculation. (m) = measured, (i) = initial (541 Ma). $^{87}Sr/^{86}Sr$ data from Kyrshabakty section as reported in Ohnemüller (2014). For a detailed list of all isotope values see Appendix Table B.

	Average	Median	Variation	min	max	n	Average	Median	Variation	min	max	n
							China:					
Kazakhstan, Koksu:												
B (ppm)	21.9	15.8	23.1	2.39	116	31	13.7	12.0	9.17	2.72	26.1	6
V (ppm)	60.7	18.4	93.5	4.67	437	35	11.5	11.1	4.28	6.46	17.0	6
Cr (ppm)	883	89.1	1973	9.61	8438	35	15.3	16.5	5.12	7.08	21.2	6
Mn (ppm)	1305	674	1449	130	5989	35	173	137	126	17.2	367	6
Co (ppm)	6.02	2.15	9.37	0.78	39.9	35	1.52	0.99	0.84	0.90	3.06	6
Ni (ppm)	53.5	16.9	87.1	6.89	339	35	11.0	8.74	4.19	6.40	17.5	6
Cu (ppm)	71.0	9.03	177	3.12	1009	35	12.4	5.46	14.5	2.71	43.5	6
Zn (ppm)	20.0	9.40	30.4	3.41	152	35	6245	36.40	13882	5.59	37286	6
As (ppm)	16.0	5.92	34.8	0.38	189	35	2.43	1.28	2.20	0.56	6.74	6
Se (ppm)	1.61	1.66	1.37	0.14	6.74	34	2.60	0.61	4.53	0.25	12.7	6
Rb (ppm)	4.99	2.21	8.89	0.08	39.5	34	6.95	6.01	5.42	0.79	17.8	6
Sr (ppm)	1396	1238	1115	102	7045	35	649	668	385	158	1188	6
Mo (ppm)	6.85	2.64	10.3	0.15	41.1	31	0.45	0.32	0.32	0.16	0.97	6
Cd (ppm)	0.13	0.06	0.17	0.02	0.81	31	0.13	0.09	0.12	0.01	0.34	6
Ba (ppm)	447	152	647	13.4	2311	35	532	367	503	16.6	1231	6
Tl (ppm)	0.07	0.03	0.09	0.00	0.4	31	0.02	0.02	0.01	0.00	0.03	6
Pb (ppm)	33.7	15.9	59.4	2.31	313	35	7.84	3.33	9.19	2.10	27.9	6
ΣREE	322	265	308	5.73	1281	33	111	83.7	74.0	34.0	235	6
$\delta^{13}C_{carb}$	-7.6	-7.4	2.4	-12.1	-1.2	35	0.0	0.5	4.4	-5.6	5.2	6
$\delta^{18}O_{carb}$	-11.7	-12.4	3.8	-17.3	-5.7	35	-10.0	-10.2	3.26	-14.1	-5.83	6
$^{87}Sr/^{86}Sr_{(m)}$	0.70909	0.70902	0.00031	0.70865	0.71012	34	0.71285	0.71108	0.00294	0.71049	0.71746	34
$^{87}Sr/^{86}Sr_{(i)}$	0.70914	0.70902	0.00045	0.70864	0.71119	33	0.71260	0.71083	0.00296	0.71014	0.71740	33
Rb/Sr	0.0029	0.0017	0.0041	0.0001	0.0183	27	0.0115	0.0115	0.0064	0.0029	0.0189	27
Mn/Sr	2.38	0.59	7.64	0.07	45.8	35	0.38	0.31	0.36	0.04	1.12	35
Kyrshabakty:												
$\delta^{13}C_{carb}$	-2.6	-2.2	4.0	-9.5	3.3	19						
$\delta^{18}O_{carb}$	-5.7	-5.0	2.5	-11.3	-2.3	15						
$^{87}Sr/^{86}Sr_{(m)}$	0.71043	0.70932	0.00182	0.70829	0.71371	19						
$^{87}Sr/^{86}Sr_{(i)}$	0.71036	0.70925	0.00182	0.70822	0.71364	19						
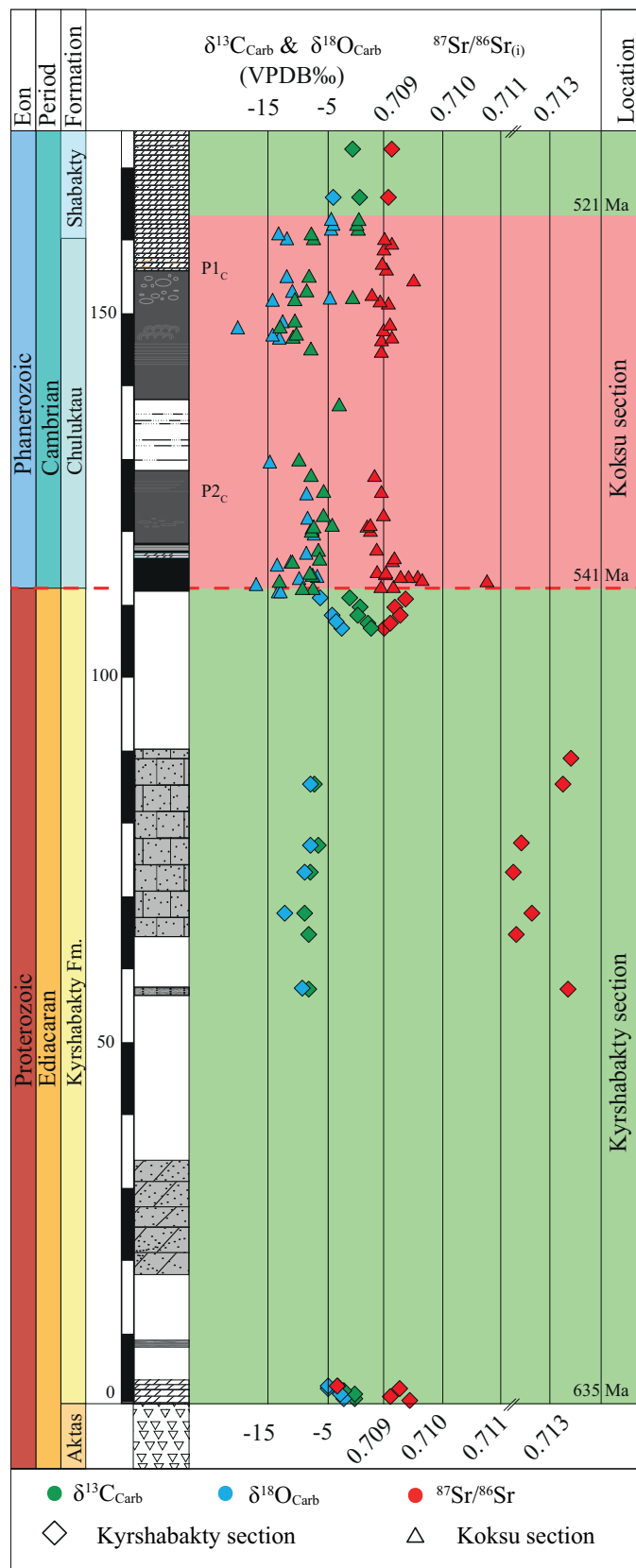
FIGURE 3.8: Compiled stable and radiogenic isotope record of two sections from Kazakhstan. Symbol sizes of $^{87}Sr/^{86}Sr$ data were adjusted in size to include leaching induced variation (see section 3 and 5.1 for details).

Any assessment of isotope values of marine precipitates has to consider change in the seawater composition from past to modern times. Based on Phanerozoic marine sedimentary rocks oxygen isotope reconstructions suggest an increase of $\delta^{18}O_{sw}$ values of the global seawater throughout the Phanerozoic up to modern times near 0 ‰ (VSMOW, Veizer, Ala, et al., 1999; Jaffrés, G. A. Shields, and Wallmann, 2007). Veizer and Prokoph (2015) proposed a past seawater δ^{18}Osw from -6.3 to -5.7 ‰ (VSMOW) during the early Cambrian epoch. Moreover, temperature (T) of the marine paleo environment during the Pc-C transition was likely higher (ca. 20-40^{circ}C) compared to present day, where T estimates are based on fluid inclusions in halite and on silicon isotopes in cherts (Meng et al., 2011; Robert and Chaussidon, 2006). Both, lighter oxygen isotope signatures of H_2O and elevated T, yield isotopically lighter precipitated carbonate compared to present day marine conditions (Kim and O'Neil, 1997; Friedman and O'Neil, 1977). The latter trend is documented by the average $\delta^{18}O_{carb}$ = -11.7 ± 3.8 ‰ of our measured samples (VPBD; Table 3.2). Although the uncertainties in the proposed past seawater oxygen isotope composition and apparent temperature are high, the $\delta^{18}O_{carb}$ range fits worthy within the above mentioned $\delta^{18}O_{sw}$ and T trend. Absolute values from either of them seem to be not reasonable to be presented for this paleo-environment due to potential overprinting even at a very low level throughout the whole Phanerozoic.

A further way to distinguish between primary seawater signatures and secondary overprint is to identify a co-variation in stable C-O isotopes. Lithification of marine sediments in the presence of mixed meteoric/marine fluids typically produces a linear covariance of $\delta^{18}O$ and $\delta^{13}C$ in bulk rocks, while post-depositional alteration through (high-T) fluid-rock interaction causes deviations from this linear trend (Knauth and Kennedy, 2009; Marshall, 1992). From Figure 3.7 it is evident that the carbonate fraction of the majority of our samples preserved a linear trend of $\delta^{18}O$ and $\delta^{13}C$ indicating partly interaction with meteoric fluids during sediment lithification, rather than post-depositional diagenetic alteration. However, four samples with unusual $\delta^{18}O$ values most likely experienced post-depositional alteration and are thus excluded from further interpretation (Figure 3.7). One additional sample shows a $\delta^{18}O$ value of -17.3 ‰ yet establishes the lower end of the $\delta^{13}C$ and $\delta^{18}O$ correlation. Although measured $\delta^{18}O$ values of this study are generally on the lower end of the global spectrum, they are in alignment with a negative trend of seawater $\delta^{18}O$ values during the late Neoproterozoic to early Cambrian (Brasier, G. Shields, et al., 1996; Gamper, 2014; Meert et al., 2011; Ohnemüller, 2014; Veizer, 1989). The ratio of meteoric/marine pore waters during sediment lithification can be evaluated using Mn-Sr and C-O isotope trends. Generally, fluid-rock interaction with meteoric water leads to higher Mn contents and lower Sr, $\delta^{13}C_{carb}$ and $\delta^{18}O_{carb}$ (Azmy et al., 2011; Jacobsen and Kaufman, 1999). In samples from the Koksu section, the Mn/Sr ratio is generally low (median = 0.6, Table 3.2), with no apparent co-variation with C-O isotopes (Figure 3.9), arguing for a low impact of meteoric fluids during

sediment lithification. One sample (KO 04) with Mn/Sr = 46, however, likely experienced alteration, and is thus excluded from interpretation on the following paleo environmental reconstruction. Isotope re-adjustment during lithification might also affect the Sr isotope composition. $^{87}Sr/^{86}Sr$ composition of interacting fluids depend on their Sr source, i.e., fluids circulating through continental felsic rocks result in radiogenic $^{87}Sr/^{86}Sr$, and through mafic rocks in less radiogenic $^{87}Sr/^{86}Sr$ (Brand et al., 2010). Continental weathering or dissolution of carbonates should result in similar $^{87}Sr/^{86}Sr$ fluid compositions. EMP spot analysis show high concentrations of Sr (ca. 0.3 wt% SrO) in the CFA minerals (Appendix Figure B.1, B.1). Alteration of the $^{87}Sr/^{86}Sr$ composition through low degrees of meteoric/marine pore waters during sediment lithification, as implied by C-O isotope systematics and more likely to affect the carbonate matrix, would be strongly rock buffered. To test the impact of the different phases that contribute to the Sr isotope signal, leaching experiments were conducted on two selected samples (KO 10 and KO 13) with different matrix (dolomite vs. calcite) and texture (phos-grainstone (KO 10) vs. phos-rudstone (KO 13), Appendix Figure B.1, B.1). The results reveal systematically higher $^{87}Sr/^{86}Sr$ values for weak acid-leachates (0.05 mol l^{-1} HNO$_3$) consistent with matrix dissolution. Variations among the different leachates and thus phases, however, were within our reproducibility of $\pm$ 100 ppm.

Alteration through either meteoric fluids or post-depositional (burial) fluids further changes REE compositions in abiogenic carbonates and phosphorites in respect to both bulk contents and patterns (Azmy et al., 2011; Emsbo et al., 2015). In the former case, minerals exhibit some REE enrichment and retain their mineral-specific REE$_N$ patterns, while post-depositional alteration causes anomalous REE patterns. In abiogenic phosphorites REE$_N$ patterns and ΣREE may show secular variation during the Phanerozoic periods (Emsbo et al., 2015). REE$_N$ in the Kazakh phosphorites resemble those of typical Cambrian phosphorites with minor REE$_N$ enrichment not exceeding values of about 10 (Figure 3.5, Emsbo et al., 2015; A. Ilyin, 1998; G. Shields and Stille, 2001). Combining these results with the lack of coherent Mn-Sr systematics and linear $\delta^{13}C$ and $\delta^{18}O$ correlation (Figure 3.9; Brand and Veizer, 1980; Jacobsen and Kaufman, 1999; Li et al., 2013), with the petrographic observations, we conclude that our suites have experienced minor fluid-rock interaction during sediment lithification at low meteoric/marine fluid ratios, altering the carbonate $\delta^{13}C$ and $\delta^{18}O$, however, otherwise preserving near-primary geochemical signatures and microstructures (Figure 3.5). $^{87}Sr/^{86}Sr$ values from the Kyrshabakty section are found to be pristine and were interpreted as result of enhanced continental weathering coupled with locally coinciding high sedimentation rates (Ohnemüller, 2014).
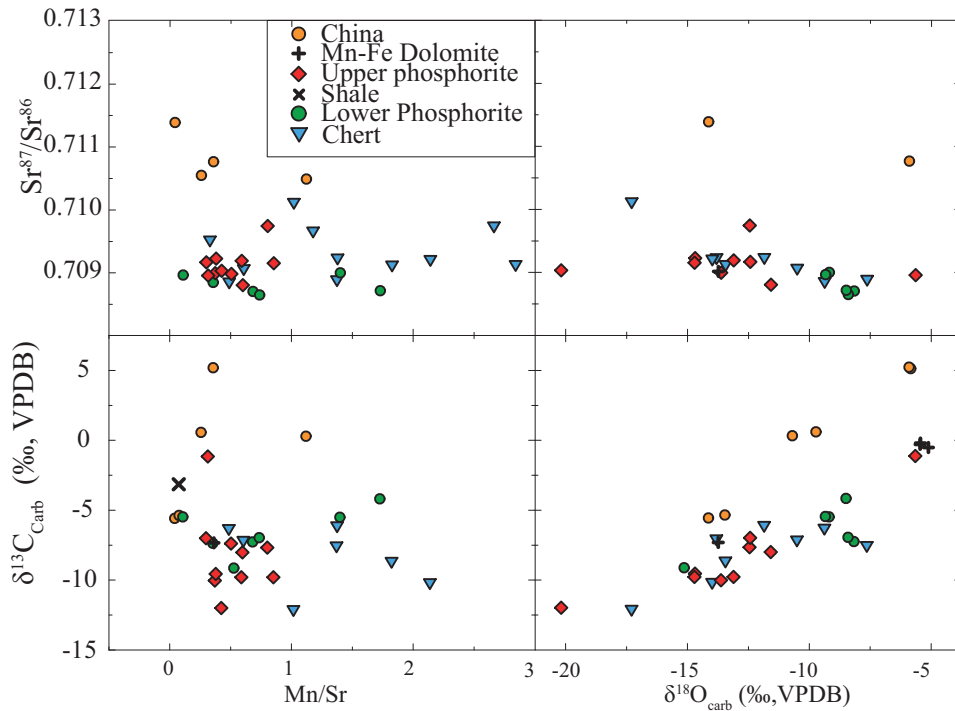
FIGURE 3.9: Scatter diagrams plotting elements that are prone to diagenetic alteration. Symbols as reported in Figure 3.2.

3.5.2 Stratigraphic correlation

The Lower Cambrian episode is marked by several globally correlated negative $\delta^{13}C_{carb}$ excursion with relative variations of up to $\pm$ 10 ‰ (Brasier, Corfield, et al., 1994; Derry et al., 1994; Gamper, 2014; Halverson, Wade, et al., 2010; Jiedong et al., 1999; Li et al., 2013; Ohnemüller, 2014; Zhu, Lu, et al., 2013). Oxygen isotope values generally follow a similar pattern with an overall trend towards strongly negative $\delta^{18}O_{carb}$ values during the Lower Cambrian of ca. -16 ‰ (Li et al., 2013).

The low $\delta^{13}C_{carb}$ and $\delta^{18}O_{carb}$ values from the Koksu carbonates (Kazakhstan, Figure 3.1) are consistent with the basal Cambrian negative carbon isotope excursion (BACE) right at the Pc-C boundary with global composite $\delta^{13}C$ of ca -10 ‰ (Figure 3.8, e.g., Shields-Zhou and Zhu (2013), and references therein). Two more negative excursions are recognized at the Koksu section, which are similar in magnitude as the global carbon isotope curves, however due to the number of negative excursions in the early Cambrian, pinpointing individual excursions seems unreasonable.

Stable isotope values at Koksu are slightly lower than those of the Cambrian phosphorites of the adjacent Kyrshabakty section. However, both Ediacaran and Cambrian samples from Kazakhstan, as well as some Cambrian Chinese samples, all deposited in a shallow water environment, plot on the same trend line, regardless of phosphorites or pure carbonates. Despite the possible influence by diagenetic alteration, the

slope of the overall regression line in Figure 3.7 shows that both Ediacaran and Cambrian samples plot on one line. This suggests that samples may still retain their near-primary C and O isotopes signatures and the stable isotope composition of the marine deposits depends rather on the depositional environment than on the time of deposition or type of sediment. The depositional environment for the highlighted data points in Figure 3.7 was a proximal shallow water setting opposed to the distinct scatter of the Ediacaran Chinese samples deposited in an intra-shelf basin setting (Zhu, J. Zhang, and Yang, 2007).

3.5.3 $^{87}Sr/^{86}Sr$ seawater evolution at the Pc-C transition

As the residence time of Sr in oceans exceeds ocean mixing time by far, $^{87}Sr/^{86}Sr$ is thought to be homogenous in a connected ocean (Veizer, 1989). Although $^{87}Sr/^{86}Sr$ values have predominantly been compiled from carbonate rocks, phosphate-rich deposits constitute a viable alternative and additional archive for past seawater $^{87}Sr/^{86}Sr$ reconstructions (McArthur et al., 1990). This is particularly important for the Pc-C transition, since phosphorites were widely deposited at this time.

$^{87}Sr/^{86}Sr$ values from the Chulaktau Formation at the Koksu section is framed by identical $^{87}Sr/^{86}Sr$ values of the adjacent Kyrshabakty section, completing the Lower Cambrian Sr isotope record for Kazakhstan (Figure 3.8). The global value of $^{87}Sr/^{86}Sr$ in seawater for the Neoproterozoic era is ca. 0.7065, followed by a rise to about 0.7085 in the Lower Cambrian period (Figure 3.10, Veizer, Ala, et al., 1999; Halverson, Wade, et al., 2010). The similarity of lower Cambrian $^{87}Sr/^{86}Sr$ values from Kazakhstan with the global evolution confirms Kazakhstan was connected to the global open ocean seawater evolution during that time. Right at the Pc-C transition, a distinct positive $^{87}Sr/^{86}Sr$ excursion is observed, which corresponds to negative $\delta^{13}C_{carb}$ and $\delta^{18}O_{carb}$ excursions (Figure 3.8). This positive $^{87}Sr/^{86}Sr$ excursion has also been observed in adjacent (micro-) continents Namibia, Siberia, Mongolia and China, with $^{87}Sr/^{86}Sr$ values as high as ca. $^{87}Sr/^{86}Sr = 0.711$ (Figure 3.10, Brasier, G. Shields, et al., 1996; Derry et al., 1994; Halverson, Wade, et al., 2010; Li et al., 2013; Nicholas, 1996; Ohnemüller, 2014; Sawaki, Tahata, et al., 2014; Sawaki, Ohno, Fukushi, et al., 2008). Another, however less pronounced, positive $^{87}Sr/^{86}Sr$ excursion occurs during the middle Ediacaran (Figure 3.10, Jiedong et al., 1999; W. Wang et al., 2002; Sawaki, Ohno, Tahata, et al., 2010; Ohnemüller, 2014).

At the investigated Chinese sections, distinctly high Sr isotope values are recorded (Figure 3.2). We assume these high values are derived from increased local weathering rates, coupled with enhanced accumulation rates in a semi-restricted shallow ocean basin and corresponding limited exchange with the open ocean seawater $^{87}Sr/^{86}Sr$ (Zhu, Lu, et al., 2013).

Li et al. (2013) argued from geochemical markers such as strongly negative $\delta^{18}O$ values that the high $^{87}Sr/^{86}Sr$ values, which were observed in phosphatic sediments

from South China, are the result of diagenetic alteration. However, Sawaki, Ohno, Fukushi, et al. (2008) and Sawaki, Tahata, et al. (2014) and Halverson, Wade, et al. (2010) reported similar positive $^{87}Sr/^{86}Sr$ excursions in marine platform carbonates from South China for the terminal Ediacaran period. High $^{87}Sr/^{86}Sr$ values at these sections were interpreted as near-primary values and attributed to the weathering-related increasing seawater $^{87}Sr/^{86}Sr$ during the Neoproterozoic. Our new data set from the Koksu section confirms that this positive Sr isotope excursion at the Pc-C transition is a reflection of the seawater isotope value and not a result of post-depositional alteration. Since these $^{87}Sr/^{86}Sr$ values are among the most extreme isotope excursions reported in Earth's history, a causal relationship with the Pc-C biogeochemical changes seems plausible.

Generally speaking, seawater $^{87}Sr/^{86}Sr$ is mainly controlled by hydrothermal activity, contributing juvenile $^{87}Sr/^{86}Sr$, and continental run-off, contributing radiogenic $^{87}Sr/^{86}Sr$ (e.g., Palmer and Edmond, 1989; Nebel and Stammeier, 2016). Throughout the Neoproterozoic, enhanced weathering rates and an associated increase in seawater $^{87}Sr/^{86}Sr$, concomitant with low $\delta^{13}C_{carb}$, have been linked to the continental break-up of Rodinia and global glaciations (Halverson, Hurtgen, et al., 2009; G. A. Shields, 2007). However, the extent observed at the Pc-C boundary with the profound, sharp increase in $^{87}Sr/^{86}Sr$ over a short time period of only a few million years, requires a more distinct mechanism. Richter, Rowley, and DePaolo (1992) modelled seawater $^{87}Sr/^{86}Sr$ in response to tectonic events that coincide with high erosion rates and thus changes in riverine influx. They found these events to cause short time $^{87}Sr/^{86}Sr$ seawater excursions that last for about 15-25 million years.

Given the relation between Sr isotopes in seawater and erosion rates, a sudden change in the continental weathering regime may be responsible for the extreme Sr isotope variations. The onset of more profound oxidative weathering of continental silicates as a result of higher atmospheric oxygen levels, combined with increased erosion rates in the aftermath of several Precambrian glaciation events (Kasemann et al., 2014), could have significantly contributed radiogenic $^{87}Sr/^{86}Sr$ into marginal shallow ocean basins. This scenario might have caused the sudden increase of $^{87}Sr/^{86}Sr$ at the Pc-C boundary, momentarily changing the balance between $^{87}Sr/^{86}Sr$ flux to the ocean vs. counterbalancing sources of non-radiogenic Sr (e.g., from mid-ocean ridge hydrothermal activity, Boger and Miller, 2004; Lyle et al., 1987; White and McKenzie, 1989). To explain the sudden increase and subsequent drop in Sr isotopes, we adopt the scenario of Sawaki, Ohno, Fukushi, et al. (2008), in which high $^{87}Sr/^{86}Sr$ of shallow ocean waters, introduced by enhanced weathering, was subsequently buffered by rift related mid-ocean ridge magmatism. Although diagenetic fluids that circulated through mafic rocks may also contribute low $^{87}Sr/^{86}Sr$ during diagenesis thereby causing a drop of $^{87}Sr/^{86}Sr$ in the local sediments, petrographic and geochemical preservation argue against this possibility (compare section 5.1). In that context, the sudden Sr isotope excursion may reflect the response of weathering to geodynamic
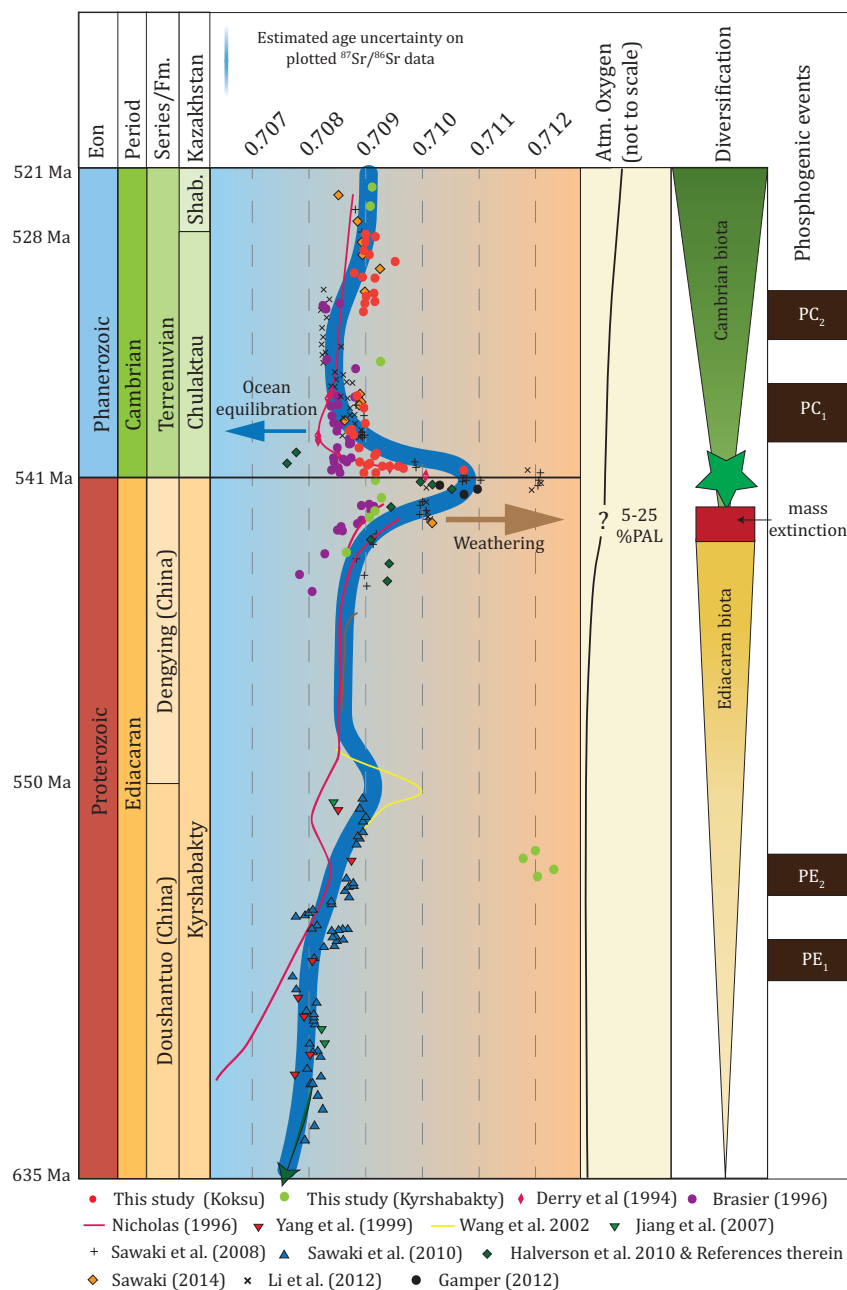
FIGURE 3.10: Compiled ^{87}Sr/^{86}Sr data covering the Pc-C boundary. Blue line represents suggested global seawater ^{87}Sr/^{86}Sr evolution including two positive excursions. Compiled data from: (This study, Derry et al., 1994; Brasier, G. Shields, et al., 1996; Nicholas, 1996; Jiedong et al., 1999; W. Wang et al., 2002; Jiang et al., 2007; Sawaki, Ohno, Fukushi, et al., 2008; Sawaki, Ohno, Tahata, et al., 2010; Halverson, Wade, et al., 2010; Li et al., 2013; Gamper, 2014; Ohnemüller, 2014; Sawaki, Tahata, et al., 2014). Stratigraphic correlation according to δ^{13}C chemostratigraphy. Note that the absolute ages are non-linear.

changes that are contemporaneous and thus probably associated with an increase in atmospheric and ocean oxygen levels.

The increase of oxygen in the oceans and the atmosphere during the Pc-C transition

has been discussed as a driving force of the Cambrian Explosion (Cloud, 1976; Runnegar, 1982; McMenamin, 1988; Canfield, Poulton, and Narbonne, 2007; Mills and Canfield, 2014; Gilbert, 2011). Accordingly, the Pc-C boundary forms a transition from a Neoproterozoic stratified ocean with oxygenated surface and anoxic bottom waters, to a Phanerozoic well mixed and oxygenated ocean (Canfield, Poulton, and Narbonne, 2007; Wille et al., 2008). To oxygenate the deeper oceans, increasing atmospheric oxygen levels, deep-water circulation or ecosystem engineering is required (Lenton, Boyle, et al., 2014). Anbar (2002) argue that progressive oxygenation increases the bioavailability of essential nutrients, a prerequisite of metazoan life. The decline of redox-sensitive elements and e.g., an associated increase in δ^{34}S value of dissolved sulfate in early Cambrian strata is also seen as evidence for a progressing ocean oxygenation (Canfield and Teske, 1996; Och et al., 2016).

At the Koksu section, the lack of redox-sensitive element enrichment, e.g. Ni, As, V and Co, which are more soluble under reducing conditions, and the negative Ce anomalies in the Cambrian shallow water sediments confirm the presence of elevated oxygen levels in shallow waters (Figure 3.4). The invention of animal burrowing in the early Cambrian, the so-called "Cambrian Substrate Revolution" or "Agronomic Revolution" (Bottjer, 2010) facilitates the decomposition or reworking of sediment-sealing microbial mats and thus oxygen transport into the deeper sediment. Intervals of such intensified bioturbation likely caused the variable Ce anomalies across the Koksu profile (Figure 3.4). In this scenario, the mixed and well-oxygenated sediment then facilitates oxygenation of organic carbon, contributing to generally low δ^{13}C. In summary, it is argued that the combined stable and radiogenic isotope and element data at the Pc-C transition mark a complex interplay of connected processes that either reflect greater geodynamic processes (Sr) or direct responses of the atmosphere (redox-sensitive elements) and the environment (C-O).

3.5.4 The occurrence of phosphorite deposits

The contemporaneous occurrence of giant phosphorite deposits and the Cambrian Explosion is linked to an increase in both Ca and P in shallow ocean waters. As a consequence of elevated oxygen levels and generally increased weathering rates, the breakdown of terrigenous material enhanced the nutrient supply to shallow ocean waters. For the early Cambrian a threefold rise of available Ca2+ in the seawater is reported (Berner, 2004; Brennan, Lowenstein, and Horita, 2004). This high nutrient transport into shallow waters promotes increased primary production, which in turn enhances phosphate cycling in shallow waters. Subsequent burial and decomposition of organic matter from primary producers at the water-sediment interface liberates organically bound phosphate and concentrates phosphate in the pore water. Experimental studies show that phosphate rapidly precipitates in the presence of Ca^{2+} under a wide range of conditions, both with or without microbial mediation (Combes and

Rey, 2010; Crosby and Bailey, 2012; Omelon, Ariganello, et al., 2013). This change in seawater/pore water chemistry leading to local supersaturation likely facilitated the formation of the precursor phase hydroxy- (fluor-) apatite and the subsequent transformation to CFA, which subsequently form phosphorites. Dissolved phosphate ions (PO_4^{3-}) are strongly linked to a complex redox-chemistry and often also coupled with biologic activity (Föllmi, 1996; Glenn et al., 1994; Omelon and Grynpas, 2008). It is thus likely that enhanced phosphorite deposition is strongly coupled to elevated oxygen levels in the oceans and thus a direct response to the oxygenation of the atmosphere. In conjunction with the positive excursion in radiogenic Sr isotopes, it seems plausible that Ca and P availability was enhanced through oxidation. The inherent bloom of Cambrian biota and agronomic revolution facilitated an efficient mixture of the water column through biological pumping (Butterfield, 2009; Meyer, Ridgwell, and Payne, 2016). This caused thereafter a rapid decline in Sr isotope signature. Accordingly, enhanced phosphorite deposits are strongly coupled to elevated oxygen levels in the oceans and thus a direct response to prior oxygenation of the atmosphere.

3.6　Summary and Conclusions

The complex interaction between primary production of marine biota, global ocean chemistry, weathering rates and nutrient availability led to a significant increase of biodiversity and the concomitant occurrence of giant phosphorite deposits throughout the early Cambrian. The presented comprehensive geochemical and isotope data increases our understanding on the significant change of paleo-environmental parameters during Pc-C transition:

The microstructure of the phosphorites clearly shows sedimentary textures characteristic for deposition in a medium to high energy shallow water environment with a pristine internal structure. Besides these microstructural features, the mineralogical/chemical composition and stable isotope distribution of C and O of the carbonate are in alignment with precipitates typically formed in shallow past marine environments, thus nearly primary material can be reasonably assumed with limited post depositional and diageneses overprint. Paleo-Kazakhstan exhibits the same negative $\delta^{13}C$ excursion (BACE) and some negative excursions thereafter as globally recognized in early Cambrian stratigraphy. The trace element and REE distribution in the carbonate and phosphate phases indicates near-pristine material with low meteoric/marine pore waters interactions during sediment lithification. Accordingly the herein investigated phosphorites at the Koksu section in Kazakhstan can be classified from microstructure and composition as a near-primary sedimentary rocks, and are suggested to be a valuable seawater archive.

^{87}Sr/^{86}Sr values at Koksu exhibit a trend towards more radiogenic values at the Pc-C boundary, sourced from an episode of rapidly increased continental (silicate) weathering. The general ^{87}Sr/^{86}Sr at Koksu aligns with the global seawater ^{87}Sr/^{86}Sr evolution. A similar positive excursion at the Pc-C boundary can be observed at several paleo-microcontinents, indicating this episode of increased continental silicate weathering was not only a local, but a global event.

This episode is characterized by a combination of already increased continental weathering rates (physical and chemical) due to elevated atmospheric oxygen levels. As a consequence, an increased influx of continental material and corresponding nutrients drive primary production in shallow waters that permanently manifests in the nutrient cycles. This in turn gives way to an increased and rapid oxygen production, thus entering a new positive feedback loop, ultimately driving the Cambrian Explosion. The present new and compiled data set support the central role of continental weathering and erosion rates, possibly linked to atmospheric oxygenation occurring around the Pc-C transition on the Cambrian Explosion.

Acknowledgements

References

Alexeiev, D. V., H. E. Cook, V. M. Buvtyshkin, and L. Y. Golub (2009). "Structural evolution of the Ural–Tian Shan junction: A view from Karatau ridge, South Kazakhstan". In: *Comptes Rendus Geoscience* 341. DOI: 10.1016/j.crte.2008.12.004.

Altschuler, Z. S. (1980). "The Geochemistry of Trace Elements in Marine Phosphorites. Part I. Characteristic Abundances and Enrichment". In: *Marine Phosphorites—Geochemistry, Occurrence, Genesis.* Ed. by Y. K. Bentor. Vol. 29. SEPM (Society for Sedimentary Geology), pp. 19–30. DOI: 10.2110/pec.80.29.0019.

Anbar, A. D. (2002). "Proterozoic Ocean Chemistry and Evolution: A Bioinorganic Bridge?" In: *Science* 297. DOI: 10.1126/science.1069651.

Azmy, K., U. Brand, P. Sylvester, S. A. Gleeson, A. Logan, and M. A. Bitner (2011). "Biogenic and abiogenic low-Mg calcite (bLMC and aLMC): Evaluation of seawater-REE composition, water masses and carbonate diagenesis". In: *Chemical Geology* 280. DOI: 10.1016/j.chemgeo.2010.11.007.

Bailey, J. V., F. A. Corsetti, S. E. Greene, C. H. Crosby, P. Liu, and V. J. Orphan (2013). "Filamentous sulfur bacteria preserved in modern and ancient phosphatic sediments: implications for the role of oxygen and bacteria in phosphogenesis". In: *Geobiology* 11. DOI: 10.1111/gbi.12046.

Barfod, G. H., F. Albarède, A. H. Knoll, S. Xiao, P. Télouk, R. Frei, and J. Baker (2002). "New Lu-Hf and Pb-Pb age constraints on the earliest animal fossils". In: *Earth and Planetary Science Letters* 201. DOI: 10.1016/S0012-821X(02)00687-8.

Bengtson, S. and Y. Zhao (1992). "Predatorial Borings in Late Precambrian Mineralized Exoskeletons". In: *Science* 257. DOI: 10.1126/science.257.5068.367.

Berner, R. A. (2004). "A model for calcium, magnesium and sulfate in seawater over Phanerozoic time". In: *American Journal of Science* 304. DOI: 10.2475/ajs.304.5.438.

Boger, S. D. and J. M. Miller (2004). "Terminal suturing of Gondwana and the onset of the Ross–Delamerian Orogeny: the cause and effect of an Early Cambrian reconfiguration of plate motions". In: *Earth and Planetary Science Letters* 219. DOI: 10.1016/S0012-821X(03)00692-7.

Bottjer, D. J. (2010). "The cambrian substrate revolution and early evolution of the phyla". In: *Journal of Earth Science* 21. DOI: 10.1007/s12583-010-0160-7.

Brand, U. and J. Veizer (1980). "Chemical Diagenesis of a Multicomponent Carbonate System–1: Trace Elements". In: *SEPM Journal of Sedimentary Research* Vol. 50. DOI: 10.1306/212F7BB7-2B24-11D7-8648000102C1865D.

Brasier, M. D. (1982). "Sea-level changes, facies changes and the late Precambrian—Early cambrian evolutionary explosion". In: *Precambrian Research* 17. DOI: 10.1016/0301-9268(82)90050-X.

Brasier, M. D., R. M. Corfield, L. A. Derry, A. Y. Rozanov, and A. Y. Zhuravlev (1994). "Multiple δ13C excursions spanning the Cambrian explosion to the Botomian crisis in Siberia". In: *Geology* 22. DOI: 10.1130/0091-7613(1994)022<0455:MCESTC>2.3.CO;2.

Brasier, M. D., G. Shields, V. N. Kuleshov, and E. A. Zhegallo (1996). "Integrated chemo- and biostratigraphic calibration of early animal evolution: Neoproterozoic–early Cambrian of southwest Mongolia". In: *Geological Magazine* 133. DOI: 10.1017/S0016756800007603.

Brennan, S. T., T. K. Lowenstein, and J. Horita (2004). "Seawater chemistry and the advent of biocalcification". In: *Geology* 32. DOI: 10.1130/G20251.1.

Butterfield, N. J. (2009). "Oxygen, animals and oceanic ventilation: an alternative view." In: *Geobiology* 7. DOI: 10.1111/j.1472-4669.2009.00188.x.

Canfield, D. E., S. W. Poulton, and G. M. Narbonne (2007). "Late-Neoproterozoic deep-ocean oxygenation and the rise of animal life." In: *Science (New York, N.Y.)* 315. DOI: 10.1126/science.1135013.

Canfield, D. E. and A. Teske (1996). "Late Proterozoic rise in atmospheric oxygen concentration inferred from phylogenetic and sulphur-isotope studies". In: *Nature* 382. DOI: 10.1038/382127a0.

Chen, X., H. Ling, D. Vance, G. Shields-Zhou, M. Zhu, S. W. Poulton, L. M. Och, S. Jiang, D. Li, L. Cremonese, and C. Archer (2015). "Rise to modern levels of ocean oxygenation coincided with the Cambrian radiation of animals". In: *Nature Communications* 6. DOI: 10.1038/ncomms8142.

Cloud, P. (1976). "Beginnings of biospheric evolution and their biogeochemical consequences". In: *Paleobiology* 2. DOI: 10.1017/S009483730000498X.

Combes, C. and C. Rey (2010). "Amorphous calcium phosphates: Synthesis, properties and uses in biomaterials". In: *Acta Biomaterialia* 6. DOI: 10.1016/j.actbio.2010.02.017.

Cook, P. J. (1992). "Phosphogenesis around the Proterozoic-Phanerozoic transition". In: *Journal of the Geological Society* 149. DOI: 10.1144/gsjgs.149.4.0615.

Cook, P. J. and J. H. Shergold (1986). "Phosphate Deposits of the World. Volume 1. Proterozoic and Cambrian Phosphorites". In: *Geological Magazine.* Ed. by P. J. Cook and J. H. Shergold. Vol. 124. Cambridge: Cambridge University Press, p. 487. DOI: 10.1017/S0016756800017106.

– (2005). "Genesis of phosphorite deposits". In: *Phosphate Deposits of the World: Volume 1: Proterozoic and Cambrian Phosphorites.* Ed. by P. J. Cook and J. H. Shergold. Cambridge: Cambridge University Press, pp. 135–156.

Crosby, C. H. and J. V. Bailey (2012). "The role of microbes in the formation of modern and ancient phosphatic mineral deposits". English. In: *Frontiers in Microbiology* 3. DOI: 10.3389/fmicb.2012.00241.

Dalziel, I. W. D. (2014). "Cambrian transgression and radiation linked to an Iapetus-Pacific oceanic connection?" In: *Geology* 42. DOI: 10.1130/G35886.1.

Delaney, M. L. (1998). "Phosphorus accumulation in marine sediments and the oceanic phosphorus cycle". In: *Global Biogeochemical Cycles* 12. DOI: 10.1029/98GB02263.

Deniel, C. and C. Pin (2001). "Single-stage method for the simultaneous isolation of lead and strontium from silicate samples for isotopic measurements". In: *Analytica Chimica Acta* 426. DOI: 10.1016/S0003-2670(00)01185-5.

Derry, L. A., M. D. Brasier, R. Corfield, A. Y. Rozanov, and A. Zhuravlev (1994). "Sr and C isotopes in Lower Cambrian carbonates from the Siberian craton: A paleoenvironmental record during the 'Cambrian explosion'". In: *Earth and Planetary Science Letters* 128. DOI: 10.1016/0012-821X(94)90178-3.

Dietzel, M., F. Schön, J. Heinrichs, A. P. Deditius, and A. Leis (2016). "Tracing formation and durability of calcite in a Punic–Roman cistern mortar (Pantelleria Island, Italy)". In: *Isotopes in Environmental and Health Studies* 52. DOI: 10.1080/10256016.2015.1016430.

Dzik, J. (2003). "Early Cambrian lobopodian sclerites and associated fossils from Kazakhstan". In: *Palaeontology* 46. DOI: 10.1111/1475-4983.00289.

Eganov, E. A., K. Y. Sovetov, and A. L. Yanshin (1986). "Proterozoic and Cambrian phosphorite deposits: Karatau, southern Kazakhstan, USSR". In: *Phosphate Deposits of the World.* Ed. by P. J. Cook and J. H. Shergold. Vol. 1. Cambridge University Press, pp. 175–189.

Elderfield, H. (1986). "Strontium isotope stratigraphy". In: *Palaeogeography, Palaeoclimatology, Palaeoecology* 57. DOI: 10.1016/0031-0182(86)90007-6.

Emsbo, P., P. I. McLaughlin, G. N. Breit, E. A. du Bray, and A. E. Koenig (2015). "Rare earth elements in sedimentary phosphate deposits: Solution to the global REE crisis?" In: *Gondwana Research* 27. DOI: 10.1016/j.gr.2014.10.008.

Filippelli, G. M. (2011). "Phosphate rock formation and marine phosphorus geochemistry: The deep time perspective". In: *Chemosphere* 84. DOI: 10.1016/j.chemosphere.2011.02.019.

Föllmi, K. (1996). "The phosphorus cycle, phosphogenesis and marine phosphate-rich deposits". In: *Earth-Science Reviews* 40. DOI: 10.1016/0012-8252(95)00049-6.

Fox, D. (2016). "What sparked the Cambrian explosion?" In: *Nature* 530. DOI: 10.1038/530268a.

Friedman, I. and J. R. O'Neil (1977). "Compilation of stable isotope fractionation factors of geochemical interest". In: *Data of Geochemistry.* U.S. Geological Survey.

Gamper, A. (2014). "Global trends in nutrient dynamics during the Ediacaran-Cambrian period as revealed by nitrogen and carbon isotope trends". Dissertation. Freien Universität Berlin.

Gamper, A., U. Struck, F. Ohnemueller, C. Heubeck, and S. Hohl (2015). "Chemo- and biostratigraphy of the Gaojiashan section (northern Yangtze platform, South China): a new Pc-C boundary section". In: *Fossil Record* 18. DOI: 10.5194/fr-18-105-2015.

Giezen, M. and T. M. Lenton (2012). "The Rise of Oxygen and Complex Life". In: *Journal of Eukaryotic Microbiology* 59. DOI: `10.1111/j.1550-7408.2011.00605.x`.

Gilbert, D. L. (2011). "Evolutionary Aspects of Atmospheric Oxygen and Organisms". In: *Comprehensive Physiology.* Hoboken, NJ, USA: John Wiley & Sons, Inc. DOI: `10.1002/cphy.cp040246`.

Glenn, C. R., K. B. Föllmi, S. R. Riggs, G. N. Baturin, K. A. Grimm, J. Trappe, A. M. Abed, C. Galli-Olivier, R. E. Garrison, A. V. Ilyin, C. Jehl, V. Rohrlich, R. M. Sadaqah, M. Schidlowski, R. E. Sheldon, and H. Seigmund (1994). "Phosphorus and phosphorites: sedimentology and environments of formation". In: *Eclogae Geologicae Helvetiae* 87.

Goldring, R. and S. Jensen (1996). "Trace fossils and biofabrics at the Precambrian–Cambrian boundary interval in western Mongolia". In: *Geological Magazine* 133. DOI: `10.1017/S0016756800007573`.

Guo, Q., G. A. Shields, C. Liu, H. Strauss, M. Zhu, D. Pi, T. Goldberg, and X. Yang (2007). "Trace element chemostratigraphy of two Ediacaran–Cambrian successions in South China: Implications for organosedimentary metal enrichment and silicification in the Early Cambrian". In: *Palaeogeography, Palaeoclimatology, Palaeoecology* 254. DOI: `10.1016/j.palaeo.2007.03.016`.

Halverson, G. P., M. Hurtgen, S. M. Porter, and A. S. Collins (2009). "Neoproterozoic-Cambrian Biogeochemical Evolution". In: *Neoproterozoic-Cambrian Tectonics, Global Change And Evolution: A Focus On South Western Gondwana.* Ed. by C. Gaucher, A. N. Sial, H. E. Frimme, and G. P. Halverson. Vol. 16. Developments in Precambrian Geology. Chap. 10, pp. 351–365. DOI: `10.1016/S0166-2635(09)01625-9`.

Halverson, G. P., B. P. Wade, M. T. Hurtgen, and K. M. Barovich (2010). "Neoproterozoic chemostratigraphy". In: *Precambrian Research* 182. DOI: `10.1016/j.precamres.2010.04.007`.

Hans, U. (2013). "High-precision strontium isotope measurements on meteorites: implications for the origin and timing of volatile depletion in the inner solar system". Dissertation. ETH Zürich.

Heubeck, C., G. Ergaliev, and S. Evseev (2013). "Large-Scale Seismogenic Deformation of A Carbonate Platform Straddling the Precambrian-Cambrian Boundary, Karatau Range, Kazakhstan". In: *Journal of Sedimentary Research* 83. DOI: `10.2110/jsr.2013.76`.

Holmer, L. E., L. E. Popov, S. P. Koneva, and R. Jia-Yu (1997). "Early Cambrian Lingulellotreta (Lingulata, Brachiopoda) from South Kazakhstan (Malyi Karatau Range) and South China (Eastern Yunnan)". In: *Journal of Paleontology* 71. DOI: `10.1017/S0022336000040063`.

Ilyin, A. V. (2004). "The Khubsugul Phosphate-Bearing Basin: New Data and Concepts". In: *Lithology and Mineral Resources* 39. DOI: `10.1023/B:LIMI.0000040735.76025.80`.

Ilyin, A. (1998). "Rare-earth geochemistry of 'old' phosphorites and probability of syngenetic precipitation and accumulation of phosphate 1". In: *Chemical Geology* 144. DOI: `10.1016/S0009-2541(97)00134-4`.

Jacobsen, S. B. and A. J. Kaufman (1999). "The Sr, C and O isotopic evolution of Neoproterozoic seawater". In: *Chemical Geology* 161. DOI: `10.1016/S0009-2541(99)00080-7`.

Jaffrés, J. B., G. A. Shields, and K. Wallmann (2007). "The oxygen isotope evolution of seawater: A critical review of a long-standing controversy and an improved geological water cycle model for the past 3.4 billion years". In: *Earth-Science Reviews* 83. DOI: `10.1016/j.earscirev.2007.04.002`.

Jiang, G., A. J. Kaufman, N. Christie-Blick, S. Zhang, and H. Wu (2007). "Carbon isotope variability across the Ediacaran Yangtze platform in South China: Implications for a large surface-to-deep ocean δ13C gradient". In: *Earth and Planetary Science Letters* 261. DOI: `10.1016/j.epsl.2007.07.009`.

Jiedong, Y., S. Weiguo, W. Zongzhe, X. Yaosong, and T. Xiancong (1999). "Variations in Sr and C isotopes and Ce anomalies in successions from China: evidence for the oxygenation of Neoproterozoic seawater?" In: *Precambrian Research* 93. DOI: `10.1016/S0301-9268(98)00092-8`.

Kasemann, S. A., P. A. Pogge von Strandmann, A. R. Prave, A. E. Fallick, T. Elliott, and K. Hoffmann (2014). "Continental weathering following a Cryogenian glaciation: Evidence from calcium and magnesium isotopes". In: *Earth and Planetary Science Letters* 396. DOI: `10.1016/j.epsl.2014.03.048`.

Keto, L. S. and S. B. Jacobsen (1987). "Nd and Sr isotopic variations of Early Paleozoic oceans". In: *Earth and Planetary Science Letters* 84. DOI: `10.1016/0012-821X(87)90173-7`.

Kim, S.-T. and J. R. O'Neil (1997). "Equilibrium and nonequilibrium oxygen isotope effects in synthetic carbonates". In: *Geochimica et Cosmochimica Acta* 61. DOI: `10.1016/S0016-7037(97)00169-5`.

Knauth, L. P. and M. J. Kennedy (2009). "The late Precambrian greening of the Earth". In: *Nature* 460. DOI: `10.1038/nature08213`.

Komiya, T., A. Suga, T. Ohno, J. Han, J. Guo, S. Yamamoto, T. Hirata, and Y. Li (2008). "Ca isotopic compositions of dolomite, phosphorite and the oldest animal embryo fossils from the Neoproterozoic in Weng'an, South China". In: *Gondwana Research* 14. DOI: `10.1016/j.gr.2007.10.004`.

Laflamme, M., S. A. Darroch, S. M. Tweedt, K. J. Peterson, and D. H. Erwin (2013). "The end of the Ediacara biota: Extinction, biotic replacement, or Cheshire Cat?" In: *Gondwana Research* 23. DOI: `10.1016/j.gr.2012.11.004`.

Landing, E. (1994). "Precambrian-Cambrian boundary global stratotype ratified and a new perspective of Cambrian time". In: *Geology* 22. DOI: `10.1130/0091-7613(1994)022<0179:PCBGSR>2.3.CO;2`.

Lenton, T. M., R. a. Boyle, S. W. Poulton, G. a. Shields-Zhou, and N. J. Butterfield (2014). "Co-evolution of eukaryotes and ocean oxygenation in the Neoproterozoic era". In: *Nature Geoscience* 7. DOI: 10.1038/ngeo2108.

Lenton, T. M. and A. J. Watson (2004). "Biotic enhancement of weathering, atmospheric oxygen and carbon dioxide in the Neoproterozoic". In: *Geophysical Research Letters* 31. DOI: 10.1029/2003GL018802.

Levashova, N. M., J. G. Meert, A. S. Gibsher, W. C. Grice, and M. L. Bazhenov (2011). "The origin of microcontinents in the Central Asian Orogenic Belt: Constraints from paleomagnetism and geochronology". In: *Precambrian Research* 185. DOI: 10.1016/j.precamres.2010.12.001.

Li, D., H. F. Ling, G. A. Shields-Zhou, X. Chen, L. Cremonese, L. Och, M. Thirlwall, and C. J. Manning (2013). "Carbon and strontium isotope evolution of seawater across the Ediacaran–Cambrian transition: Evidence from the Xiaotan section, NE Yunnan, South China". In: *Precambrian Research* 225. DOI: 10.1016/j.precamres.2012.01.002.

Lyle, M., M. Leinen, R. M. Owen, and D. K. Rea (1987). "Late Tertiary history of hydrothermal deposition at the East Pacific Rise, 19°S: Correlation to volcano-tectonic events". In: *Geophysical Research Letters* 14. DOI: 10.1029/GL014i006p00595.

Marshall, J. D. (1992). "Climatic and oceanographic isotopic signals from the carbonate rock record and their preservation". In: *Geological Magazine* 129. DOI: 10.1017/S0016756800008244.

Maruyama, S., Y. Sawaki, T. Ebisuzaki, M. Ikoma, S. Omori, and T. Komabayashi (2014). "Initiation of leaking Earth: An ultimate trigger of the Cambrian explosion". In: *Gondwana Research* 25. DOI: 10.1016/j.gr.2013.03.012.

McArthur, J., A. Sahami, M. Thirlwall, P. Hamilton, and A. Osborn (1990). "Dating phosphogenesis with strontium isotopes". In: *Geochimica et Cosmochimica Acta* 54. DOI: 10.1016/0016-7037(90)90159-I.

McKerrow, W. S., C. R. Scotese, and M. D. Brasier (1992). "Early Cambrian continental reconstructions". In: *Journal of the Geological Society* 149. DOI: 10.1144/gsjgs.149.4.0599.

McLennan, S. M. (2001). "Relationships between the trace element composition of sedimentary rocks and upper continental crust". In: *Geochemistry, Geophysics, Geosystems* 2. DOI: 10.1029/2000GC000109.

McMenamin, M. A. (1988). "Paleoecological feedback and the Vendian-Cambrian transition". In: *Trends in Ecology & Evolution* 3. DOI: 10.1016/0169-5347(88)90008-0.

Meert, J. G., A. S. Gibsher, N. M. Levashova, W. C. Grice, G. D. Kamenov, and A. B. Ryabinin (2011). "Glaciation and ˜770Ma Ediacara (?) Fossils from the Lesser Karatau Microcontinent, Kazakhstan". In: *Gondwana Research* 19. DOI: 10.1016/j.gr.2010.11.008.

Meng, F., P. Ni, J. D. Schiffbauer, X. Yuan, C. Zhou, Y. Wang, and M. Xia (2011). "Ediacaran seawater temperature: Evidence from inclusions of Sinian halite". In: *Precambrian Research* 184. DOI: 10.1016/j.precamres.2010.10.004.

Meyer, K. M., A. Ridgwell, and J. L. Payne (2016). "The influence of the biological pump on ocean chemistry: Implications for long-term trends in marine redox chemistry, the global carbon cycle, and marine animal ecosystems". In: *Geobiology* 14. DOI: 10.1111/gbi.12176.

Mills, D. B. and D. E. Canfield (2014). "Oxygen and animal evolution: did a rise of atmospheric oxygen "trigger" the origin of animals?" In: *BioEssays : news and reviews in molecular, cellular and developmental biology* 36. DOI: 10.1002/bies.201400101.

Morris, S. C. (1987). "Cambrian enigmas". In: *Geology Today.*

– (1989). "Burgess Shale Faunas and the Cambrian Explosion". In: *Science* 246. DOI: 10.1126/science.246.4928.339.

Na, L. and W. Kiessling (2015). "Diversity partitioning during the Cambrian radiation". In: *Proceedings of the National Academy of Sciences* 112. DOI: 10.1073/pnas.1424985112.

Nebel, O. and J. A. Stammeier (2016). "Strontium Isotopes". In: *Encyclopedia of Geochemistry: A Comprehensive Reference Source on the Chemistry of the Earth.* Ed. by W. M. White. Springer International Publishing. DOI: 10.1007/978-3-319-39193-9_137-1.

Nicholas, C. J. (1996). "The Sr isotopic evolution of the oceans during the 'Cambrian Explosion'". In: *Journal of the Geological Society* 153. DOI: 10.1144/gsjgs.153.2.0243.

Och, L. M., L. Cremonese, G. A. Shields-Zhou, S. W. Poulton, U. Struck, H. Ling, D. Li, X. Chen, C. Manning, M. Thirlwall, H. Strauss, and M. Zhu (2016). "Palaeoceanographic controls on spatial redox distribution over the Yangtze Platform during the Ediacaran-Cambrian transition". In: *Sedimentology* 63. Ed. by I. Fairchild. DOI: 10.1111/sed.12220.

Ohnemüller, F. (2014). "Reconstruction of Ediacaran to early Cambrian Ocean pH and weathering conditions". Doctoral dissertation. Universität Bremen. DOI: [http://]http://nbn-resolving.de/urn:nbn:de:gbv:46-00103948-13.

Omelon, S. J., M. Ariganello, E. Bonucci, M. Grynpas, and A. Nanci (2013). "A Review of Phosphate Mineral Nucleation in Biology and Geobiology". In: *Calcified Tissue International* 93. DOI: 10.1007/s00223-013-9784-9.

Omelon, S. J. and M. D. Grynpas (2008). "Relationships between Polyphosphate Chemistry, Biochemistry and Apatite Biomineralization". In: *Chemical Reviews* 108. DOI: 10.1021/cr0782527.

Palmer, M. and J. Edmond (1989). "The strontium isotope budget of the modern ocean". In: *Earth and Planetary Science Letters* 92. DOI: 10.1016/0012-821X(89)90017-4.

Pin, C. and C. Bassin (1992). "Evaluation of a strontium-specific extraction chromatographic method for isotopic analysis in geological materials". In: *Analytica Chimica Acta* 269. DOI: 10.1016/0003-2670(92)85409-Y.

Popov, L. E., M. G. Bassett, V. G. Zhemchuzhnikov, L. E. Holmer, and I. a. Klishevich (2009). "Gondwanan faunal signatures from Early Palaeozoic terranes of Kazakhstan and Central Asia: evidence and tectonic implications". In: *Geological Society, London, Special Publications* 325. DOI: 10.1144/SP325.3.

Richter, F. M., D. B. Rowley, and D. J. DePaolo (1992). "Sr isotope evolution of seawater: the role of tectonics". In: *Earth and Planetary Science Letters* 109. DOI: 10.1016/0012-821X(92)90070-C.

Robert, F. and M. Chaussidon (2006). "A palaeotemperature curve for the Precambrian oceans based on silicon isotopes in cherts". In: *Nature* 443. DOI: 10.1038/nature05239.

Rothwell, R. G. (1989). "Micronodules (Fe-Mn Oxides and Hydroxides)". In: *Minerals and Mineraloids in Marine Sediments.* Dordrecht: Springer Netherlands, pp. 151–155. DOI: 10.1007/978-94-009-1133-8_16.

Runnegar, B. (1982). "The Cambrian explosion: Animals or fossils?" In: *Journal of the Geological Society of Australia* 29. DOI: 10.1080/00167618208729222.

Saltzman, M. R. (2005). "Phosphorus, nitrogen, and the redox evolution of the Paleozoic oceans". In: *Geology* 33. DOI: 10.1130/G21535.1.

Sawaki, Y., T. Ohno, Y. Fukushi, T. Komiya, T. Ishikawa, T. Hirata, and S. Maruyama (2008). "Sr isotope excursion across the Precambrian–Cambrian boundary in the Three Gorges area, South China". In: *Gondwana Research* 14. DOI: 10.1016/j.gr.2007.11.002.

Sawaki, Y., T. Ohno, M. Tahata, T. Komiya, T. Hirata, S. Maruyama, B. F. Windley, J. Han, D. Shu, and Y. Li (2010). "The Ediacaran radiogenic Sr isotope excursion in the Doushantuo Formation in the Three Gorges area, South China". In: *Precambrian Research* 176. DOI: 10.1016/j.precamres.2009.10.006.

Sawaki, Y., M. Tahata, T. Ohno, T. Komiya, T. Hirata, S. Maruyama, J. Han, and D. Shu (2014). "The anomalous Ca cycle in the Ediacaran ocean: Evidence from Ca isotopes preserved in carbonates in the Three Gorges area, South China". In: *Gondwana Research* 25. DOI: 10.1016/j.gr.2013.03.008.

Schulz, H. N. and H. D. Schulz (2005). "Large sulfur bacteria and the formation of phosphorite." In: *Science (New York, N.Y.)* 307. DOI: 10.1126/science.1103096.

Shen, Y., M. Schidlowski, and X. Chu (2000). "Biogeochemical approach to understanding phosphogenic events of the terminal Proterozoic to Cambrian". In: *Palaeogeography, Palaeoclimatology, Palaeoecology* 158. DOI: 10.1016/S0031-0182(00)00033-X.

Shields, G. A. (2007). "A normalised seawater strontium isotope curve: possible implications for Neoproterozoic-Cambrian weathering rates and the further oxygenation of the Earth". In: *eEarth* 2. DOI: 10.5194/ee-2-35-2007.

Shields, G. and P. Stille (2001). "Diagenetic constraints on the use of cerium anomalies as palaeoseawater redox proxies: an isotopic and REE study of Cambrian phosphorites". In: *Chemical Geology* 175. DOI: 10.1016/S0009-2541(00)00362-4.

Shields, G., P. Stille, and M. D. Brasier (1996). "Isotopic records across two phosphorite giant episodes compared: the Precambrian-Cambrian and the late Cretaceous-Recent". In: *Marine Authigenesis: From Global to Microbial.* Ed. by C. Glenn, L. Prevot-Lucas, and J. Lucas. Vol. 66, pp. 103–115.

Shields-Zhou, G. and M. Zhu (2013). "Biogeochemical changes across the Ediacaran–Cambrian transition in South China". In: *Precambrian Research* 225. DOI: 10.1016/j.precamres.2012.10.011.

Smith, M. P. and D. T. Harper (2013). "Causes of the Cambrian Explosion". In: *Science* 341. DOI: 10.1126/science.1239450.

Sperling, E. A., C. J. Wolock, A. S. Morgan, B. C. Gill, M. Kunzmann, G. P. Halverson, F. Macdonald, A. H. Knoll, and D. T. Johnston (2015). "Statistical analysis of iron geochemical data suggests limited late Proterozoic oxygenation". In: *Nature* 523. DOI: 10.1038/nature14589.

Tatzel, M., F. von Blanckenburg, M. Oelze, J. Bouchez, and D. Hippler (2017). "Late Neoproterozoic seawater oxygenation by siliceous sponges". In: *Nature Communications* 8. DOI: 10.1038/s41467-017-00586-5.

Trappe, J. (2001). "A nomenclature system for granular phosphate rocks according to depositional texture". In: *Sedimentary Geology* 145. DOI: 10.1016/S0037-0738(01)00103-8.

Veizer, J., D. Ala, K. Azmy, P. Bruckschen, D. Buhl, F. Bruhn, G. A. Carden, A. Diener, S. Ebneth, Y. Godderis, T. Jasper, C. Korte, F. Pawellek, O. G. Podlaha, and H. Strauss (1999). "87Sr/86Sr, δ13C and δ18O evolution of Phanerozoic seawater". In: *Chemical Geology* 161. DOI: 10.1016/S0009-2541(99)00081-9.

Veizer, J. and A. Prokoph (2015). "Temperatures and oxygen isotopic composition of Phanerozoic oceans". In: *Earth-Science Reviews* 146. DOI: 10.1016/j.earscirev.2015.03.008.

Veizer, J. (1989). "Strontium Isotopes in Seawater through Time". In: *Annual Review of Earth and Planetary Sciences* 17. DOI: 10.1146/annurev.ea.17.050189.001041.

Wang, J., D. Chen, D. Yan, H. Wei, and L. Xiang (2012). "Evolution from an anoxic to oxic deep ocean during the Ediacaran–Cambrian transition and implications for bioradiation". In: *Chemical Geology* 306-307. DOI: 10.1016/j.chemgeo.2012.03.005.

Wang, W., R. Matsumoto, H. Wang, S. Ohde, A. Kano, and X. Mu (2002). "Isotopic chemostratigraphy of the upper sinian in Three gorges area". In: *Acta micropalaeontologica Sinica* 19.

Weber, B., M. Steiner, S. Evseev, and G. Yergaliev (2013). "First report of a Meishucun-type early Cambrian (Stage 2) ichnofauna from the Malyi Karatau

area (SE Kazakhstan): Palaeoichnological, palaeoecological and palaeogeographical implications". In: *Palaeogeography, Palaeoclimatology, Palaeoecology* 392. DOI: `10.1016/j.palaeo.2013.08.021`.

Wen, H., J. Carignan, Y. Zhang, H. Fan, C. Cloquet, and S. Liu (2011). "Molybdenum isotopic records across the Precambrian-Cambrian boundary". In: *Geology* 39. DOI: `10.1130/G32055.1`.

White, R. and D. McKenzie (1989). "Magmatism at rift zones: The generation of volcanic continental margins and flood basalts". In: *Journal of Geophysical Research* 94. DOI: `10.1029/JB094iB06p07685`.

Wille, M., T. F. Nägler, B. Lehmann, S. Schröder, and J. D. Kramers (2008). "Hydrogen sulphide release to surface waters at the Precambrian/Cambrian boundary". In: *Nature* 453. DOI: `10.1038/nature07072`.

Xiao, S., K. A. McFadden, S. Peek, A. J. Kaufman, C. Zhou, G. Jiang, and J. Hu (2012). "Integrated chemostratigraphy of the Doushantuo Formation at the northern Xiaofenghe section (Yangtze Gorges, South China) and its implication for Ediacaran stratigraphic correlation and ocean redox models". In: *Precambrian Research* 192-195. DOI: `10.1016/j.precamres.2011.10.021`.

Yuan-Hui, L. (1991). "Distribution patterns of the elements in the ocean: A synthesis". In: *Geochimica et Cosmochimica Acta* 55. DOI: `10.1016/0016-7037(91)90485-N`.

Zhang, J., T. Fan, T. J. Algeo, Y. Li, and J. Zhang (2016). "Paleo-marine environments of the Early Cambrian Yangtze Platform". In: *Palaeogeography, Palaeoclimatology, Palaeoecology* 443. DOI: `10.1016/j.palaeo.2015.11.029`.

Zhang, X., D. Shu, J. Han, Z. Zhang, J. Liu, and D. Fu (2014). "Triggers for the Cambrian explosion: Hypotheses and problems". In: *Gondwana Research* 25. DOI: `10.1016/j.gr.2013.06.001`.

Zhu, M., M. Lu, J. Zhang, F. Zhao, G. Li, Y. Aihua, X. Zhao, and M. Zhao (2013). "Carbon isotope chemostratigraphy and sedimentary facies evolution of the Ediacaran Doushantuo Formation in western Hubei, South China". In: *Precambrian Research* 225. DOI: `10.1016/j.precamres.2011.07.019`.

Zhu, M., J. Zhang, and A. Yang (2007). "Integrated Ediacaran (Sinian) chronostratigraphy of South China". In: *Palaeogeography, Palaeoclimatology, Palaeoecology* 254. DOI: `10.1016/j.palaeo.2007.03.025`.

Chapter 4

Magnesium Isotope Evidence for Continental Weathering During Enhanced Crustal Reworking as a Cause for the Ediacarian Mass Extinction

Jessica A. Stammeier[1]**, Dorothee Hippler**[1]**, Oliver Nebel**[2]**, and Martin Dietzel**[1]

[1] Institute of Applied Geosciences, Graz University of Technology, Rechbauerstraße 12, 8010 Graz, Austria

[2] School of Earth, Atmosphere and Environment, Monash University, Clayton VIC 3800, Australia

Abstract

The initiation of the Phanerozoic eon was accompanied by a unique (bio-) geochemical revolution in Earth´s history, leading to the rise of metazoan life. Concomitant continent re-organization and collision is associated with enhanced continental reworking and mixing of water masses through changing global ocean currents, affecting amongst others, weathering of rocks and changes in ocean nutrient balance. However, causal relations of these geologic changes and respective timing of the biologic revolution remain unclear.

Here we show that the temporal response in ocean chemistry consequent to crustal reworking is of remarkably short duration. In this study we investigate phosphatic shallow water sediments from Kazakhstan, key deposits from the Precambrian-Cambrian (Pc-C) boundary. A rapid increase of the stable Mg and radiogenic Sr isotope signatures in seawater indicates a swift and severe response in ocean chemistry to enhanced crustal reworking.

Our data strongly suggests that the oceans at the Pc-C boundary, although rapidly recovering through ocean spreading buffering, were strongly affected by this continent

re-organization. A direct link between the unique response of ocean chemistry to Gondwana assembly at the Pc-C boundary and the marked change in oceanic fauna at this time seems most plausible. Accordingly, the rise of metazoan life during the early Cambrian following the Ediacaran mass extinction was a fortuitous circumstance at a critical stage in the evolution of life.

4.1   Introduction

The Precambrian-Cambrian (Pc-C) transition has long been recognized as a critical point in Earth's history, marking the rise of metazoan life following the first aquatic mass extinction of the Ediacaran fauna ca. 541 Ma ago (e.g., Halverson, Hurtgen, et al., 2009). Among the most prominent environmental and geological factors connected to this vital change are (I) oceanic and atmospheric oxygenation; (II) continental reworking (weathering, erosion) and high nutrient influx with subsequent chert and phosphate deposition; (III) perturbation to nutrient cycling; and (IV) re-assemblage of continental masses (e.g., Zhang et al., 2014; Smith and Harper, 2013, and references therein). Despite decades of research, causal relationships between the biologic, ecologic and geologic features and respective timing of oxygenation relative to the Pc-C transition remain a matter of hot debate. Whilst the causality between those features remains controversial, an individual trigger initiating the secular change from Ediacaran to Cambrian fauna remain to be identified (Fox, 2016).

Increasing $^{87}Sr/^{86}Sr$ in seawater during the late Neoproterozoic have plausibly been linked to enhanced weathering rates and continental run-off Halverson, Wade, et al., 2010. A sharp, positive excursion at the Pc-C transition has been suggested to reflect higher influx of evolved, crustal material (Burns, Haudenschild, and Matter, 1994) counterbalanced by increased hydrothermal activity, yet later studies dismissed this spike in radiogenic Sr isotopes as poor preservation and diagenetic alteration (e.g. Li et al., 2013). Stammeier et al. (under review) confirmed the Sr isotope peak in early Cambrian carbonate and phosphorite sequences of the Malyi Karatau, Kazakhstan. The chemical sediments deposited during the Pc-C episode in a former shallow water basin were connected to global ocean evolution and interpreted to reflect continental weathering and erosion during enhanced crustal reworking. This sharp temporal relationship provides strong evidence that changes in biodiversity are consequent to geodynamic responses of plate re-organization. Whilst detailed relations are far more complex, this would generally link the critical evolution of Cambrian biota to passive continental dynamics.

A critical test for the degree of continental weathering is potentially captured in distinct stable isotope signatures of authigenic, abiotic shallow water sediments. Magnesium is a key component for both chemical weathering and abiotic carbonate precipitation (Berner, Lasaga, and Garrels, 1983). Thus, seawater Mg isotope composition

is largely influenced by flux imbalances between weathering and precipitation processes and have been used before e.g., to trace weathering changes (E. T. Tipper, Galy, and Bickle, 2006; Liu, 2013; Wimpenny et al., 2014; Kasemann et al., 2014; B. G. Pokrovsky, Mavromatis, and O. S. Pokrovsky, 2011).

Here, we present new Mg isotope data for the Kazakhstan section complementary to already reported Sr isotope variations (Stammeier et al. under review). Combined with refined global $^{87}Sr/^{86}Sr$ seawater signatures, we evaluate the consequences of different Mg and Sr isotope pools in a dynamic time-dependent state model and validate these results with plausible causes for seawater excursions in the light of enhanced weathering rates, carbonate precipitation and hydrothermal activity.

4.2   Sample Description

The Koksu section and the herein investigated samples have previously been described in detail by Stammeier et al. (under review) in terms of petrography and geochemistry. A summary of the investigated sample material and micrographs can be found in the digital data repository. Briefly, the section is located in the Malyi Karatau mountain range, south Kazakhstan and comprises sedimentary rocks of the Fortunian and stage 2 of the lower Cambrian (541 - 521 Ma, Figure 4.1 & Figure 4.2). The 50 m profile crops out along an exploration trench comprising a con-
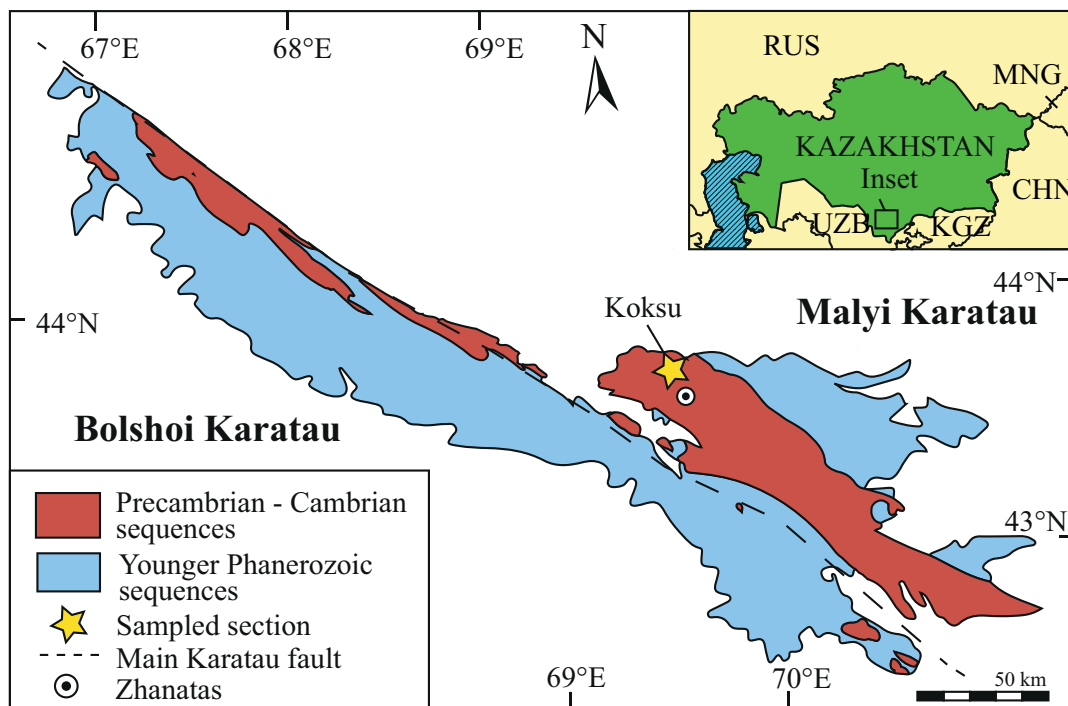
FIGURE 4.1: Schematic geologic map of the Malyi and Bolshoi Karatau Mountain range (simplified after Eganov, Sovetov, and Yanshin, 1986). The Koksu section (43.653611, 69.636389, WGS84) is located at the margin of a former shallow water basin.

secutive sequence of the Chulaktau Formation, which consists mainly of cherts and

phosphorites. The investigated samples belong to the two lowermost units (1) Aksai Chert, bedded, dark-colored cherts with dolomite and phosphate fractions, and (2) Lower Phosphorite, granular phosphorites with a calcite and/or dolomite matrix. The dolomite matrix forms a mosaic structure of anhedral grains. Internal structure, element and isotope systematics classified these rocks as near primary sedimentary rocks (see detailed discussion in Stammeier et al. under review).

4.3　Results and Discussion

Stable Mg isotopes and radiogenic Sr throughout the sedimentary profile Mg isotope analysis of the acid-soluble fraction yielded δ^{26}Mg values ranging from -2.3 ‰ to 0.5 ‰ (DSM3) with a mean of -1.0 $\pm$ 0.2 ‰ (2 SE). The observed temporal trend of decreasing δ^{26}Mg towards younger samples (Figure 4.2, Appendix A) correlates considerably with previously investigated ^{87}Sr/^{86}Sr values (Stammeier et al., under review). Moreover, δ^{26}Mg anti-correlate with their corresponding δ^{13}C$_{carb}$ and δ^{18}O$_{carb}$ (Figure 4.2), the latter being strongly linked to environmental conditions.
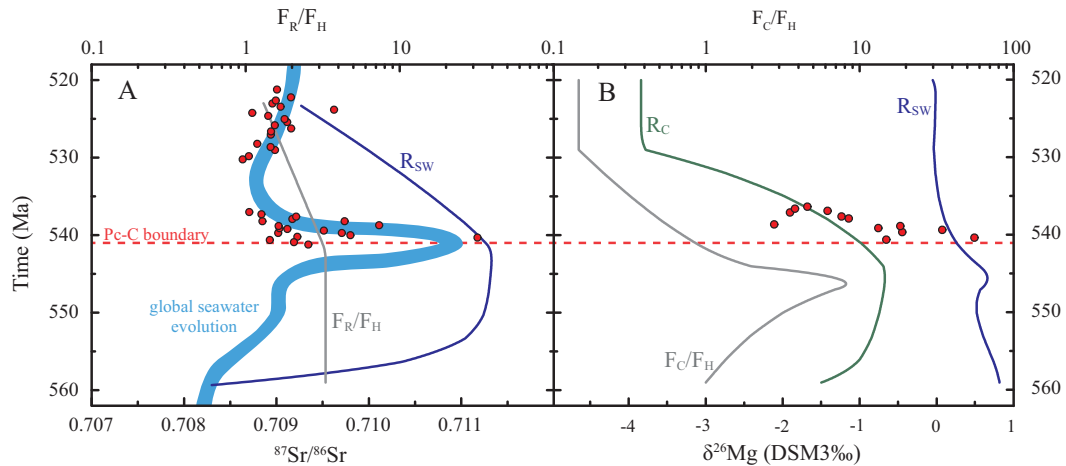
FIGURE 4.2: Compiled isotope profile of the investigated Koksu section. Both Mg-Sr and C-O isotopes display the same temporal trend, calculated as the moving average (black line). Sr, C and O isotope data from (Stammeier et al. under review). Ky. Fm = Kyrshabakty formation, AC = Aksei Chert, LP = Lower Phosphorite, SM = Shale Member after (Heubeck, Ergaliev, and Evseev, 2013). If not indicated otherwise, uncertainty (2 SD) is within symbol size.

4.3.1　^{87}Sr/^{86}Sr seawater evolution in response to changing continental weathering and hydrothermal fluxes

The authenticity and meaning of both, stable Mg and radiogenic Sr isotopes can be tested with a mass balance model that equates elemental and isotopic input and output fluxes for the past ocean basin. To reconstruct the radiogenic Sr isotope evolution during the Pc-C transition we used a time-dependent dynamic state model

based on the equation

$$\frac{dN\,R_{SW}}{dt} = \sum F_{in}R_{in} - \sum F_{out}R_{out} \tag{4.1}$$

describing the isotopic evolution R_{SW} of reservoir N as a function of the fluxes F in and out of the reservoir with the attributed isotope composition R (e.g., Richter, Rowley, and DePaolo, 1992). For the Sr isotope ocean budget, $R_{SW} = R_{out}$, as Sr is not fractionating during carbonate precipitation, which constitutes the main sink of Sr (Palmer and Edmond, 1989). The remaining fluxes into the ocean are mainly of riverine (F_R), hydrothermal (F_H) and diagenetic (F_D) origin. Assuming $dR_{sw}/dt = 0$ equation 4.1 yields the steady state equation

$$R_{SW-SSr} = \frac{F_R R_R + F_H R_H + F_D R_D}{F_R + F_H + F_D} \tag{4.2}$$

Considering the residence time (τ) of Sr as

$$\tau = \frac{N}{\sum F_{in}} \tag{4.3}$$

the time-dependent evolution can be described by

$$R_{SW}(t) = R_{SW-S} - (R_{SW-S} - R_{SW-t_0})e^{\frac{\Delta t}{\tau}} \tag{4.4}$$

(detailed mathematical derivation is given by Hodell et al., 1989). Using equation (4.4) we forced the riverine (F_R) and hydrothermal (F_H) flux, leaving diagenetic flux (FD) constant, in an iterative approach over the time span from mid-Ediacaran (560 Ma) to the Early Cambrian (521 Ma) in steps of 1 myr. The initial fluxes Fin are reported in Table 4.1 and represent present day values. Isotope ratios Rin were chosen as $R_R = 0.714$ to represent increased continental weathering rates, RD = 0.708 and $R_H = 0.703$ according to ^{87}Sr/^{86}Sr seawater and mantle evolution during the Ediacaran, respectively (Wilson, 1989; Halverson, Wade, et al., 2010).

TABLE 4.1: Model parameter used to calculate ^{87}Sr/^{86}Sr$_{SW}$ and δ^{26}Mg$_{SW}$ & δ^{26}Mg$_{Carb}$

	Parameter	Sr	Mg
Source:	F_R	3.3 *10^{10}	5.6*10^{12}
	F_D	0.3 *10^{10}	2.8*10^{12}
	F_H	1.0 *10^{10}	2.8*10^{12}
	N	1.25*10^{17}	7.3*10^{19}
Isotope ratios:	R_R	0.714	-0.5‰
	R_C	0.708	-2.0‰
	R_H	0.703	
	R_N		0.8‰

The modelled ^{87}Sr/^{86}Sr seawater evolution shown in Figure 4.3 shows a rapid increase of Sr values in response to a simultaneous increase of 5%/myr in F_R and F_R

approaching $^{87}Sr/^{86}Sr$ values of ca. 0.711. While F_H increased continuously from 560 – 521 Ma, F_R and thus weathering was considered to have reached a maximum at the Pc-C boundary (541 Ma.), causing the reversed $^{87}Sr/^{86}Sr$ evolution. The modelled Sr isotope evolution describing a rapid increase in the lead up to the Pc-C boundary followed by a rapid decrease is in agreement with $^{87}Sr/^{86}Sr$ data in Kazakhstan and a proposed global seawater Sr evolution (Figure 4.3). Note that the model successfully recreates the magnitude, however, does not recreate the extremely short duration of the positive excursion in global seawater $^{87}Sr/^{86}Sr$. This suggests more variability in flux-dynamics with (I) a rapid increase of weathering (F_R), and/or (II) varying source regions. The model shows, that a 5% increase in weathering and erosion rates (i.e., the riverine input) is sufficient to cause such a positive excursion, despite similarly increasing hydrothermal activity.
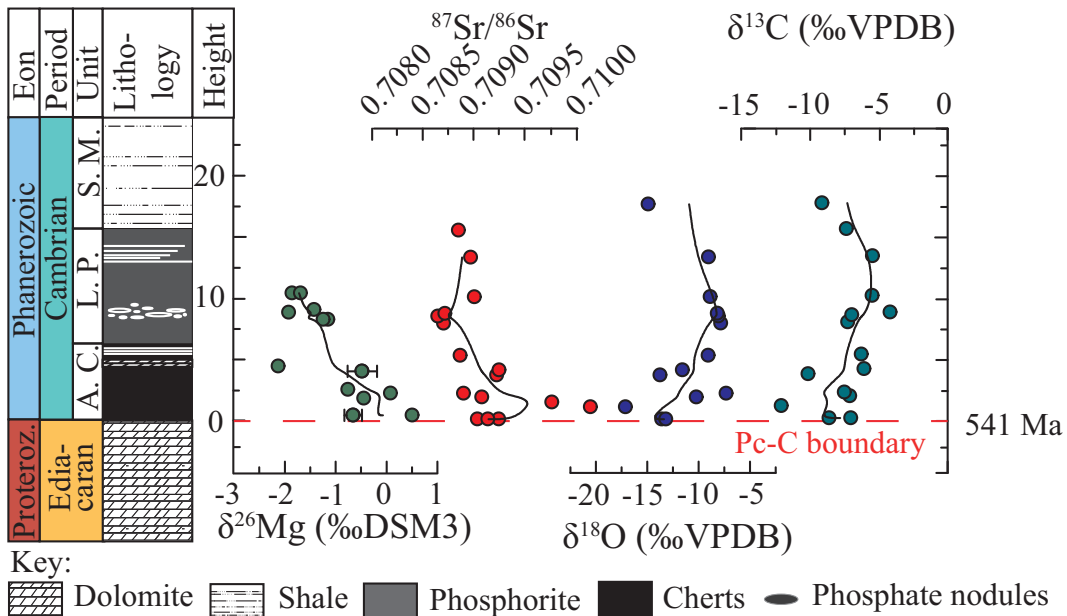
FIGURE 4.3: Calculated Mg and Sr isotope values in a time-dependent dynamic state model. Red circles indicate isotope ratios measured in early Cambrian Kazakh strata. A: Modelled $^{87}Sr/^{86}Sr$ seawater composition (R_{SW}) in response to changing weathering (F_R) and hydrothermal (F_H) fluxes, shown as F_R/F_H. Thick blue line indicates recorded $^{87}Sr/^{86}Sr$ seawater evolution as compiled by Stammeier et al. (under review) and references therein. B: Modelled $\delta^{26}Mg$ of seawater (R_{SW}) and carbonate (R_C) in response to increased diagenesis (F_C) and hydrothermal activity (F_H), shown as F_C/F_H.

$\delta^{26}Mg$ for seawater and carbonates in response to changing weathering and carbonate precipitation For seawater $\delta^{26}Mg$ values, the analogous time-dependent dynamic state model using equations (4.1) and (4.4) as for $^{87}Sr/^{86}Sr$ in seawater is applied. For the Mg budget in seawater the main source is riverine influx (F_R), which is counterbalanced by output via carbonate precipitation from sea water (F_C) and hydrothermal removal through interaction of sea water with MORB (F_H). Here, we can assume that $R_{SW} = R_H$ as Mg fractionation through hydrothermal removal is generally negligible (Villiers, Dickson, and Ellam, 2005), which yields in the equation

$$R_{SW-SMg} = \frac{F_R R_R - F_C R_C}{F_R - F_C} \tag{4.5}$$

at steady state conditions. Experimental studies have shown that dolomite formation, which, given stoichiometry, constitute the majority of the Mg sink though carbonate removal, can be estimated to account for $\Delta^{26}/^{24}Mg_{Dol-SW}$ of ca. -1.7 to -2.7 ‰ (Higgins and Schrag, 2010), so that Mg isotopes in carbonates can only indirectly reflect seawater composition. Thus, we employed a two-step iterative approach to calculate the $\delta^{26}Mg$ of carbonates as a function of changing seawater composition. In the first step we calculated $R_{SW(t)}$, representing the seawater $\delta^{26}Mg$ in response to changing fluxes. These calculated values were used to calculate $\delta^{26}Mg_{carb}$, solving equation (4.5) for R_C. In the next iteration this new R_C value was then used to calculate the next R_{SW}. In this model, we chose to change riverine influx F_R and removal through carbonate precipitation F_C, as continental weathering and carbonate sink during carbonate deposition were likely the strongest influences on $\delta^{26}Mg_{SW}$ at that time. With the condition that $\Sigma F_{in} = \Sigma F_{out}$, F_H is defined by the difference of $F_R - F_C$. The initial values are reported in table 1. The influx of riverine Mg F_R is adapted from (Wilkinson and Algeo, 1989) and removed from the ocean by F_H and F_C to equal proportions. $\delta^{26}Mg$ of the riverine influx was set to $R_R = $ -0.5 ‰, representing silicate dominated weathering and kept stable (see discussion below, (Wimpenny et al., 2014; E. T. Tipper, Galy, and Bickle, 2006)). For $\delta^{26}Mg$ carb the average value of -2 ‰ from terminal Neoproterozoic dolomites was taken from B. G. Pokrovsky, Mavromatis, and O. S. Pokrovsky (2011). E. Tipper et al. (2006) suggest that during times of increased dolomitization $\delta^{26}Mg_{SW}$ could have been up to 1.5 ‰ isotopically heavier than present-day seawater. Accordingly, initial $\delta^{26}Mg_{SW}$ was set to $+ 0.8$ ‰. Wilkinson and Algeo (1989) suggest that the Mg sink in seawater through dolomitization accounts for as much as 90% during enhanced dolomitization. In accordance with the ongoing massive dolomite deposition during the Neoproterozoic, F_C was increased by 10%/myr converging 90% dolomite removal and then reversed by -10%/myr until values of 13% dolomite removal were reached, i.e., present-day conditions (Elderfield and Schultz, 1996), and then kept stable thereafter.

4.3.2 The significance of $\delta^{26}Mg$ composition of the riverine input

Isotopically heavy $\delta^{26}Mg$ seawater values can either be caused by preferential removal of light Mg isotopes, i.e. during extreme dolomitization events, or input of heavy isotopes, i.e. through silicate dominated riverine influx. However, our box model needs to be confirmed by both, Sr and Mg fluxes, so that dolomitization may contribute to the scatter in Mg-Sr isotope co-variations, but cannot be the main reason for the coupled isotope excursion. Despite uncertainty in the input parameters, it is apparent that the isotope modelling successfully recreates the observed amplitude at the Pc-C

transition, confirming continental weathering and run-off as the driving force for the $^{87}Sr/^{86}Sr$ - $\delta^{26}Mg$ isotope excursions (Figure 4.3).

E. T. Tipper, Galy, and Bickle (2006) showed that modern rivers draining silicate rocks can be as heavy as -0.3 ‰ and rivers draining carbonate rocks record values as low as -2.7 ‰. In weathering dominated rivers as e.g. in the Himalaya, these two endmembers combine to a riverine $\delta^{26}Mg$ of -0.9 ‰. To evaluate the significance of the isotope ratio of riverine influx (R_C) we increase carbonate removal (F_C) up to 90% removal of total influx and combined this with three different isotope ratios (R_R) of the riverine influx to represent the different endmembers from (a) carbonate dominated weathering with a $\delta^{26}Mg$ value of -2.7 ‰, (b) silicate dominated weathering with a $\delta^{26}Mg$ value of -0.3 ‰, and (c) $\delta^{26}Mg$ value of -0.9 ‰ representing a generally or mixed weathering dominated river (Figure 4.4, E. T. Tipper, Galy, and Bickle, 2008). For (a) calculated carbonate $\delta^{26}Mg$ values are unrealistically low with a maximum value of -3.5 ‰ and a rapid decrease towards < -10 ‰. Even by using the $\delta^{26}Mg$ value of scenario (c) it was not possible to achieve high $\delta^{26}Mg$ carb approaching near 0 ‰ values during peaking weathering rates and simultaneous enhanced dolomitization (Figure 4.4). The best fit was achieved with an R_R value of -0.5 ‰ for $\delta^{26}Mg$, similar to the value (b), confirming the Sr-Mg isotope systematics.
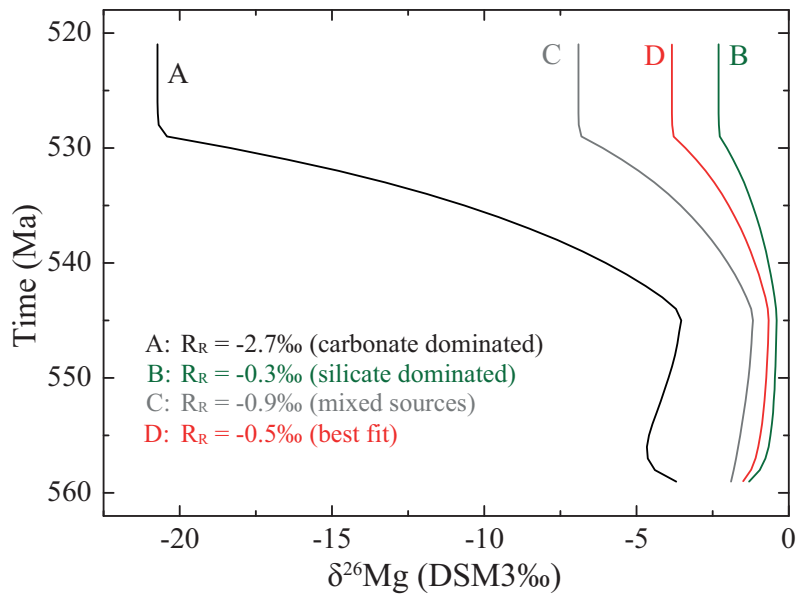
FIGURE 4.4: Modelled $\delta^{26}Mg$ in carbonates (R_C) using different riverine $\delta^{26}Mg$ (R_R) input values, representing (A) carbonate, (B) silicate, (C) generally or mixed weathering dominated endmembers, and (D) best fit results.

4.4 Paleoenvirnonmental Implications

Although reconstruction of the evolution of δ^{26}Mg values of past seawater and related carbonate deposits is highly challenging, as Mg isotope fractionation between the carbonate precipitate and reactive solution depends on multiple factors, e.g. temperature, precipitation rate and/or alkalinity, the modeled δ^{26}Mg carb reproduce the observed Koksu trend within 0.5-1 ‰ deviation from measured δ^{26}Mg carb (Figure 4.3). As shown above, the isotope composition of riverine input is crucial to the seawater δ^{26}Mg mass-balance and reveals the dominance of crustal reworking for the Pc-C transition. Our isotope modelling suggests that the dominance of continental influx to the ocean budget for Mg and Sr is rapidly counterbalanced by hydrothermal activity (Figure 4.3).

Enhanced erosion rates are expected in the aftermath of several Neoproterozoic glaciations, such as e.g. Sturtian and Marinoan (Kasemann et al., 2014), and as a consequence of Gondwana assembly from 0.8-0.6 Ga (Meert and Van Der Voo, 1997). Weathering and associated riverine run-off are thus the likely cause for the steady increase in Sr isotopes during the late Neoproterozoic era (cf. Halverson, Wade, et al., 2010) along with an increase in ocean alkalinity and transport of nutrients, e.g., P, to the oceans (Smith and Harper, 2013).

The sharp excursion in seawater ^{87}Sr/^{86}Sr together with high δ^{26}Mg at the Pc-C transition (Figure 4.2), however, marks a single, critical event in mountain building that cannot be explained by merely enhanced weathering rates, but requires a severe geodynamic event. The timing coincides with a range of global orogenies, e.g., Pan-African orogeny (650-500 Ma, Miller, 1983), and Cadomian orogeny (750-540 Ma, Linnemann et al., 2014), associated with the Gondwana assembly. Whilst current geotectonic plate reconstruction lacks the temporal resolution to pinpoint a single, unique collisional event, the negative excursion in global Hf isotope data indicates an unprecedented collision of continental landmass at the time of Gondwana assembly (Roberts, 2012). Such a collisional event and associated crustal reworking would cause a severe increase of riverine input to the ocean, resulting in high ^{87}Sr/^{86}Sr and δ^{26}Mg.

The observed isotope excursions are unprecedented in its extremes and relatively short duration (Figure 4.2), however, as extreme and sudden as either Ediacaran mass extinction or Cambrian explosion. It thus seems likely that a single event, as e.g. coincidence of continental collision, along with reworking of evolved continental crust and an associated release of nutrients, led to a possibly sudden change in marine biota at the Pc-C transition.

Acknowledgements

References

Berner, R. A., A. C. Lasaga, and R. M. Garrels (1983). "The carbonate-silicate geochemical cycle and its effect on atmospheric carbon dioxide over the past 100 million years". In: *American Journal of Science* 283. DOI: `10.2475/ajs.283.7.641`.

Burns, S. J., U. Haudenschild, and A. Matter (1994). "The strontium isotopic composition of carbonates from the late Precambrian (560-540Ma) Huqf Group of Oman". In: *Chemical Geology* 111. DOI: `10.1016/0009-2541(94)90094-9`.

Eganov, E. A., K. Y. Sovetov, and A. L. Yanshin (1986). "Proterozoic and Cambrian phosphorite deposits: Karatau, southern Kazakhstan, USSR". In: *Phosphate Deposits of the World.* Ed. by P. J. Cook and J. H. Shergold. Vol. 1. Cambridge University Press, pp. 175–189.

Elderfield, H. and A. Schultz (1996). "Mid-Ocean Ridge Hydrothermal Fluxes and the Chemical Composition of the Ocean". In: *Annual Review of Earth and Planetary Sciences* 24. DOI: `10.1146/annurev.earth.24.1.191`.

Fox, D. (2016). "What sparked the Cambrian explosion?" In: *Nature* 530. DOI: `10.1038/530268a`.

Halverson, G. P., M. Hurtgen, S. M. Porter, and A. S. Collins (2009). "Neoproterozoic-Cambrian Biogeochemical Evolution". In: *Neoproterozoic-Cambrian Tectonics, Global Change And Evolution: A Focus On South Western Gondwana.* Ed. by C. Gaucher, A. N. Sial, H. E. Frimme, and G. P. Halverson. Vol. 16. Developments in Precambrian Geology. Chap. 10, pp. 351–365. DOI: `10.1016/S0166-2635(09)01625-9`.

Halverson, G. P., B. P. Wade, M. T. Hurtgen, and K. M. Barovich (2010). "Neoproterozoic chemostratigraphy". In: *Precambrian Research* 182. DOI: `10.1016/j.precamres.2010.04.007`.

Heubeck, C., G. Ergaliev, and S. Evseev (2013). "Large-Scale Seismogenic Deformation of A Carbonate Platform Straddling the Precambrian-Cambrian Boundary, Karatau Range, Kazakhstan". In: *Journal of Sedimentary Research* 83. DOI: `10.2110/jsr.2013.76`.

Higgins, J. A. and D. P. Schrag (2010). "Constraining magnesium cycling in marine sediments using magnesium isotopes". In: *Geochimica et Cosmochimica Acta* 74. DOI: `10.1016/j.gca.2010.05.019`.

Hodell, D. A., P. A. Mueller, J. A. McKenzie, and G. A. Mead (1989). "Strontium isotope stratigraphy and geochemistry of the late Neogene ocean". In: *Earth and Planetary Science Letters* 92. DOI: `10.1016/0012-821X(89)90044-7`.

Kasemann, S. A., P. A. Pogge von Strandmann, A. R. Prave, A. E. Fallick, T. Elliott, and K. Hoffmann (2014). "Continental weathering following a Cryogenian glaciation: Evidence from calcium and magnesium isotopes". In: *Earth and Planetary Science Letters* 396. DOI: `10.1016/j.epsl.2014.03.048`.

Li, D., H. F. Ling, G. A. Shields-Zhou, X. Chen, L. Cremonese, L. Och, M. Thirlwall, and C. J. Manning (2013). "Carbon and strontium isotope evolution of seawater across the Ediacaran–Cambrian transition: Evidence from the Xiaotan section, NE Yunnan, South China". In: *Precambrian Research* 225. DOI: `10.1016/j.precamres.2012.01.002`.

Linnemann, U., A. Gerdes, M. Hofmann, and L. Marko (2014). "The Cadomian Orogen: Neoproterozoic to Early Cambrian crustal growth and orogenic zoning along the periphery of the West African Craton—Constraints from U–Pb zircon ages and Hf isotopes (Schwarzburg Antiform, Germany)". In: *Precambrian Research* 244. DOI: `10.1016/j.precamres.2013.08.007`.

Liu, X.-M. (2013). "Tracing continental weathering using lithium and magnesium isotopes: insights from the chemical weathering of columbia river basalts asnd mass balance modeling". In:

Meert, J. G. and R. Van Der Voo (1997). "The assembly of Gondwana 800-550 Ma". In: *Journal of Geodynamics* 23. DOI: `10.1016/S0264-3707(96)00046-4`.

Miller, R. M. (1983). *Evolution of the Damara Orogen of South West Africa/Namibia.* Geological Society of South Africa, p. 515.

Palmer, M. and J. Edmond (1989). "The strontium isotope budget of the modern ocean". In: *Earth and Planetary Science Letters* 92. DOI: `10.1016/0012-821X(89)90017-4`.

Pokrovsky, B. G., V. Mavromatis, and O. S. Pokrovsky (2011). "Co-variation of Mg and C isotopes in late Precambrian carbonates of the Siberian Platform: A new tool for tracing the change in weathering regime?" In: *Chemical Geology* 290. DOI: `10.1016/j.chemgeo.2011.08.015`.

Richter, F. M., D. B. Rowley, and D. J. DePaolo (1992). "Sr isotope evolution of seawater: the role of tectonics". In: *Earth and Planetary Science Letters* 109. DOI: `10.1016/0012-821X(92)90070-C`.

Roberts, N. M. W. (2012). "Increased loss of continental crust during supercontinent amalgamation". In: *Gondwana Research* 21. DOI: `10.1016/j.gr.2011.08.001`.

Smith, M. P. and D. T. Harper (2013). "Causes of the Cambrian Explosion". In: *Science* 341. DOI: `10.1126/science.1239450`.

Tipper, E., A. Galy, J. Gaillardet, M. J. Bickle, H. Elderfield, and E. Carder (2006). "The magnesium isotope budget of the modern ocean: Constraints from riverine magnesium isotope ratios". In: *Earth and Planetary Science Letters* 250. DOI: `10.1016/j.epsl.2006.07.037`.

Tipper, E. T., A. Galy, and M. J. Bickle (2006). "Riverine evidence for a fractionated reservoir of Ca and Mg on the continents: Implications for the oceanic Ca cycle". In: *Earth and Planetary Science Letters* 247. DOI: `10.1016/j.epsl.2006.04.033`.

– (2008). "Calcium and magnesium isotope systematics in rivers draining the Himalaya-Tibetan-Plateau region: Lithological or fractionation control?" In: *Geochimica et Cosmochimica Acta* 72. DOI: `10.1016/j.gca.2007.11.029`.

Villiers, S. de, J. A. D. Dickson, and R. M. Ellam (2005). "The composition of the continental river weathering flux deduced from seawater Mg isotopes". In: *Chemical Geology* 216. DOI: `10.1016/j.chemgeo.2004.11.010`.

Wilkinson, B. H. and T. J. Algeo (1989). "Sedimentary carbonate record of calcium-magnesium cycling". In: *American Journal of Science* 289. DOI: `10.2475/ajs.289.10.1158`.

Wilson, M. (1989). *Igneous petrogenesis.* Ed. by M. Wilson, p. 466.

Wimpenny, J., Q. Z. Yin, D. Tollstrup, L. W. Xie, and J. Sun (2014). "Using Mg isotope ratios to trace Cenozoic weathering changes: A case study from the Chinese Loess Plateau". In: *Chemical Geology* 376. DOI: `10.1016/j.chemgeo.2014.03.008`.

Zhang, X., D. Shu, J. Han, Z. Zhang, J. Liu, and D. Fu (2014). "Triggers for the Cambrian explosion: Hypotheses and problems". In: *Gondwana Research* 25. DOI: `10.1016/j.gr.2013.06.001`.

Chapter 5

Strontium Isotopes

Oliver Nebel[1] and Jessica A. Stammeier[2] [I] [II]

[1] School of Earth, Atmosphere and Environment, Monash University, Clayton/ Melbourne, VIC, Australia
[2] Institute of Applied Geosciences, Graz University of Technology, Graz, Austria

Abstract

Strontium (Sr) isotopes are widely applied tracers in geoscientific applications. One of the four stable isotopes (^{87}Sr) is subject to long-term radiogenic ingrowth by radioactive decay of rubidium (^{87}Rb). Resultant isotope variations in ^{87}Sr/^{86}Sr, but also other stable isotope variations, can be employed to trace mixing of global reservoirs, ranging from high-temperature-pressure processes preserved in solid rock to low-temperature, environmental conditions in surface waters, oceans, chemical sediments, or biogeochemistry. A second, frequent application is the dating of rock-forming processes using the Rb-Sr decay scheme, ranging in age from the infant stages of the solar system to most recent geologic events.

This chapter is a contribution to 'Encyclopedia of Geochemistry: A Comprehensive Reference Source on the Chemistry of the Earth' dealing with different aspects of Sr isotopes, including background, introduction to analytics, and the different applications in scientific research questions. These range from radiogenic Sr isotopes as a tracer in high and low temperature environments, application of stable Sr isotopes, and Sr isotopes in forensic sciences.

Reprinted by permission from Springer Customer Service Centre GmbH: Springer Nature Encyclopedia of Geochemistry by W. M. White (Ed.) 2018

The chapter can be found online, and in appendix C.

[I]Both authors contributed equally
[II]https:doi.org10.1007978-3-319-39193-9__137-1

Chapter 6

In-situ Raman Spectroscopy of Amorphous Calcium Phosphate to Crystalline Hydroxyapatite Transformation

Jessica A. Stammeier[1]*, Bettina Purgstaller[1], Dorothee Hippler[1], Vasileios Mavromatis[1], and Martin Dietzel[1]

[1] Institute of Applied Geosciences, Graz University of Technology, Rechbauerstraße 12, 8010 Graz, Austria
*corresponding author email: j.stammeier@web.de

Abstract

Amorphous calcium phosphate ($Ca_3(PO_4)_2 * nH_2O$; n = 3 – 4.5; ACP) is a precursor phase of the mineral hydroxyapatite ($Ca_5(PO_4)_3(OH)$; HAP) that in natural settings is reported to occur during both authigenic and biogenic mineral formation. In aqueous solutions ACP rapidly transforms to the crystalline phase. The transformation rate is highly depended on the physico-chemical conditions, most likely on: Ca & PO_4 concentration, *pH* and temperature. In this study, we conducted a calcium phosphate precipitation experiment at 20 °C and *pH* 9.2, in order to study the temporal evolution of the phosphate mineralogy. We monitored and assessed the transformation process of ACP to crystalline HAP using highly time-resolved *in-situ* Raman spectroscopy at 100 spectra per hour, in combination with solution chemistry and XRD data. Transformation of ACP via a transient octacalcium phosphate (OCP) to crystalline HAP occured within 18 hours, as it is illustrated in a clear peak shift in Raman spectra from 950 cm^{-1} to 960 cm^{-1} as well as in a sharpening of the 960 cm^{-1} peak.

Keywords

Amorphous Calcium Phosphate, *in-situ* Monitoring, Raman Spectroscopy, Intermediate Phase, Apatite

6.1   Introduction

Hydroxyapatite ($Ca_5(PO_4)_3(OH)$; HAP, Table 6.1) has a wide range of occurrences and uses. Those span from products of biomineralization and post-sedimentation in natural surroundings (Omelon and Grynpas, 2008; Omelon, Ariganello, et al., 2013; H. N. Schulz and H. D. Schulz, 2005); add-ons in composites for tailored properties e.g., of cements and water treatment agents (Bellier, Chazarenc, and Comeau, 2006; Molle et al., 2005; Zoltek, 1974) to innovative medical-related products e.g., for remineralization of teeth or for bone grafts (Combes and Rey, 2010; Eanes, 2001; Legeros, 1988; LeGeros, 1993). Amorphous calcium phosphate ($Ca_3(PO_4)_2 * nH_2O$; n = 3 – 4.5; ACP) is often a precursor phase of the mineral HAP that can be formed in natural settings during either authigenic or biogenic mineral formation. ACP has already been identified as a transient phase during bone mineralization in the 1960ies by mere optical measures (Gonzales and Karnovsky, 1961). This observation was later confirmed in several studies by X-ray diffraction (e.g., LeGeros, 1981). Further, ACP was found during the mineralization of fish bone (Mahamid et al., 2008), during microbially-mediated formation of phosphatic sediments (Arning et al., 2009), or mineralization of teeth (Beniash et al., 2009) highlighting the relevance of investigating ACP transformation pathways in medical, geological, biological or paleontological fields of science. In aqueous environments, the meta-stable ACP precipitates as intermediate or transitional phase, which then rapidly converts into the crystalline apatite-phase (Kim et al., 2005). The transformation rate depends highly on the physico-chemical conditions of the solution, e.g., element availability (Kibalczyc et al., 1990; LeGeros, Bleiwas, et al., 1999; Termine, Peckauskas, and Posner, 1970), pH and temperature (Christoffersen et al., 1989; LeGeros, Mijares, et al., 2005; Lundager Madsen and Christensson, 1991). In alkaline media, however, transformation pathways were found to be more complex, because ACP rapidly hydrolyses to the meta-stable octacalciumphosphate ($Ca_8H_2(PO_4)_6 * 5H_2O$; OCP), which subsequently transforms to HAP (Johnsson and Nancollas, 1992).

Time-resolved spectroscopic measurements can provide useful information on the nucleation and growth processes of minerals. Raman spectroscopy (RS), a form of vibrational spectroscopy, is based on the excitation of molecular vibration by electromagnetic waves. In geosciences, RS is most commonly used as a fingerprinting tool for identifying and characterizing minerals. As such, time-resolved *in-situ* RS presents

an easy, rapid and reliable tool with a wide range of applications, e.g., identifying aqueous species, monitoring pathways of mineral formation, quantitative determination of mineral contents as well as studying the exchange kinetics of e.g., O-isotopes (Geisler et al., 2012; Purgstaller, Mavromatis, et al., 2016; Purgstaller, Dietzel, et al., 2017; Montes-Hernandez and Renard, 2016). Further, RS is very sensitive to short-range ordered (amorphous) phases. It thus constitutes an excellent tool to study the transformation of amorphous to crystalline materials (e.g., Nasdala et al., 2004, and references therein). An additional advantage of *in-situ* RS is that it is non-invasive and is thus especially suited for experimental studies with critical sample size or material. No material is consumed during RS analysis, reducing costs and offering a valuable screening tool for quick and reliable analysis.

TABLE 6.1: Selected calcium phosphates and their respective chemical formula and molar Ca/P. After Dorozhkin (2011) and Combes and Rey (2010)

Mineral	Chemical formula	Ca/P
Amorphous Calcium Phosphate (ACP)	$Ca_3(PO_4)_2 * nH_2O$, $n = 3 - 4.5$	$1.2 - 2.5$
Octacalciumphosphate (OCP)	$Ca_8H_2(PO_4)_6 * 5H_2O$	1.33
Hydroxyapatite (HAP)	$Ca_5(OH)(PO_4)_3$	1.67

In this study we investigate the application of high temporal resolution *in-situ* RS as a new and exciting tool for (near) continuous monitoring of mineral (trans-) formation. As an exemplary study we performed calcium phosphate precipitation experiments (T = 20.00 ± 0.01 °C; *pH* 9.2 ± 0.1) in order to monitor the transformation process of ACP to crystalline HAP. Homogeneous aliquots of the experimental solution were collected at certain reaction times to follow the chemical evolution of the solution and precipitate and to assess the combined data sets for deciphering transformation kinetics. The precipitates were further investigated for their internal structure to confirm the presence of the respective mineralogical phases.

6.2 Methods

6.2.1 Experimental setup

Calcium phosphate precipitation experiments were performed at constant temperature of 20.00 ± 0.01 °C using an Easy MaxTM 102 system (Mettler Toledo) equipped with a 150 ml glass reactor and coupled with two titration units (TU), a 702 SM Titrino titrator (Methrom, TU 1) and a TitroLine alpha plus (Schott, TU 2; Figure 6.1).

Calcium phosphate precipitation was induced by titrating 50 ml of a 0.3 mol l^{-1} $CaCl_2$ solution (TU 1) at a rate of 5 ml min^{-1} to an equal volume of a 0.2 mol l^{-1}
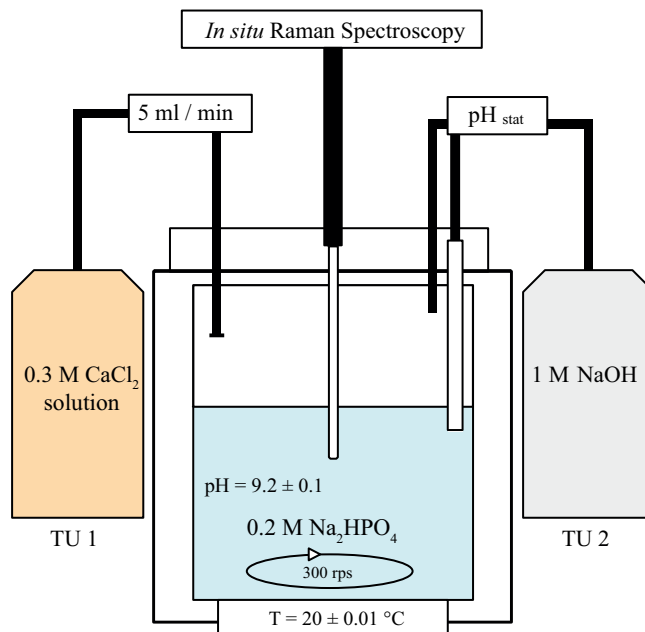
FIGURE 6.1: Experimental set up of the calcium phosphate precipitation experiment. Figure adapted from Purgstaller, Mavromatis, et al. (2016). TU = titration unit.

Na_2HPO_4 solution (glass reactor). The pH was kept constant at pH 9.2 ± 0.1 by titration of a 1 mol l^{-1} $NaOH$ solution (TU 2). Homogenization of the reactant solutions was achieved by stirring with a magnetic stirrer at 300 rpm. After 16 h of reaction time the reactant solution was transferred to a gas-tight beaker (Nalgene). Solution was stirred and kept in a temperature-controlled room at 20°C. During the experiment homogeneous aliquot samples were taken from the experimental solution and instantly filtered using 0.2 μm cellulose acetate filter. Subsequently, the separated solid samples were lyophilized using a Virtis Benchtop 3 L freeze-dryer (-58°C; 10 mbar partial vacuum). Sampling times are reported in Table 6.2.

6.2.2   Analytical procedures

Elemental concentrations of the solid samples (digested in 0.45 mol l^{-1} HNO_3, p.a.) and solutions were determined by inductively coupled plasma optical emission spectroscopy (ICP-OES) using a PerkinElmer Optima 8300 with an analytical uncertainty of $\pm$ 2 %. Qualitative X-ray diffraction (XRD) analysis for mineralogical characterization of the precipitates were performed using a PANalytical X'Pert PRO diffractometer, equipped with a Co-tube (40 kV and 40mA), a spinner stage, 0.5° divergence and anti-scattering slits, and a Scientific X'Celerator detector. Randomly oriented preparations were recorded over the range of 4-85°2θ with a step size of 0.008°2θ.

TABLE 6.2: Sample name and time of sampling (in min or h) after beginning of $CaCl_2$ titration, as well as solution chemistry (pH; Ca, P in mmol l^{-1}) and solid chemistry (Ca, P in mmol l^{-1}; Ca/P). Note outlier sample (11) with unusual solid chemistry values; compare Figure 6.2.

Sample Name	Sampling time	pH	Solution (mmol l^{-1}) Ca	P	Solid (mmol l^{-1}) Ca	P	Ca/P
1	10 min	9.42	174	0.55	8427	6401	1.32
2	17 min	9.34	172	0.37	7851	5796	1.35
3	23 min	9.30	176	0.40	7909	5806	1.36
4	30 min	9.26	165	0.37	8159	5953	1.37
5	35 min	9.23	202	0.33	8028	5871	1.37
6	43 min	9.21	195	0.24	7772	5723	1.36
7	120 min	9.03	167	0.48	7948	5750	1.38
8	180 min	9.21	187	0.25	8145	6014	1.35
9	5 h	9.55	170	0.36	7804	5630	1.39
10	6.7 h	9.26	160	0.19	7235	4955	1.46
11	18 h	9.14	164	0.24	5353	5242	1.02
12	24 h	9.00	180	0.33	8445	6022	1.40

6.2.3 Raman instrumentation

In-situ Raman spectroscopic analyses were performed using a RAMAN RXN2TM analyser from Kaiser Optical Systems with a Kaiser MR Probe head equipped with a quarter-inch immersion optic. Configuration of the experimental settings was determined using the experiment wizard of the iC RamanTM 4.1 software. The wizard automatically guides the user through all configuration steps, including experiment duration, collection of reference spectra and focusing of the instrument. Focusing of the instrument was optimized to a pixel fill of ca. 60 %. The pixel fill is the measure of intensity in absolute counts at any given wavenumber with 100 % saturation resulting in ca. 65 pixel fill. This was optimized for wavenumber $950 - 961$ cm^{-1} to an exposure time of 30 seconds. The Raman spectra were collected in 35 s intervals, consisting of 30 s exposure time and 5 s overtime, for a total of 16h enabling a near continuous monitoring. After 16 hours, Raman spectra were only collected during sampling for shorter intervals, using with the same instrument settings. Spectra were collected in the $100 - 1890$ cm^{-1} region with a resolution of 1 cm^{-1} using a laser beam with an excitation wavelength of 785 nm. For comparison, a HAP certified reference material (CRM, Sigma Aldrich) was dissolved in MiliQ. Individual reference spectra of this HAP CRM and of all titrating solutions were collected at 20.00 °C using the same instrumental settings. The obtained reference spectra were only collected for comparison purpose as no automatic calculations, e.g., phase quantifications, were conducted during or after the experiment.

6.2.4   Data handling

For Raman spectra, first hand data treatment was performed using the iC RamanTM 4.1 software (Mettler Toledo), which included baseline correction using the Pearson's method and spectra smoothing using the Savitsky-Golay filter. Intensity was normalized to the intensity of the $v4$ Raman peak of the reference spectrum. Further data treatment (peak identification and peak fitting) of the collected Raman spectra was performed by the Fityk 0.9.8 (© Wojdyr, 2010) non-linear curve fitting and data analysis software. The peaks were identified and fitted employing a PseudoVoigt function. The PseudoVoigt function is a convolution of both Lorentzian and Gaussian functions and is often better suited for peak fitting of spectroscopic data. The shape of this fitted PseudoVoigt function can be quantitatively described by its full width at half maximum (FWHM, compare Figure 6.4). The 3D surface plot from Figure 6.3 was created using the Origin 9.0.0 (© 1991 – 2012 OriginLab Corporation) software. For XRD data handling, the baseline was determined manually using the X'Pert HighScore Plus 3.0d (© 2011 PANalytical B.V.) software and subtracted after data collection.

6.3   Results and Discussion

6.3.1   Chemical evolution of experimental solution

Elemental compositions of solid and solution samples and pH are reported in Table 6.2. The addition of the $CaCl_2$ solution into the $NaHPO_4$ solution induced instant precipitation of calcium phosphate. This initial precipitation and the simultaneous titration of the NaOH solution caused large variations in the pH value within the initial stage of the experiment (Figure 6.2). After the addition of the $CaCl_2$ solution was stopped (10 min), the pH reached a more constant value, slowly dropping from pH 9.5 towards pH 9 and remained quasi constant at 9.2 ± 0.1 during 24 h of reaction time. Analysis of the reactive solution showed that all PO_4 is almost quantitatively consumed and only trace amounts of ca. 0.3 mol l^{-1} were present Table 6.2. Within this time frame the Ca concentration of the solid remained near constant at 7975 ± 320 mmol kg^{-1}. The molar Ca/P of the solid samples ranges from about 1.32 to 1.46, showing a clear increase with time (Figure 6.2B). The initial molar Ca/P of ca. 1.3 might indicate the presence of OCP, a transient phase of HAP in alkaline environments (Johnsson and Nancollas, 1992). In such kind of precipitation experiments non-stoichiometric HAP typically forms at a molar Ca/P of ca. 1.45 ± 0.05 (Johnsson and Nancollas, 1992).
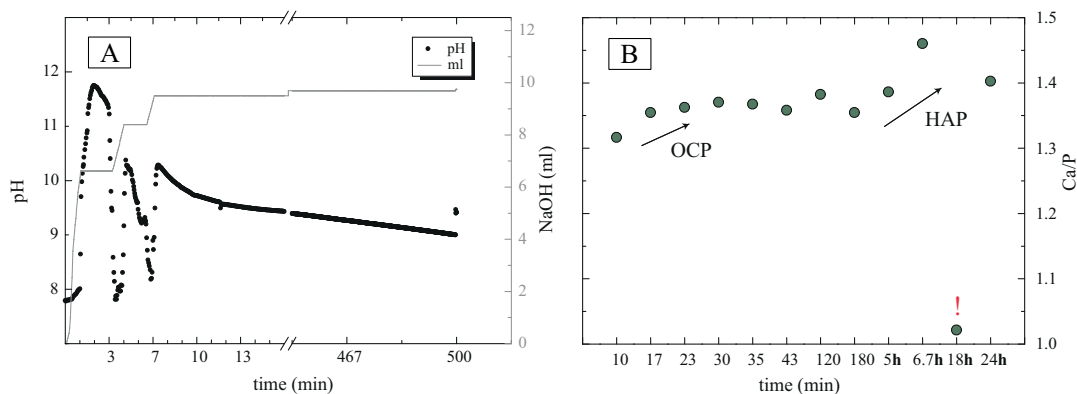
FIGURE 6.2: A: *pH* evolution of the reactive solution and titrated *NaOH* (ml) of the first 8 h of the experiment. B: Molar Ca/P ratios of solid samples. Note the outlier sample (!) after 18 h, highlighting the consequences of sampling biases.

6.3.2 *In-situ* Raman spectroscopy and solid characterization

The characteristic vibration bands of PO_4 groups in HAP crystals are (i) $v2$ bending of P-O-P at 472 cm^{-1}, (ii) $v4$ bending of P-O-P at 563 and 602 cm^{-1}, (iii) $v1$ stretching of P-O at 960–962 cm^{-1}, and (iv) $v3$ stretching of P-O stretching at 1035-1045 cm^{-1} (Cosmidis et al., 2015). For ACP, the most characteristic shift is documented by a 10 cm^{-1} shift of the $v1$ stretching towards 950 cm^{-1} (Cosmidis et al., 2015). Thus, the transformation of ACP to HAP is characterized by a shift of the $v1$ symmetrical band from a broad peak at ca. 950 cm^{-1} towards a narrow peak at 960 cm^{-1} (Combes and Rey, 2010).

In the initial solution, the *in-situ* Raman spectra showed a distinct peak of the $v1$ band of the aqueous $(HPO_4^{2-})_{aq}$ molecule at 990 cm^{-1} (Figure 6.3). After onset of $CaCl_2$ titration, the intensity of this band quickly decreased within the first $3-5$ min and a peak at 950 cm^{-1} appeared, indicating the formation of ACP nano-material (compare dark blue line Figure 6.3). In a later stage, after about 150 min a shift of the 950 cm^{-1} band towards the 960 cm^{-1} band occurred, indicating an increase in the degree of order (compare bright blue line Figure 6.3). This is consistent with the formation of the transient phase OCP, as indicated by solution composition. After about 500 min (ca. 8 h) the band has mainly shifted to the 960 cm^{-1} band of HAP, with only a shoulder remaining towards ca. 950 cm^{-1} (compare green line Figure 6.3). Complete transition of ACP to HAP was achieved after ca. 1000 min (ca. 18 h; compare orange line Figure 6.3).

Transformation of ACP into HAP probably via OCP was accompanied by a clear peak sharpening. This sharpening was recorded by a decreased FWHM of the PseudoVoigt function from 26.87 cm^{-1} in the amorphous phase after 10 minutes (Figure 6.4, inlet A) to 16.76 cm^{-1} in the crystalline state (Figure 6.4, inlet C).
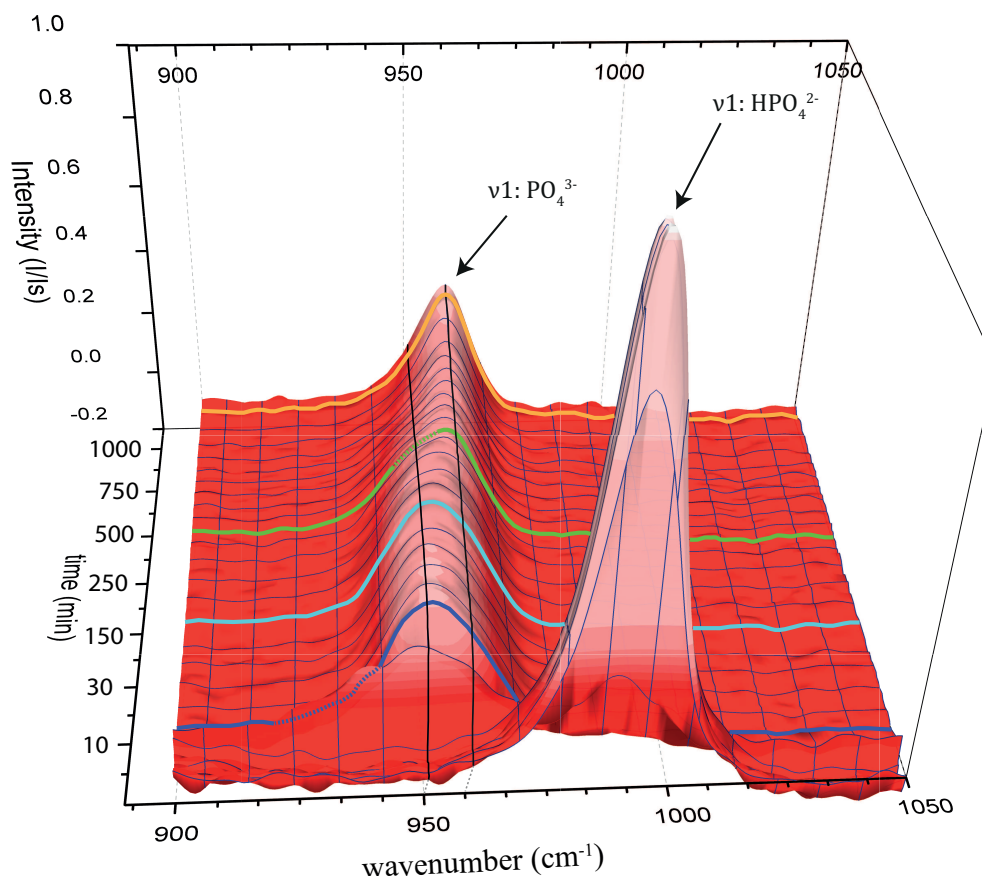
FIGURE 6.3: The first sharp peak is produced by the $v1$ symmetric stretching of the aqueous HPO_4^{2-} molecule of the Na_2HPO_4 solution. Titration of $CaCl_2$ immediately induces precipitation of ACP (dark blue line), completely consuming all aqueous HPO_4^{2-}. Transformation of ACP into OCP begins after ca. 150 min (bright blue line) and to HAP after ca. 500 min (ca. 8 h; green line) with complete transition achieved after ca. 1000 min (ca. 18h; orange line) indicated by a clear peak sharpening.

Time-resolved XRD patterns of the collected solids are displayed in Figure 6.5. The presence of ACP in the reactive solution shortly after $CaCl_2$ titration (10 min) is confirmed by XRD patterns (Figure 6.5). Comparison of the time integrated samples clearly shows the increasing crystallinity and thus the degree of ordering in the solid samples. After 10 min, the XRD pattern shows a very broad peak at ca. $36°2\theta$, while after 405 minutes (6.7 h) crystalline material, enough for detection, can be observed. After 24 h, the XRD pattern indicates distinct peaks, coherent with crystalline HAP.

6.4 Summary and Concluding Remarks

Previous experimental studies on HAP formation suggested that in aqueous alkaline media, OCP occurs as an intermediate phase during the transformation of ACP to
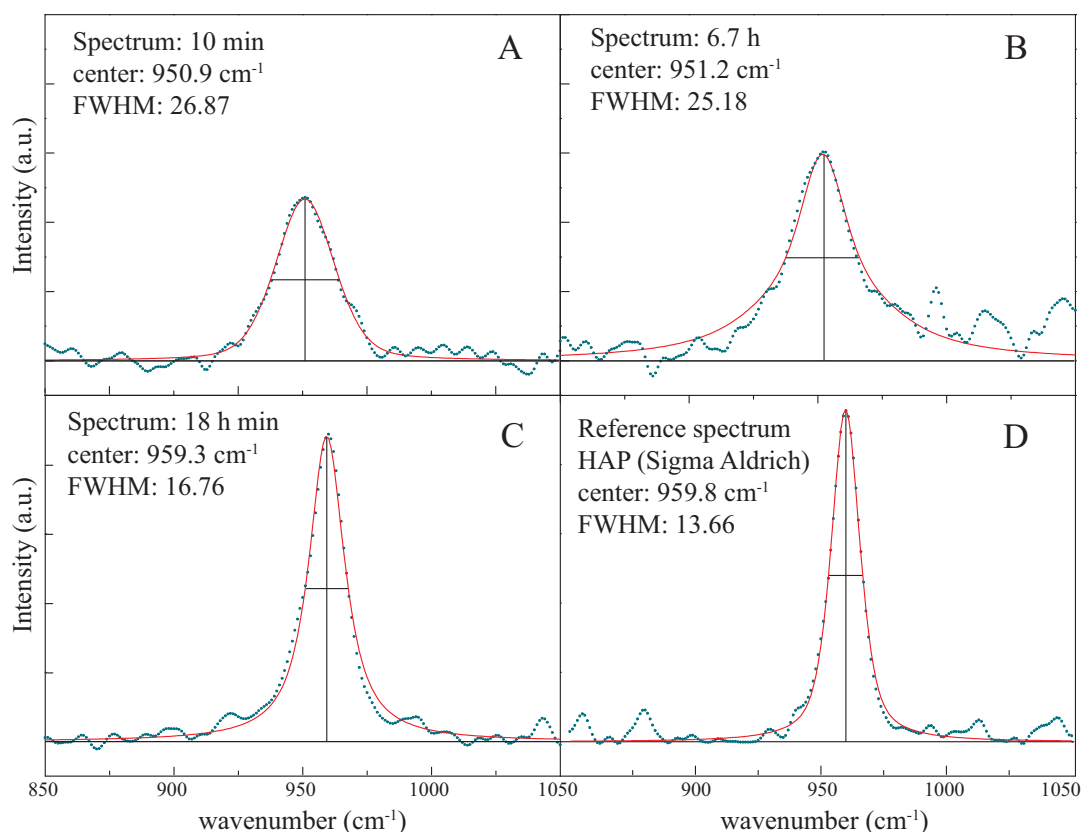
FIGURE 6.4: The transformation process of ACP to HAP (via OCP) is accompanied by a clear peak sharpening recorded in a decreasing FWHM (inlet A – C). The Reference spectra of well-crystallized HAP (Sigma Aldrich) shows a well defined sharp peak highlighted by the lowest FWHM (Inlet D).

HAP (Young and Brown, 1982). In this context, it has been shown that OCP precipitates rapidly by hydrolysis of ACP, forming a layered structure comprising an apatite and hydroxide layer. In an autocatalytic reaction, OCP then slowly transforms to HAP (Young and Brown, 1982). In the present study, *in-situ* RS was successfully applied to detect the transformation of ACP to HAP via an OCP intermediate at a high time-resolution of Raman spectra of 35 seconds. This transformation from amorphous (ACP) to nano-material (OCP) towards crystalline material (HAP) is accompanied by (1) an increased degree of ordering (Figure 6.5), along with (2) an increase of the molar Ca/P ratio of the precipitating solids (Figure 6.2) and (3) a clear peak sharpening of the $v1$ Raman band (Figure 6.4). *In-situ* Raman spectroscopy facilitates the visualization of this increase in crystallinity and ordering, i.e., lattice ordering, in nearly real time. *In-situ* Raman spectroscopy thus facilitates the (near) continuous monitoring of experimental solutions at high temporal resolution and has a clear advantage over manual sampling. Individually extracted samples can thus only offer 'snap-shots' of a dynamic temporal evolution. The outlier sample after 18 h further highlights the sensitivity of sample results due to small sampling biases. This is especially important when working with meta-stable materials, underlining
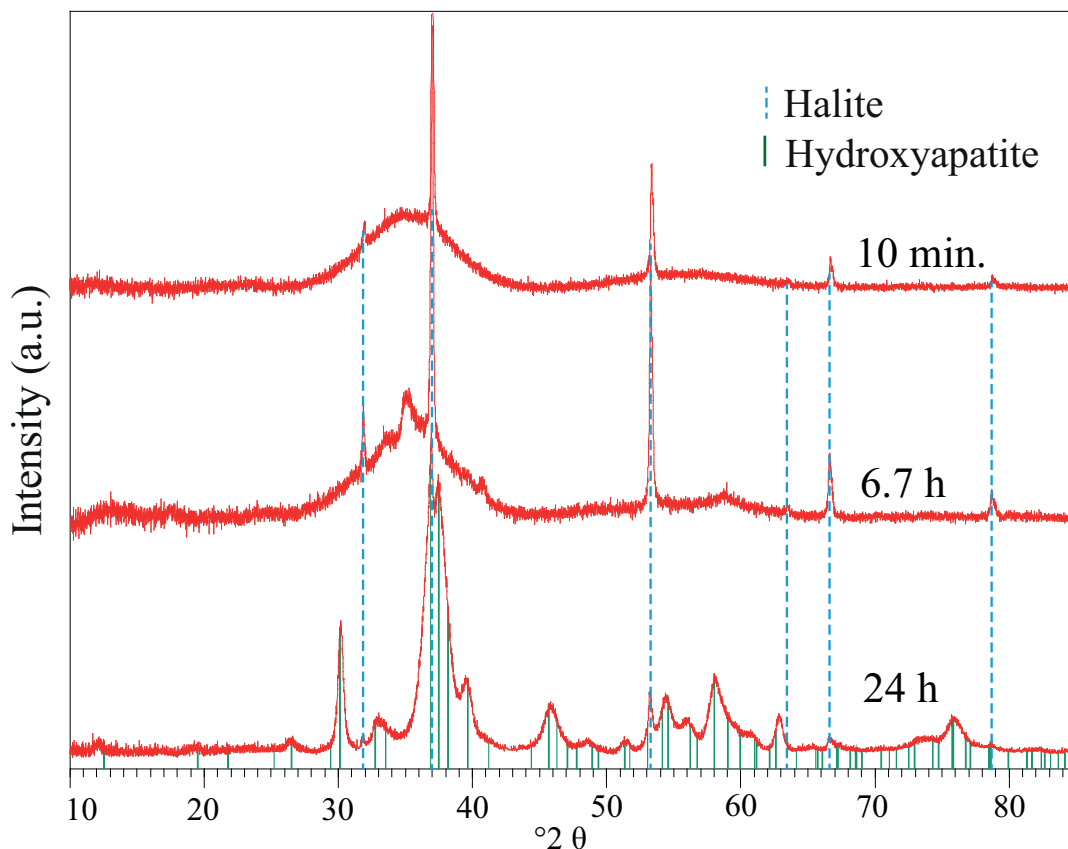
FIGURE 6.5: Time-resolced, stacked XRD patterns confirm the amorphous state after 10 minutes and record the progressive crystallization as a function of time, indicated by development of distinct peaks. Halite ($NaCl$) co-precipitates as an artifact of the chosen method.

the necessity of *in-situ* Raman spectroscopy. The given protocol can be used in both, industrial applications as e.g., a quality screening tool, or for research applications such as *in-situ* reaction monitoring in aqueous media to follow and assess transformation processes, phase identification or crystallinity.

Acknowledgments

References

Arning, E. T., a. Lückge, C. Breuer, N. Gussone, D. Birgel, and J. Peckmann (2009). "Genesis of phosphorite crusts off Peru". In: *Marine Geology* 262. DOI: `10.1016/j.margeo.2009.03.006`.

Bellier, N., F. Chazarenc, and Y. Comeau (2006). "Phosphorus removal from wastewater by mineral apatite". In: *Water Research* 40. DOI: `10.1016/j.watres.2006.05.016`.

Beniash, E., R. A. Metzler, R. S. Lam, and P. Gilbert (2009). "Transient amorphous calcium phosphate in forming enamel". In: *Journal of Structural Biology* 166. DOI: `10.1016/j.jsb.2009.02.001`.

Christoffersen, J., M. R. Christoffersen, W. Kibalczyc, and F. A. Andersen (1989). "A contribution to the understanding of the formation of calcium phosphates". In: *Journal of Crystal Growth* 94. DOI: `10.1016/0022-0248(89)90102-4`.

Combes, C. and C. Rey (2010). "Amorphous calcium phosphates: Synthesis, properties and uses in biomaterials". In: *Acta Biomaterialia* 6. DOI: `10.1016/j.actbio.2010.02.017`.

Cosmidis, J., K. Benzerara, F. Guyot, F. Skouri-Panet, E. Duprat, C. Férard, J.-M. Guigner, F. Babonneau, and C. Coelho (2015). "Calcium-Phosphate Biomineralization Induced by Alkaline Phosphatase Activity in Escherichia coli: Localization, Kinetics, and Potential Signatures in the Fossil Record". In: *Frontiers in Earth Science* 3. DOI: `10.3389/feart.2015.00084`.

Dorozhkin, S. V. (2011). "Calcium orthophosphates: occurrence, properties, biomineralization, pathological calcification and biomimetic applications." In: *Biomatter* 1. DOI: `10.4161/biom.18790`.

Eanes, E. (2001). "Amorphous Calcium Phosphate". In: *Octacalcium Phosphate*. Ed. by L. C. Chow and E. D. Eanes. Vol. 18. Basel: KARGER, pp. 130–147. DOI: `10.1159/000061652`.

Geisler, T., C. Perdikouri, A. Kasioptas, and M. Dietzel (2012). "Real-time monitoring of the overall exchange of oxygen isotopes between aqueous and H2O by Raman spectroscopy". In: *Geochimica et Cosmochimica Acta* 90. DOI: `10.1016/j.gca.2012.04.058`.

Gonzales, F. and M. J. Karnovsky (1961). "Electron microscopy of osteoclasts in healing fracturees of rat bone." In: *The Journal of biophysical and biochemical cytology* 9. DOI: `10.1083/jcb.9.2.299`.

Johnsson, M. S.-A. and G. H. Nancollas (1992). "The Role of Brushite and Octacalcium Phosphate in Apatite Formation". In: *Critical Reviews in Oral Biology & Medicine* 3. DOI: `10.1177/10454411920030010601`.

Kibalczyc, W., J. Christoffersen, M. Christoffersen, a. Zielenkiewicz, and W. Zielenkiewicz (1990). "The effect of magnesium ions on the precipitation of calcium phosphates". In: *Journal of Crystal Growth* 106. DOI: `10.1016/0022-0248(90)90080-5`.

Kim, S., H.-S. Ryu, H. Shin, H. S. Jung, and K. S. Hong (2005). "In situ observation of hydroxyapatite nanocrystal formation from amorphous calcium phosphate in calcium-rich solutions". In: *Materials Chemistry and Physics* 91. DOI: 10.1016/j.matchemphys.2004.12.016.

LeGeros, R. Z., C. B. Bleiwas, M. Retino, R. Rohanizadeh, and J. P. LeGeros (1999). "Zinc effect on the in vitro formation of calcium phosphates: relevance to clinical inhibition of calculus formation." In: *American journal of dentistry* 12.

LeGeros, R. Z. (1993). "Biodegradation and bioresorption of calcium phosphate ceramics". In: *Clinical Materials* 14. DOI: 10.1016/0267-6605(93)90049-D.

LeGeros, R. Z., D. Mijares, J. Park, X.-F. Chang, I. Khairoun, R. Kijkowska, R. Dias, and J. P. LeGeros (2005). "Amorphous Calcium Phosphates (ACP): Formation and Stability". In: *Key Engineering Materials* 284-286. DOI: 10.4028/www.scientific.net/KEM.284-286.7.

LeGeros, R. Z. (1981). "Apatites in biological systems". In: *Progress In Crystal Growth And Characterization* 4. DOI: 10.1016/0146-3535(81)90046-0.

Legeros, R. (1988). "Calcium Phosphate Materials in Restorative Dentistry: a Review". In: *Advances in Dental Research* 2. DOI: 10.1177/08959374880020011101.

Lundager Madsen, H. E. and F. Christensson (1991). "Precipitation of calcium phosphate at 40° C from neutral solution". In: *Journal of Crystal Growth* 114. DOI: 10.1016/0022-0248(91)90407-V.

Mahamid, J., A. Sharir, L. Addadi, and S. Weiner (2008). "Amorphous calcium phosphate is a major component of the forming fin bones of zebrafish: Indications for an amorphous precursor phase." In: *Proceedings of the National Academy of Sciences of the United States of America* 105. DOI: 10.1073/pnas.0803354105. arXiv: arXiv:1408.1149.

Molle, P., A. Liénard, A. Grasmick, A. Iwema, and A. Kabbabi (2005). "Apatite as an interesting seed to remove phosphorus from wastewater in constructed wetlands". In: *Water Science and Technology* 51. DOI: 10.2166/wst.2005.0318.

Montes-Hernandez, G. and F. Renard (2016). "Time-Resolved in Situ Raman Spectroscopy of the Nucleation and Growth of Siderite, Magnesite, and Calcite and Their Precursors". In: *Crystal Growth and Design* 16. DOI: 10.1021/acs.cgd.6b01406.

Nasdala, L., J. Götze, J. Hanchar, M. Gaft, and M. R. Krbetschek (2004). "Luminescence techniques in Earth Sciences 1". In: *EMU Notes in Mineralogy* 6.

Omelon, S. J., M. Ariganello, E. Bonucci, M. Grynpas, and A. Nanci (2013). "A Review of Phosphate Mineral Nucleation in Biology and Geobiology". In: *Calcified Tissue International* 93. DOI: 10.1007/s00223-013-9784-9.

Omelon, S. J. and M. D. Grynpas (2008). "Relationships between Polyphosphate Chemistry, Biochemistry and Apatite Biomineralization". In: *Chemical Reviews* 108. DOI: 10.1021/cr0782527.

Purgstaller, B., M. Dietzel, A. Baldermann, and V. Mavromatis (2017). "Control of temperature and aqueous Mg 2+ /Ca 2+ ratio on the (trans-)formation of ikaite". In: *Geochimica et Cosmochimica Acta* 217. DOI: 10.1016/j.gca.2017.08.016.

Purgstaller, B., V. Mavromatis, A. Immenhauser, and M. Dietzel (2016). "Transformation of Mg-bearing amorphous calcium carbonate to Mg-calcite - In situ monitoring". In: *Geochimica et Cosmochimica Acta* 174. DOI: 10.1016/j.gca.2015.10.030.

Schulz, H. N. and H. D. Schulz (2005). "Large sulfur bacteria and the formation of phosphorite." In: *Science (New York, N.Y.)* 307. DOI: 10.1126/science.1103096.

Termine, J., R. Peckauskas, and A. Posner (1970). "Calcium phosphate formation in vitro". In: *Archives of Biochemistry and Biophysics* 140. DOI: 10.1016/0003-9861(70)90072-X.

Wojdyr, M. (2010). "Fityk : a general-purpose peak fitting program". In: *Journal of Applied Crystallography* 43. DOI: 10.1107/S0021889810030499.

Young, R. A. and W. E. Brown (1982). "Structures of Biological Minerals". In: *Biological Mineralization and Demineralization.* Berlin, Heidelberg: Springer Berlin Heidelberg, pp. 101–141. DOI: 10.1007/978-3-642-68574-3_6.

Zoltek, J. (1974). "Phosphorus Removal by Orthophosphate Nucleation". In: *Journal (Water Pollution Control Federation)* 46. DOI: 10.2307/25038300.

Chapter 7

Conclusions and Perspective

7.1 Conclusions

The current study comprises a set of geochemical and isotopic data of Kazakh sedimentary samples that constrain the paleo-environmental conditions during the Pc-C transition. These results link the ecosphere changes of the Pc-C transition to weathering-related processes. It thus expands our knowledge of this critical time in Earth's history.

Trace and REE, stable oxygen and carbon isotopes, together with petrographic investigation point to a shallow marine depositional environment at the continental margin of the Kazakh microcontinent. Generally low Mn/Sr, ΣREE and a linear co-variation of δ^{13}C and δ^{18}O in these suggest limited interaction with meteoric waters during sediment lithification. On the basis of these geochemical and micro-structural features, the investigated samples can be regarded as near-primary (chapter 3). Leaching experiments demonstrated that contribution from post-sedimentary calcite veins is within the lab's measurement reproducibility of 100 ppm (compare chapter 2 for analytic details and uncertainties). These sedimentary sequences can thus be employed as a seawater archive.

The investigated shallow water deposits record a negative δ^{13}C$_{carb}$ excursion. This can be correlated to the globally occurring basal Cambrian negative carbon isotope excursion (BACE), connecting paleo-Kazakhstan to the global ocean evolution.

Analysis of stable Mg and radiogenic Sr reveals distinctly high values at the Pc-C transition at 541 Ma. Comparison with literature data show that distinctly high Sr isotope values can also be observed at other paleo-microcontinents, including Namibia, China, Siberia and Mongolia. Construction of a new, refined global ^{87}Sr/^{86}Sr seawater evolution, including data from this study and literature data sets, highlights a sudden, positive excursion at the Pc-C boundary at 541 Ma.

Reconstruction of seawater Sr and Mg using the time dependent dynamic-state model (chapter 4) reveals the strong contribution of continental silicate weathering as a major cause for high seawater Sr and Mg values leading up to the Pc-C transition.

These high values are shortly after counterbalanced by hydrothermal activity, causing the observed decrease in both seawater Mg and Sr in the early Cambrian.

The sharp excursion in seawater $^{87}Sr/^{86}Sr$ together with high $\delta^{26}Mg$ at the Pc-C transition, marks a single, critical event in mountain building during the assembly of the Gondwana super-continent. Such an event would cause intense crustal reworking, contributing high $^{87}Sr/^{86}Sr$ and $\delta^{26}Mg$ to the oceans. However, a direct link to atmospheric oxygenation could not be established. It seems however feasible, that oxygen values were already elevated in the Late Neoproterozoic, thus intensifying weathering processes (compare chapter 3). Roberts (2012) has shown a negative excursion of global Hf isotopes during the Gondwana assembly, also indicating such an unprecedented collisional event. The current study thus shows that Mg and Sr isotopes in the marine sedimentary record may be used to identify times of increased continental reworking in Earth's history, similar to Hf isotopes. The associated transport of nutrients to shallow marine environments and the development of large epi-continental shelf areas both facilitated the occurrence of massive phosphorite deposits. This is supported by the experimental studies (chapter 6 and appendix D) in which Ca-phosphates readily form in the presence of elevated Ca and P, producing a variety of shapes and minerals. This can either occur during abiotic mineral formation or within bio-film mimicking polymer gels, resembling biogenic mineral formation. Further, these advances in nutrient cycling aid the sudden developments in marine biota at the Pc-C transition. Overall, this study expands our knowledge about the events at the Pc-C transition, plausibly linking geodynamic events to the ecosphere revolution.

7.2   Perspective

This study has has shown that the Kazakh paleo-microcontinent was part of the global ocean evolution. In contrast to the Chinese paleo-microcontinents, isotope data from Kazakhstan is still sparse. Kazakhstan thus constitutes a key location for future geochemical investigation. The results of this study suggest an extensive, critical orogenic event as a major contributor to the Pc-C ecosphere revolution. Although such an event is certainly plausible during the Gondwana supercontinent assembly, current orogenic reconstructions lack temporal resolution. It could thus be considered, to increase the current data set by investigating additional sections in Kazakhstan. Additionally, in order to expand the data set and validate the global validity, different locations from the various paleo-microcontinents should be investigated. Another approach could also include re-evaluating $^{87}Sr/^{86}Sr$ data from previous or unpublished studies, as this study has shown that the positive $^{87}Sr/^{86}Sr$ excursion at the Pc-C transition is indeed true.

Although this study suggests an orogenic event as the driving force of the Cambrian ecosphere revolution, respective timing and role of atmospheric oxygenation remains

to be identified. In order to constrain the role of atmospheric oxygenation, investigation of redox sensitive isotopes, such as Fe, Mo or Zn isotopes, could be considered. A subset of samples from the investigated Koksu section has already been analyzed for their Fe, Mo and Zn isotopic composition. The obtained results will be evaluated in light of redox conditions and oxygen availability during the early Cambrian.

Several studies have suggested significant seawater pH variation in Earth's history (Mackenzie and Andersson, 2013; Royer et al., 2004). These are often associated with periods of intense weathering and related perturbations to the carbon cycle, a.g. during the post-glacial Late Neoproterozoic (e.g. Ohnemüller, 2014; Kasemann et al., 2010). As the Pc-C transition is also associated with an extensive global weathering event, investigating the seawater pH during the early Cambrian could significantly contribute to our understanding of the Pc-C geodynamic events. Seawater pH can be reconstructed using non-traditional stable B isotopes in combination with stable carbon isotopes (Foster, Pogge von Strandmann, and Rae, 2010; Sanyal et al., 1995; Hönisch and Hemming, 2004; Honisch et al., 2009). In recent years, application of B isotopes has developed as a new and convenient tool in reconstructing paleo-seawater (Marschall and Foster, 2017).

The experimental studies showed that in aqueous media crystallization occurs via a meta-stable transient phase over a relatively long time period of ca. 18 hours. During precipitation within the polymer gel such a transient phase was not observed. In this study, the experimental design did not allow time-dependent sampling of the precipitating mineral without disrupting the process. However, such a meta-stable transient phase can occur during both authigenic and biogenic mineral formation. It could thus be interesting to monitor *in-situ* the precipitation within these polymer gels. A similarly (relatively) long transformation time during biogenic fomation as observed during abiotic precipitation could have implications on the preservation of sensitive materials, such as e.g. embryo fossils (Yin and Zhu, 2012; Li, Chen, and Hua, 1998). A systematic investigation of the stability time under varying conditions might unravel the formation and possible preservation of such fossilized embryos. For such a study, both presented experimental set-up could be combined to facilitate non-invasive *in-situ* monitoring using Raman spectroscopy, in order to not disrupt the precipitation process within polymer gels and yet get high time-resolved insights on biogenic mineral formation.

References

Foster, G. L., P. A. E. Pogge von Strandmann, and J. W. B. Rae (2010). "Boron and magnesium isotopic composition of seawater". In: *Geochemistry, Geophysics, Geosystems* 11. DOI: 10.1029/2010GC003201.

Honisch, B., N. G. Hemming, D. E. Archer, M. Siddall, and J. F. McManus (2009). "Atmospheric Carbon Dioxide Concentration Across the Mid-Pleistocene Transition". In: *Science* 324. DOI: 10.1126/science.1171477.

Hönisch, B. and N. G. Hemming (2004). "Ground-truthing the boron isotope-paleo-pH proxy in planktonic foraminifera shells: Partial dissolution and shell size effects". In: *Paleoceanography* 19. DOI: 10.1029/2004PA001026.

Kasemann, S. A., A. R. Prave, A. E. Fallick, C. J. Hawkesworth, and K.-H. Hoffmann (2010). "Neoproterozoic ice ages, boron isotopes, and ocean acidification: Implications for a snowball Earth". In: *Geology* 38. DOI: 10.1130/G30851.1.

Li, C. W., J. Y. Chen, and T. E. Hua (1998). "Precambrian sponges with cellular structures". In: *Science* 279. DOI: 10.1126/science.279.5352.879.

Mackenzie, F. T. and A. J. Andersson (2013). "The Marine Carbon System and Ocean Acidification during Phanerozoic Time". In: *Geochemical Perspectives* 2.

Marschall, H. and G. L. Foster (2017). *Boron isotopes : the fifth element*. Springer, p. 288.

Ohnemüller, F. (2014). "Reconstruction of Ediacaran to early Cambrian Ocean pH and weathering conditions". Doctoral dissertation. Universität Bremen. DOI: [http://]http://nbn-resolving.de/urn:nbn:de:gbv:46-00103948-13.

Roberts, N. M. W. (2012). "Increased loss of continental crust during supercontinent amalgamation". In: *Gondwana Research* 21. DOI: 10.1016/j.gr.2011.08.001.

Royer, D. L., R. A. Berner, I. P. Montañez, N. J. Tabor, and D. J. Beerling (2004). "CO2 as a primary driver of Phanerozoic climate". In: *GSA Today* 14. DOI: 10.1130/1052-5173(2004)014<4:CAAPDO>2.0.CO;2.

Sanyal, A., N. G. Hemming, G. N. Hanson, and W. S. Broecker (1995). "Evidence for a higher pH in the glacial ocean from boron isotopes in foraminifera". In: *Nature* 373. DOI: 10.1038/373234a0.

Yin, Z. and M. Zhu (2012). "New observations of the ornamented Doushantuo embryo fossils from the Ediacaran Weng'an Biota, South China". In: *Bulletin of Geosciences* 87. DOI: 10.3140/bull.geosci.1234.

Appendix A

Publications and Conference Contributions

A.1   Publication as First Author

O. Nebel and **J. A. Stammeier**. "Strontium Isotopes"
Published in book: Encyclopedia of Geochemistry, Springer International Publishing
AG, 2016

A.2   Publication as Co-author

O. Nebel, P. A. Sossi, J. Foden, A. Bénard, P. Brandl, **J. A. Stammeier**, J. Lupton,
R. J. Arculus. „Constraints on Fe isotope variability in ocean floor lavas from Lau
back-arc basin basalts"
Submitted to Geochimica et Cosmochimica Acta in March 2018, under review

A.3   Conference Contributions

First author:

Goldschmidt 2015, Prague, Czech Republic (Poster)
J. A. Stammeier, F. Konrad, D. Hippler, M. Dietzel. "A FTIR and Raman spec-
troscopic study on sedimentary apatites from the PC-C boundary: a case study on
Central and South Asian phosphorites"

Goldschmidt 2015 – Biomineralization workshop, Prague, Czech Republic (Poster)
J. A. Stammeier, D. Hippler, M. Przezdziak, A. Taubert, M. Dietzel. "Tracing the
(trans-) formation of calcium phosphate by structural, elemental and isotope compo-
sition - Experiments and case studies"

MinPet 2015, Leoben, Austria (Poster)
J. A. Stammeier, D. Hippler, M. Dietzel. "REE abundances in Ediacaran to Early
Cambrian phosphate deposits from Central and South Asia by LA-ICPMS"

EGU 2016, Vienna, Austria (Poster)

J. A. Stammeier, D. Hippler, V. Mavromatis, S. Sacher, M. Dietzel. "(Continuous) In-situ observation of the transformation of amorphous calcium phosphate to crystalline hydroxyapatite"

EWCPS 2017, St. Anton, Austria (Poster)

J. A. Stammeier, D. Hippler, O. Nebel, A. Leis, C. Grengg, F. Mittermayr, M. Dietzel. "Unlocking isotopic and elemental archives in marine phosphorites: a case study from the Precambrian-Cambrian boundary"

Goldschmidt 2017, Paris, France (Poster)

J. A. Stammeier, D. Hippler, O. Nebel, A. Leis, M. Dietzel. "Cambrian Phosphorites as an archive of the bio-geochemical evolution during the Cambrian Explosion - a coupled isotope investigation"

Appendix B

Supplementary Material to Chapter 3

TABLE B.1: Main element data of the acid soluble fraction. The abundance of CO_2 within the carbonates and phosphates was estimated from difference.

Sample	Al_2O_3 [wt.%]	CaO [wt.%]	Fe_2O_3 [wt.%]	MgO [wt.%]	Na_2O [wt.%]	P_2O_5 [wt.%]	SiO_2 [wt.%]	SUM [wt.%]	CO_2 [wt.%]
Koksu, Kazaksthan:									
KO 01	0.36	49.6	5.09	4.57	0.59	37.8	0.21	98.2	1.8
KO 02	0.34	46.9	0.26	0.89	0.37	40.4	0.11	89.3	10.7
KO 25	1.22	39.9	0.65	0.38	D.L.	24.4	4.7	71.2	28.8
KO 03	0.30	46.1	1.46	2.37	0.28	37.0	0.03	87.5	12.5
KO 30	0.42	41.1	0.16	6.44	D.L.	37.9	0.30	86.4	
KO 34	1.31	44.0	0.49	0.30	D.L.	52.8	0.60	100	0
KO 04	0.07	30.0	0.21	19.1	0.06	1.50	0.07	51.0	49
KO 05	1.60	41.0	12.9	2.17	1.22	32.2	0.89	92.0	8
KO 06	0.28	48.5	2.48	2.87	0.23	35.2	0.04	89.6	10.4
KO 07	2.04	45.5	10.9	0.71	0.74	34.8	0.39	95.2	4.8
KO 08	0.15	48.5	1.34	0.79	0.34	39.0	0.03	95.2	4.8
KO 09	0.07	37.7	0.09	2.68	0.20	29.2	0.08	90.2	9.8
KO 10	0.06	73.0	0.02	2.34	0.21	28.5	0.08	70.0	30
KO 11	0.04	43.0	0.01	2.98	0.21	35.9	0.03	104.2	
KO 12	0.03	39.1	0.01	5.99	0.18	27.7	0.03	82.2	17.8
KO 13	0.04	42.6	0.02	5.25	0.27	29.7	0.09	73.0	27
KO 14	0.06	47.5	0.10	0.10	0.40	41.1	0.09	78.0	22
KO 15	0.42	47.2	0.16	0.20	0.37	39.8	0.18	89.4	10.6
KO 16	0.40	44.3	0.12	0.16	0.54	40.2	0.38	88.3	11.7
KO 36	9.05	42.2	3.06	2.03	1.04	34.7	0.52	86.1	13.9
KO 42	0.49	46.3	0.41	0.27	0.52	40.6	0.16	92.6	7.4
KO 43	0.71	46.1	0.19	0.18	0.52	41.2	0.01	88.8	11.2
KO 44	0.93	49.2	0.32	0.23	0.56	38.7	0.03	88.9	11.1
KO 45	0.46	46.0	0.17	0.18	0.51	40.7	0.34	90.0	10
KO 46	0.97	47.0	0.36	0.22	0.52	42.2	0.03	88.4	11.6
KO 50	0.61	45.7	0.30	1.01	0.45	33.7	0.03	91.3	8.7
KO 51	0.46	44.3	0.40	0.20	0.54	40.1	0.77	81.8	18.2
KO 52	0.75	48.2	0.59	0.38	0.57	41.6	0.02	86.8	13.2
KO 56	6.33	46.3	5.59	2.73	1.02	29.0	0.56	91.5	8.5
KO 57	0.05	45.7	0.09	0.18	0.47	39.7	0.22	86.4	13.6
KO 58	0.06	49.4	0.10	0.19	0.52	42.5	0.03	92.8	7.2
KO 59	0.06	46.4	0.08	0.18	0.47	40.3	0.05	87.5	12.5
KO 60	0.04	48.2	0.06	0.16	0.39	41.7	0.07	90.6	9.4
KO 62	0.32	46.2	0.24	0.25	0.42	39.7	0.43	87.6	12.4

TABLE B.1: continued

Sample	Al_2O_3 [wt.%]	CaO [wt.%]	Fe_2O_3 [wt.%]	MgO [wt.%]	Na_2O [wt.%]	P_2O_5 [wt.%]	SiO_2 [wt.%]	SUM [wt.%]	CO_2 [wt.%]
China									
NXF 1204	1.56	44.5	0.5	2.22	0.46	33.1	0.04	82.3	17.7
NXF 1202	0.38	26.8	0.6	15.3	0.12	4.06	0.04	47.3	52.7
ZCP 1202	2.16	51.0	0.4	0.28	0.70	47.7	0.10	102.4	
ZCP 1203	2.04	51.0	0.2	0.32	0.70	47.0	0.04	101.3	
ZCP 1217	0.24	28.4	0.26	14.5	0.12	5.94	0.06	49.6	50.4
ZCP 1215	1.53	54.0	1.17	3.28	0.44	36.5	0.05	96.9	3.1

TABLE B.4: Complementary isotope data. ^{87}Sr/^{86}Srof replica measurements are displayed as average, n = number of measurements; (m) = measured, (i) = initial (541 Ma); errors refer to 2*S.E. of all replica measurements or internal precision, respectively. Values in italic are omitted from interpretation (see section 5.1). ^{87}Sr/^{86}Srdata from Kyrshabakty section as reported in Ohnemüller (2014).

Sample	δ^{13}C (‰VPDB)	δ^{18}O (‰VPDB)	^{87}Sr/^{86}Sr$_{(m)}$	±2 S.E.	n	^{87}Sr/^{86}Sr$_{(i)}$	Rb/Sr
Kazakhstan, Koksu:							
KO 01			0.709750	0.000014		0.70972	0.0014
KO 02	-7.1	-10.51	0.709072	0.000074	2	0.70904	0.0017
KO 22			0.711189	0.000003		0.71119	0.0000
KO 25			0.709608	0.000004		0.70952	0.0037
KO 03	-7.5	-7.64	0.708895	0.000014		0.70886	0.0016
KO 30			0.709117	0.000006		0.70905	0.0033
KO 34			0.709561	0.000013		0.70936	0.0092
KO 04	-7.1	-13.81	0.709237	0.000018		0.70920	0.0017
KO 05	-8.6	-13.44	0.709130	0.000012		0.70894	0.0086
KO 06	-10.2	-13.99	0.709216	0.000014		0.70918	0.0015
KO 07	-12.1	-17.29	0.710124	0.000014		0.70981	0.0140
KO 08	-6.3	-9.38	0.708861	0.000026	2	0.70885	0.0005
KO 09	-6.1	-11.85	0.709240	0.000022	2	0.70922	0.0007
KO 10	-7.3	-8.16	0.708724	0.000027	2	0.70872	0.0003
KO 11	-7.0	-8.40	0.708647	0.000057	2	0.70864	0.0001
KO 12	-4.2	-8.49	0.708713	0.000011	2	0.70871	0.0001
KO 13	-5.5	-9.18	0.709000	0.000049	3	0.70900	0.0002
KO 14	-5.5	-9.33	0.708962	0.000012		0.70895	0.0006
KO 15	-7.4	-18.66	0.708845	0.000014		0.70880	0.0019
KO 16	-9.2	-15.13					0.0019
KO 36	-3.2	-18.62					0.0103
KO 42	-7.4	-19.86	0.708983	0.000014		0.70895	0.0015
KO 43	-10.0	-13.62	0.708995	0.000016		0.70895	0.0019
KO 44	-9.6	-14.69	0.709226	0.000012		0.70917	0.0025
KO 45	-12.0	-20.18	0.709032	0.000012		0.70899	0.0018
KO 46	-9.8	-13.11	0.709191	0.000018		0.70913	0.0028
KO 50	-9.8	-14.71	0.709153	0.000012		0.70910	0.0024
KO 51	-1.2	-5.65	0.708957			0.70892	0.0016
KO 52	-8.0	-11.58	0.708804	0.000010		0.70875	0.0025
KO 54			0.709074	0.000014			0.0048
KO 56	-7.7	-12.45	0.709743	0.000037	2	0.70964	0.0005
KO 57			0.709066	0.000038	3	0.70906	0.0006
KO 58			0.708981	0.000044		0.70897	0.0005
KO 59			0.709015	0.000012		0.70900	0.0003
KO 60	-7.0	-12.43	0.709168	0.000024		0.70917	0.0028
KO 62	-7.3	-13.74	0.709016	0.000010		0.70902	0.0183
KO 64	-0.3	-5.45					
KO 65	-0.6	-5.11					
KO 66	-0.2	-5.44					

TABLE B.2: Trace element data of the acid soluble fraction. D.l. = detection limit

Sample	B [ppm]	V [ppm]	Cr [ppm]	Mn [ppm]	Co [ppm]	Ni [ppm]	Cu [ppm]	Zn [ppm]	As [ppm]	Se [ppm]	Rb [ppm]	Sr [ppm]	Mo [ppm]	Cd [ppm]	Ba [ppm]	Tl [ppm]	Pb [ppm]
Koksu, Kazakhstan																	
KO 01	14.7	73.0	3611	3062	10.4	230	145	12.8	8.42	1.79	1.61	1152	27.2	0.12	586	0.11	6.80
KO 02	11.1	22.5	9.61	557	1.49	9.38	5.30	6.23	4.55	1.79	1.52	920	0.81	0.06	237	0.05	5.36
KO 22	<DL	109	134	5989	30.5	42.9	59.4	152	24.3	<DL	<DL	592	<DL	<DL	2311	<DL	196
KO 25	<DL	97.2	51.2	1922	6.00	17.8	145	27.8	21.7	0.70	6.00	1606	<DL	<DL	1714	<DL	98.5
KO 03	11.3	54.0	1206	1167	3.66	64.6	34.6	6.16	3.53	1.22	1.36	852	8.26	0.05	207	0.03	4.22
KO 30	<DL	91.0	25.0	2570	2.00	7.90	7.90	8.00	5.40	2.20	3.00	926	<DL	<DL	291	<DL	12.7
KO 34	<DL	237	89.1	431	1.80	8.30	10.8	13.6	11.0	3.40	12.1	1316	0.95	<DL	408	<DL	23.6
KO 04	2.39	34.0	144	4675	1.35	12.1	9.03	4.25	1.09	0.26	0.17	102	41.1	0.09	13.4	<DL	4.81
KO 05	25.6	193	7669	2475	23.7	337	208	64.4	22.4	3.47	11.1	1297	12.7	0.81	2269	0.11	32.0
KO 06	10.6	46.9	1992	1787	5.86	97.4	185	9.40	5.18	1.44	1.23	836	36.3	0.20	247	0.03	8.35
KO 07	36.7	437	8438	1298	24.4	339	1009	50.2	32.2	4.74	19.3	1384	6.48	0.48	938	0.03	25.5
KO 08	9.87	25.9	1069	504	2.61	52.3	42.0	5.18	2.54	0.96	0.54	1039	0.68	0.06	140	0.02	4.34
KO 09	8.10	34.1	83.5	1065	1.23	8.98	6.27	4.25	1.27	0.36	0.56	775	0.27	0.05	87.0	<DL	4.46
KO 10	5.55	18.4	21.5	304	0.80	9.29	3.97	3.41	0.80	1.21	0.27	855	0.15	0.04	34.7	<DL	5.61
KO 11	9.33	6.26	11.3	674	0.78	6.89	6.67	5.78	0.46	0.18	0.11	916	0.20	0.03	35.5	<DL	2.65
KO 12	8.60	8.88	10.0	1355	0.94	7.93	3.34	9.45	0.38	0.16	0.08	784	0.47	0.05	35.0	<DL	4.75
KO 13	10.8	5.92	15.0	1196	1.33	8.79	3.12	5.60	1.69	0.14	0.20	855	0.58	0.06	55.2	<DL	2.31
KO 14	14.4	5.02	27.5	130	1.17	9.58	7.57	7.41	7.05	0.40	0.76	1206	1.91	0.02	60.8	<DL	9.11
KO 15	29.1	9.68	49.4	448	2.30	11.3	6.24	6.92	6.40	1.90	2.42	1261	2.64	0.06	110	0.03	6.00
KO 16	25.7	7.65	30.2	632	2.04	12.2	4.43	5.98	4.16	1.76	2.27	1197	2.71	0.03	120	0.05	15.9
KO 36	116	242	648	279	19.2	93.5	123	100	189	6.74	39.5	3833	3.49	0.50	611	0.15	56.0
KO 42	20.7	17.0	291	728	2.61	23.8	7.07	7.45	4.65	1.75	2.14	1446	5.69	0.05	137	0.04	15.9
KO 43	19.0	7.54	83.0	487	2.07	16.9	5.65	11.0	6.78	1.63	2.48	1315	14.7	0.12	182	0.21	15.5
KO 44	25.4	7.12	167	636	3.12	31.3	11.7	19.0	10.3	1.73	4.14	1684	4.70	0.25	205	0.21	18.1
KO 45	21.4	7.52	80.1	606	2.15	18.4	6.39	12.0	6.31	1.37	2.52	1434	5.33	0.11	152	0.10	17.2
KO 46	23.3	21.7	188	836	2.46	27.8	10.4	11.6	13.0	1.82	4.04	1421	5.07	0.07	143	0.07	19.9
KO 50	18.6	4.67	275	1054	3.46	30.0	14.0	11.4	7.69	1.91	3.02	1238	1.73	0.14	224	0.13	33.5
KO 51	21.4	16.4	263	469	1.50	23.9	7.00	7.76	5.92	1.69	2.37	1502	4.79	0.02	128	0.02	15.9
KO 52	19.7	9.05	436	899	3.14	35.7	18.7	10.8	10.5	2.12	3.80	1507	18.5	0.08	243	0.13	35.9
KO 56	92.4	213	3587	5644	39.9	223	341	59.0	108	2.30	34.1	7045	0.57	0.27	2003	0.40	313
KO 57	16.5	10.3	32.2	407	1.07	10.1	5.32	9.19	5.08	0.40	0.71	1381	0.67	0.02	96.0	0.01	27.4
KO 58	15.8	9.66	35.8	429	1.13	10.6	13.2	9.90	4.83	0.47	0.84	1380	0.46	0.03	95.2	0.01	22.2
KO 59	12.6	10.5	15.1	372	1.06	9.37	3.92	11.0	4.49	0.37	0.65	1228	0.76	0.03	87.3	0.01	23.4
KO 60	8.73	7.78	9.64	299	1.01	8.67	4.17	5.86	3.33	0.22	0.34	1003	2.56	0.02	82.4	0.01	27.1
KO 62	12.9	23.8	111	293	2.40	15.0	9.46	6.85	15.1	2.11	4.38	1578	2.56	0.05	1352	0.13	65.2
China:																	
NXF 1204	4.55	15.8	21.2	177	3.06	16.1	14.4	15.1	6.74	0.61	2.89	158	0.77	0.12	16.6	0.03	27.9
NXF 1202	26.1	14.3	19.0	307	0.94	8.64	2.93	24.4	1.04	0.93	8.17	1188	0.19	0.02	1184	<DL	2.34
ZCP 1202	9.70	7.84	7.08	17.2	1.00	6.40	2.71	37286	0.56	12.73	6.66	416	0.16	0.24	252	0.02	3.08
ZCP 1203	25.1	17.0	19.8	74.2	2.24	17.5	6.82	91.0	1.52	0.61	17.8	942	0.18	0.34	482	0.02	8.05
ZCP 1217	2.72	6.46	14.0	97.10	0.90	8.60	4.09	48.4	3.79	0.25	0.79	271	0.44	0.05	24.1	<DL	3.57
ZCP 1215	14.2	7.67	10.9	367	0.97	8.83	43.5	5.59	0.92	0.49	5.36	919	0.97	0.01	1231	<DL	2.10

TABLE B.3: Rare earth element data of the acid soluble fraction. n.a. = not available

Sample	La [ppm]	Ce [ppm]	Nd [ppm]	Sm [ppm]	Eu [ppm]	Gd [ppm]	Tb [ppm]	Dy [ppm]	Ho [ppm]	Er [ppm]	Tm [ppm]	Yb [ppm]	Lu [ppm]	Ce/Ce*	MREE/ MREE*	HREE/ HREE*
Koksu, Kazakhstan:																
KO 01	110	140	92.2	18.8	4.34	23.6	3.21	19.0	3.95	10.7	1.24	6.20	0.80	0.62	1.36	1.14
KO 02	94.0	105	76.4	15.5	3.59	19.9	2.75	16.0	3.47	9.28	1.08	5.39	0.71	0.55	1.36	1.09
KO 22	165	321	158	32.2	0.00	32.5	0.0	<DL	<DL	<DL	<DL	0		0.91	2.40	n.a.
KO 25	204	289	142	25.6	4.22	32.7	<DL	23.4	<DL	12.5	<DL	7.18	<DL	0.73	1.46	n.a.
KO 03	72.7	74.0	61.7	12.5	2.91	16.2	2.20	13.3	2.86	7.92	0.91	4.56	0.60	0.50	1.35	1.03
KO 30	100	119	81.4	15.9	3.43	20.3	2.51	15.8	3.17	9.08	0.86	5.27	0.52	0.59	1.40	1.50
KO 34	174	194	134	26.0	5.46	33.1	4.00	25.6	5.08	14.8	1.37	8.80	0.85	0.56	1.40	1.60
KO 04	13.8	9.20	14.7	2.97	0.65	3.20	0.40	2.17	0.44	1.17	0.13	0.67	0.09	0.30	1.41	1.50
KO 05	199	267	185	38.6	9.37	46.0	6.19	35.4	7.08	18.8	2.13	10.9	1.39	0.63	1.40	1.26
KO 06	82.7	96.7	70.5	14.1	3.16	18.0	2.39	14.1	2.99	8.09	0.93	4.65	0.60	0.57	1.39	1.15
KO 07	314	425	283	55.3	12.1	63.5	8.44	47.6	9.51	25.6	2.92	14.7	1.86	0.65	1.39	1.44
KO 08	44.4	46.9	41.4	9.06	2.12	11.8	1.59	9.57	2.05	5.49	0.61	2.92	0.38	0.50	1.37	1.01
KO 09	13.0	12.8	11.3	2.34	0.55	3.00	0.39	2.27	0.48	1.28	0.14	0.64	0.08	0.48	1.42	1.27
KO 10	18.1	14.5	15.2	3.07	0.72	4.23	0.57	3.54	0.82	2.28	0.25	1.22	0.15	0.39	1.32	0.94
KO 11	2.87	2.34	2.41	0.43	0.11	0.53	0.06	0.30	0.07	0.17	0.02	0.07	0.02	0.40	1.54	1.62
KO 12	2.01	1.94	1.76	0.30	0.07	0.36	0.04	0.20	0.04	0.12	0.01	0.06	0.01	0.46	1.58	2.24
KO 13	1.80	1.44	1.53	0.27	0.07	0.32	0.04	0.20	0.04	0.11	0.01	0.06	0.01	0.39	1.49	1.64
KO 14	15.4	12.0	12.5	2.34	0.54	3.03	0.37	2.07	0.45	1.18	0.12	0.52	0.07	0.38	1.48	1.72
KO 15	72.9	59.4	59.9	12.0	2.93	17.0	2.28	14.4	3.28	9.15	1.01	4.84	0.62	0.40	1.33	0.94
KO 16	67.6	62.7	58.7	12.2	2.95	16.7	2.25	13.73	3.04	8.38	0.93	4.52	0.58	0.45	1.36	0.96
KO 36	175	341	256	58.2	13.4	68.6	9.47	53.6	10.3	25.9	2.77	13.3	1.68	0.77	1.41	1.13
KO 42	74.2	63.4	55.8	10.8	2.52	14.5	1.87	11.2	2.46	6.70	0.73	3.56	0.46	0.43	1.41	1.26
KO 43	80.6	68.6	61.1	11.6	2.73	15.4	2.00	11.9	2.60	7.13	0.76	3.74	0.48	0.43	1.40	1.31
KO 44	88.2	73.9	64.6	12.3	2.84	16.1	2.09	12.4	2.69	7.42	0.81	4.07	0.52	0.43	1.40	1.31
KO 45	69.3	56.2	49.4	9.26	2.18	12.46	1.61	9.68	2.14	5.91	0.64	3.18	0.41	0.42	1.40	1.29
KO 46	95.8	83.5	68.9	12.7	2.94	16.8	2.17	13.2	2.84	7.82	0.86	4.26	0.54	0.45	1.40	1.34
KO 50	87.9	92.1	74.7	15.0	3.42	19.1	2.49	14.4	3.00	8.06	0.87	4.35	0.55	0.51	1.43	1.31
KO 51	81.9	76.3	65.6	12.8	2.99	17.0	2.18	12.8	2.76	7.47	0.79	3.81	0.48	0.46	1.43	1.34
KO 52	97.4	100	81.5	16.3	3.74	21.0	2.72	15.8	3.33	8.98	0.98	4.81	0.61	0.50	1.44	1.30
KO 56	142	242	153	31.9	7.29	36.2	4.60	25.5	4.91	13.0	1.39	7.34	0.87	0.76	1.45	1.51
KO 57	20.1	14.8	15.4	2.65	0.59	3.35	0.37	1.93	0.41	1.02	0.08	0.35	0.04	0.37	1.61	3.22
KO 58	23.0	18.3	17.5	3.11	0.70	4.00	0.46	2.50	0.53	1.38	0.13	0.54	0.07	0.40	1.56	2.44
KO 59	19.7	13.9	14.9	2.49	0.56	3.17	0.34	1.75	0.37	0.90	0.07	0.30	0.04	0.36	1.67	3.60
KO 60	10.3	6.50	6.82	1.03	0.23	1.26	0.13	0.63	0.13	0.33	0.03	0.13	0.02	0.33	1.71	4.39
KO 62	56.1	41.2	38.7	7.05	1.57	9.71	1.24	7.47	1.67	4.58	0.48	2.29	0.28	0.38	1.41	1.42
China:																
NXF 1204	11.4	16.6	14.6	3.11	0.71	3.50	0.46	2.49	0.49	1.31	0.15	0.78	0.10	0.61	1.42	1.20
NXF 1202	47.4	94.6	50.1	10.1	2.87	11.8	1.51	8.28	1.53	3.94	0.43	2.10	0.26	0.90	1.50	1.63
ZCP 1202	11.6	20.1	11.1	2.16	0.45	2.31	0.30	1.62	0.28	0.74	0.09	0.46	0.06	0.81	1.47	1.76
ZCP 1203	23.7	41.9	23.9	4.68	1.07	5.10	0.64	3.41	0.62	1.66	0.19	1.03	0.14	0.81	1.49	1.67
ZCP 1217	6.37	10.2	9.07	2.06	0.50	2.54	0.34	1.96	0.40	1.07	0.13	0.64	0.09	0.64	1.41	0.85
ZCP 1215	36.0	73.3	37.8	7.61	2.37	9.30	1.20	6.70	1.28	3.36	0.37	1.87	0.24	0.92	1.50	1.41

TABLE B.4: continued

Sample	$\delta^{13}C$ (‰VPDB)	$\delta^{18}O$ (‰VPDB)	$^{87}Sr/^{86}Sr_{(m)}$	$\pm$2 S.E.	n	$^{87}Sr/^{86}Sr_{(i)}$	Rb/Sr
Kazakhstan, Kyrshabakty:							
KY 3	-0.1	-3.4	0.709461	0.000008		0.70939	
KY 4	-0.7	-4.3	0.709084	0.000052		0.70901	
KY 7	-2.4	-5.0	0.709300	0.000023		0.70923	
KY 9	-2.6	-5.0	0.708292	0.000172		0.70822	
KY 18	-7.9	-9.0	0.713452	0.000019		0.71338	
KY 20	-8.4		0.712040	0.000034		0.71197	
KY 22	-9.5	-11.3	0.712370	0.000009		0.71230	
KY 25	-7.7	-8.8	0.711805	0.000036		0.71173	
KY28	-6.3	-7.7	0.711983	0.000010		0.71191	
KY 33	-7.0	-7.7	0.713641	0.000009		0.71357	
KY 36	-4.6	-4.6	0.713710	0.000026		0.71364	
KY 38	2.7		0.708611	0.000158		0.70854	
KY 41	3.3	-2.3	0.709058	0.000024		0.70899	
KY 43	2.1	-3.5	0.709152	0.000011		0.70908	
KY 45	0.5	-4.1	0.709316	0.000008		0.70925	
KY 48	1.5		0.709172	0.000008		0.70910	
KY 49	-2.2	-5.8	0.709413	0.000010		0.70934	
KY 59	-0.9		0.709160	0.000026		0.70909	
KY 63	0.5	-3.7	0.709205	0.000008		0.70913	
China:							
NXF 12 02	0.6	-9.72	0.710548	0.000012		0.71014	0.0069
NXF 12 04	0.3	-10.69	0.710489	0.000014		0.71034	0.0183
ZCP 12 03	-5.4	-13.46	0.716479	0.000016		0.71606	0.0189
ZCP 12 02	-5.6	-14.13	0.717463	0.000014		0.71740	0.0029
ZCP 12 15	5.1	-5.83	0.711387	0.000016		0.71103	0.0160
ZCP 12 17	5.2	-5.90	0.710763	0.000022		0.71063	0.0058

TABLE B.5: Summary of single microprobe spot analyses of sample KO10 (C.1) and KO13 (C.2). Mineral composition was calculated from averaged contents. CO_3 contents are calculated from stoichiometry and relative to elemental concentrations. Carbonate fluorapatite contains traces of Cl. n.d.= not determined; d.l. = detection limit. D.l. of Sr was ca. 400 ppm. Elements F, P, S, and Cl were not determined in carbonate phases.

KO 10

CFA	F [wt.%]	MgO [wt.%]	P_2O_5 [wt.%]	SrO [wt.%]	SO_3 [wt.%]	CaO [wt.%]	Cl [wt.%]	CO_2 [wt.%]	Total [wt.%]
1	3.68	0.12	37.42	n.d.	0.20	56.99	0.02	4.47	100.75
2	3.10	0.08	37.88	n.d.	0.18	56.81	0.03	4.46	100.72
3	3.41	0.09	38.29	n.d.	0.22	57.09	0.04	4.48	101.62
4	3.56	0.08	37.24	n.d.	0.29	56.43	0.04	4.43	99.98
5	3.06	0.04	36.41	n.d.	0.23	56.51	0.03	4.43	98.92
6	3.92	0.06	37.31	n.d.	0.24	56.51	0.03	4.43	100.21
7	3.60	0.10	37.54	n.d.	0.23	56.39	0.03	4.43	100.21
8	3.56	0.08	37.28	n.d.	0.32	56.50	0.03	4.43	100.12
9	3.09	0.09	37.10	n.d.	0.25	57.40	0.02	4.50	100.64
10	3.02	0.10	37.74	n.d.	0.29	56.58	0.01	4.44	100.43
11	3.62	0.11	36.92	n.d.	0.25	56.74	0.04	4.45	99.99
12	3.43	0.11	37.99	n.d.	0.32	56.14	0.03	4.41	100.42
13	3.35	0.08	36.83	n.d.	0.50	55.14	0.02	4.33	98.29
14	3.24	0.09	36.69	n.d.	0.32	55.52	0.03	4.36	98.35
15	3.50	0.10	36.96	n.d.	0.45	55.06	0.06	4.32	98.37
16	3.39	0.09	36.96	n.d.	0.33	55.83	0.03	4.38	99.03
17	3.04	0.10	38.34	n.d.	0.18	56.86	0.04	4.46	101.23
18	3.73	0.10	38.27	n.d.	0.28	57.20	0.04	4.49	101.93
19	3.03	0.07	37.56	0.26	0.24	56.67	0.04	4.45	100.54
20	3.34	0.12	38.20	0.25	0.31	56.15	0.04	4.41	100.85
21	3.80	0.11	37.31	0.20	0.25	55.90	0.04	4.39	99.76
22	3.08	0.09	38.36	0.30	0.24	56.02	0.04	4.40	100.72
23	3.13	0.10	37.77	0.22	0.27	56.04	0.04	4.40	100.12
24	3.24	0.08	37.40	0.25	0.27	55.18	0.03	4.33	98.89
25	3.49	0.09	38.25	0.24	0.23	56.67	0.04	4.45	101.40
26	2.99	0.13	37.61	0.33	0.25	56.15	0.03	4.41	100.14
27	3.28	0.09	37.67	0.30	0.26	56.14	0.03	4.41	100.26
28	3.51	0.13	37.72	0.23	0.27	55.88	0.04	4.39	100.10
Average	3.36	0.09	37.54	0.26	0.27	56.30	0.03	4.42	100.14

Chemical formular: $(Ca_{4.98}\ Mg_{0.01}Sr_{0.01})_5((PO_4)_{2.62}(SO_4)_{0.02}(CO_3)_{0.36})_3(Cl_{0.005}F_{0.88}(CO_3)_{0.12})$

Table B.5: continued

KO 10

Dolomite	MgO [wt.%]	SrO [wt.%]	CaO [wt.%]	CO_2 [wt.%]	Total [wt.%]
1	18.62	n.d.	34.84	47.67	101.13
2	18.62	n.d.	34.50	47.41	100.53
3	18.65	n.d.	34.49	47.43	100.57
4	17.91	n.d.	35.62	47.51	101.04
5	17.88	n.d.	34.70	46.76	99.34
6	17.36	n.d.	35.62	46.91	99.89
7	18.01	n.d.	34.99	47.13	100.13
8	18.75	n.d.	33.73	46.94	99.42
9	18.90	n.d.	34.28	47.54	100.72
10	17.36	<d.l.	35.61	46.90	99.87
11	18.29	<d.l.	34.69	47.20	100.18
12	17.99	<d.l.	34.73	46.90	99.62
13	18.32	<d.l.	34.62	47.17	100.11
14	14.77	<d.l.	38.18	46.09	99.04
Average	17.96		35.04	47.11	100.11
Chemical formular	$Ca_{1.17}Mg_{0.83}(CO_3)_2$				

Calcite matrix	MgO [wt.%]	SrO [wt.%]	CaO [wt.%]	CO_2 [wt.%]	Total [wt.%]
1	0.64	n.d.	54.90	43.78	99.32
2	0.56	n.d.	56.09	44.63	101.28
3	0.25	n.d.	55.59	43.90	99.74
4	0.23	n.d.	55.34	43.68	99.25
5	0.55	n.d.	55.53	44.18	100.26
6	0.33	n.d.	54.86	43.41	98.60
7	0.65	n.d.	55.65	44.38	100.68
8	0.19	n.d.	55.27	43.58	99.04
9	0.57	n.d.	55.23	43.97	99.77
10	0.54	<d.l.	54.67	43.49	98.70
11	0.76	<d.l.	54.32	43.46	98.54
12	0.59	<d.l.	55.06	43.85	99.50
13	0.45	<d.l.	55.63	44.15	100.23
14	0.26	<d.l.	55.45	43.80	99.51
15	0.23	<d.l.	55.52	43.82	99.57
16	0.41	<d.l.	54.96	43.58	98.95
17	0.20	<d.l.	55.55	43.81	99.56
18	0.23	<d.l.	55.00	43.41	98.64
Average	0.42		55.26	43.83	99.51
Chemical formular	$Ca_{0.99}Mg_{0.01}CO_3$				

TABLE B.5: continued

KO 13

CFA	F [wt.%]	MgO [wt.%]	P$_2$O$_5$ [wt.%]	SrO [wt.%]	SO$_3$ [wt.%]	CaO [wt.%]	Cl [wt.%]	CO$_2$ [wt.%]	Total [wt.%]
1	3.42	n.d.	37.65	n.d.	0.42	56.70	0.02	4.45	100.66
2	3.24	n.d.	37.79	n.d.	0.26	56.15	0.01	4.41	99.97
3	3.45	n.d.	36.96	n.d.	0.41	56.57	0.03	4.44	99.84
4	3.46	n.d.	37.40	n.d.	0.32	56.53	0.03	4.44	100.15
5	3.54	n.d.	37.99	n.d.	0.40	56.57	0.04	4.44	100.90
6	3.76	n.d.	37.26	n.d.	0.31	56.89	0.04	4.46	100.51
7	3.51	n.d.	37.90	n.d.	0.29	56.92	0.03	4.47	101.07
8	3.58	n.d.	36.07	n.d.	0.35	57.02	0.03	4.47	99.42
9	2.87	n.d.	37.26	n.d.	0.49	56.61	0.04	4.44	100.02
10	3.32	n.d.	37.88	n.d.	0.45	56.60	0.03	4.44	100.77
11	3.8	n.d.	37.63	n.d.	0.43	55.97	0.03	4.39	100.03
12	2.98	n.d.	36.62	n.d.	0.45	56.19	0.01	4.41	98.93
13	3.44	n.d.	37.83	n.d.	0.35	55.16	0.03	4.33	99.12
14	3.08	n.d.	38.73	n.d.	0.42	57.19	0.02	4.49	102.13
15	4.10	n.d.	38.98	n.d.	0.36	56.36	0.04	4.42	101.85
16	3.89	n.d.	38.43	n.d.	0.44	54.58	0.03	4.28	99.38
17	3.28	0.00	36.69	n.d.	0.54	56.72	0.02	4.45	99.79
18	3.60	0.00	36.37	n.d.	1.73	55.60	0.04	4.36	99.58
19	3.20	0.00	37.95	n.d.	0.47	56.42	0.05	4.43	100.63
20	3.40	0.00	38.16	0.31	0.50	55.93	0.03	4.39	100.72
21	3.48	0.00	37.72	0.31	0.36	56.22	0.02	4.41	100.50
22	3.68	0.00	37.74	0.25	0.28	55.84	0.04	4.38	100.05
23	3.54	0.00	38.13	0.15	0.59	55.98	0.04	4.39	100.75
24	3.39	0.00	38.25	0.25	0.36	55.31	0.03	4.34	99.93
25	3.10	0.00	37.15	0.23	0.46	56.78	0.02	4.46	100.39
26	2.92	0.00	37.35	0.24	0.48	55.28	0.03	4.34	98.93
27	3.56	0.00	37.56	0.19	0.31	55.59	0.04	4.36	99.51
28	3.50	0.11	38.20	0.24	0.45	56.07	0.03	4.40	100.84
Average	3.43	0.01	37.63	0.24	0.45	56.21	0.03	4.41	100.23

Chemical formular: (Ca$_{4.98}$ Mg$_{0.01}$Sr$_{0.01}$)$_5$((PO$_4$)$_{2.64}$(SO$_4$)$_{0.03}$(CO$_3$)$_{0.33}$)$_3$(Cl$_{0.005}$F$_{0.90}$(CO$_3$)$_{0.10}$)

Dolomite	MgO [wt.%]	SrO [wt.%]	CaO [wt.%]	CO$_2$ [wt.%]	Total [wt.%]
1	20.53	n.d.	31.93	47.48	99.94
2	20.06	n.d.	32.50	47.41	99.97
3	20.10	n.d.	32.13	47.16	99.39
4	18.89	n.d.	34.01	47.32	100.22
5	18.31	n.d.	34.38	46.97	99.66
6	19.85	n.d.	31.79	46.62	98.26
7	20.03	n.d.	31.52	46.61	98.16
8	19.27	n.d.	33.87	47.62	100.76
9	19.91	n.d.	31.89	46.77	98.57
10	19.98	n.d.	31.99	46.92	98.89
11	19.88	<d.l.	32.24	47.01	99.13
12	19.83	<d.l.	32.08	46.83	98.74
13	20.51	<d.l.	31.96	47.48	99.95
14	19.72	<d.l.	32.56	47.09	99.37
Average	19.78		32.49	47.09	99.36

Chemical formular: Ca$_{1.08}$Mg$_{0.92}$(CO$_3$)$_2$

TABLE B.5: continued

KO 13

Calcite	MgO [wt.%]	SrO [wt.%]	CaO [wt.%]	CO_2 [wt.%]	Total [wt.%]
1	0.47	n.d.	55.45	44.03	99.95
2	0.61	n.d.	54.58	43.50	98.69
3	0.51	n.d.	54.40	43.25	98.16
4	0.68	n.d.	54.76	43.72	99.16
5	0.50	n.d.	54.90	43.63	99.03
6	0.43	n.d.	54.75	43.44	98.62
7	0.40	n.d.	55.07	43.65	99.12
8	0.44	n.d.	54.93	43.59	98.96
9	0.51	n.d.	55.41	44.04	99.96
10	0.58	n.d.	55.04	43.83	99.45
11	0.65	<d.l.	54.81	43.72	99.18
12	0.37	<d.l.	54.51	43.18	98.06
13	0.43	<d.l.	54.39	43.15	97.97
14	0.40	<d.l.	56.32	44.64	101.36
15	0.86	<d.l.	54.68	43.85	99.39
16	0.38	<d.l.	54.44	43.14	97.96
17	0.57	<d.l.	54.34	43.27	98.18
18	0.62	<d.l.	54.65	43.57	98.84
Average	0.52	<d.l.	54.60	43.62	99.00

Chemical formular: $Ca_{0.99}Mg_{0.01}CO_3$
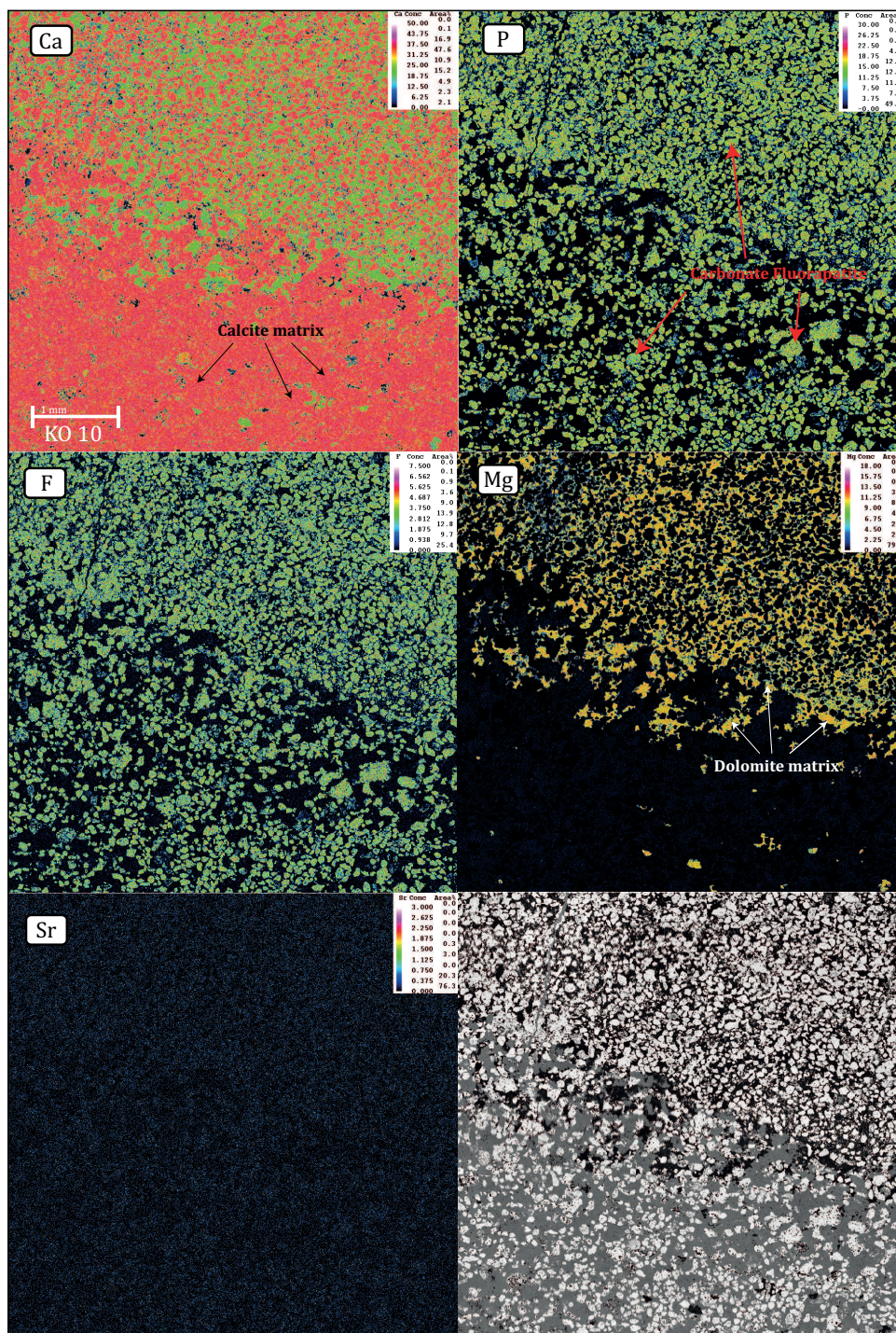
FIGURE B.1: Elemental concentration images of samples KO 10 (C.1) and KO 13 (C.2). Strontium contents are up to 0.26 and 0.24 wt.% within the Carbonate-Fluorapatite (CFA). Image (C.1) displays the transition of a calcite to dolomite matrix in a well-sorted phosgrainstone; image (C.2) depicts a poorly sorted flat pebble phos-rudstones with a dolomite matrix. Single spot analyses of the three major minerals (arrows) were evenly distributed within the samples. CFA has an average molar Ca/P ratio of 2.5 ± 0.1 (n = 56). Dolomite has an average molar Ca/Mg ratio of 2.3 ± 0.2 (KO10, n = 14) and 2.0 ± 0.1 (KO13, n = 14). Note: Samples KO 10 (C.1) and KO 13 (C.2) were also used for leaching experiments to determine ^{87}Sr/^{86}Sr contribution.

FIGURE B.1: continued

References

Ohnemüller, F. (2014). "Reconstruction of Ediacaran to early Cambrian Ocean
    pH and weathering conditions". Doctoral dissertation. Universität Bremen. DOI:
    [http://]http://nbn-resolving.de/urn:nbn:de:gbv:46-00103948-13.

Appendix C

Encyclopedia of Geochemistry: Strontium Isotopes

S

Strontium Isotopes

Oliver Nebel[1] and Jessica A. Stammeier[2]
[1]School of Earth, Atmosphere and Environment, Monash University, Clayton/Melbourne, VIC, Australia
[2]Institute of Applied Geosciences, Graz University of Technology, Graz, Austria

Definition

Strontium (Sr) isotopes are widely applied tracers in geoscientific applications. One of the four stable isotopes (^{87}Sr) is subject to long-term radiogenic ingrowth by radioactive decay of rubidium (^{87}Rb). Resultant isotope variations in ^{87}Sr/^{86}Sr, but also other stable isotope variations, can be employed to trace mixing of global reservoirs, ranging from high-temperature-pressure processes preserved in solid rock to low-temperature, environmental conditions in surface waters, oceans, chemical sediments, or biogeochemistry. A second, frequent application is the dating of rock-forming processes using the Rb-Sr decay scheme, ranging in age from the infant stages of the solar system to most recent geologic events.

Introduction to Rb-Sr Systematics

Rb-Sr systematics are based on the radioactive decay of the isotope ^{87}Rb (that today accounts for ~27% of all rubidium) to ^{87}Sr (~9% of all strontium) by beta decay with a half-life of approximately 49 billion years, corresponding to a Rb decay constant (λ^{87}Rb) of 1.394×10^{-11}/a (Nebel et al., 2011b). A prime application of the decay scheme is tracing geochemical processes using the radiogenic Sr isotope signature in rocks and minerals. As a dating technique Rb-Sr is, in principle, suitable for samples from the early stages of the solar system to a few million years before present. Modern Rb-Sr

geochronology of multiple phases can achieve precisions similar to Ar-Ar dating or conventional U-Pb dating, in the order ca. ±0.2% (Nebel and Mezger, 2008; Willigers et al., 2004). The thermal threshold, or closure temperature T_C, for Rb-Sr reset is between 300°C and 400°C, dependent on mineralogy. This renders Rb-Sr one of the most susceptible systems to thermal overprint among the long-lived lithophile element isotope systems.

Isochron relationships can further be used to test initial isotope equilibrium of phases. For this, in an isochron diagram, isotope equilibrium at t_0 is marked by the ordinate intercept of the regression line (Figure 1) or can be calculated as initial ^{87}Sr/^{86}Sr. The related decay equation is (with t in millions of years):

$$^{87}\text{Sr}/^{86}\text{Sr}_{present} = {}^{87}\text{Sr}/^{86}\text{Sr}_{initial} + {}^{87}\text{Rb}/^{86}\text{Sr} \\ \times \left(e^{\left(\lambda \times t \right)} - 1 \right)$$

Strontium Isotope Analyses

Strontium isotope compositions vary from subtle variations among whole rocks or mineral phases in the 5th decimal place (i.e., 0.00005) to large variations, especially in older samples. The ^{87}Sr/^{86}Sr can be routinely analyzed in > 50 ng Sr of purified sample material by thermal ionization mass spectrometry (TIMS). Precisions are typically ±40 ppm but can be as good as ±5 ppm with modern TIMS instruments. An alternative method is the use of multicollector inductively coupled plasma source mass spectrometry (MC-ICP-MS). This technique allows a high sample throughput and in situ analyses via laser ablation, but yields less precise data no better than ± 100 ppm (Vroon et al., 2008) and is restricted to samples with low Rb/Sr. Collision-cell, triple-quadrupole ICP mass spectrometers, however, can be used for in situ Rb-Sr dating with precisions < 1.5% of the sample age
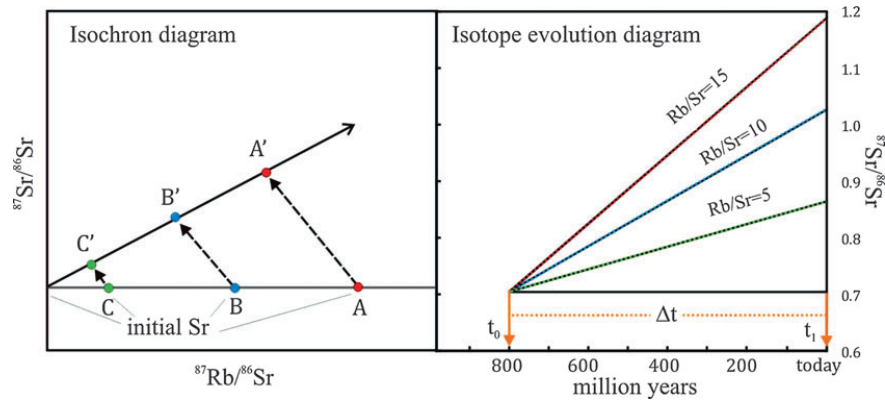
Strontium Isotopes, Figure 1 (**a**) Rb-Sr isochron diagram showing the time-dependent evolution of three different phases, (A-C) with variable Rb/Sr that formed in isotopic equilibrium and thus have the same initial $^{87}Sr/^{86}Sr$ isotope composition. Points A'-C' reflect the present day isotope composition of phases A-C, respectively. (**b**) $^{87}Sr/^{86}Sr$ isotope evolution versus time plot (with t_0 defining the onset of radiogenic ingrowth and t_1 the time of sampling) with the respective ^{87}Sr ingrowth of three different phases as a consequence of their variable Rb/Sr.

(Zack and Hogmalm, 2016). Mass fractionation in the mass spectrometer during isotope analyses is corrected for by using a $^{86}Sr/^{88}Sr = 0.1194$ by convention, or in the case of stable isotope analyses, by correction relative to the NBS-987 isotope standards.

## Radiogenic Sr Isotopes in Early Solar System Material and Bulk Silicate Earth

The initial $^{87}Sr/^{86}Sr$ composition of the solar system ($^{87}Sr/^{86}Sr_{SS}$) is best estimated by analyses of calcium-aluminum-rich inclusions (CAI) in primitive chondrites. These inclusions, composed of predominantly refractory elements, are believed to be the first solids condensed from the solar nebular. Their initial $^{87}Sr/^{86}Sr$ has recently been determined to 0.698975 ± 0.000008 (Hans et al., 2013).

Previous determination of $^{87}Sr/^{86}Sr_{SS}$ also employed initial $^{87}Sr/^{86}Sr$ of achondrites (best achondrite basaltic initial - BABI), including the pyroxene-rich angrite Angra Dos Reis (ADOR). These older analyses revealed $^{87}Sr/^{86}Sr$ isotope heterogeneity among the earliest solar system bodies. However, Hans and co-workers found variations in the stable $^{84}Sr/^{86}Sr$ in these meteorites, which they ascribe to incomplete mixing of r-process nuclides in the solar nebula. Upon correction for these isotope variations in $^{84}Sr/^{86}Sr$ compositions (and thus also affecting $^{87}Sr/^{86}Sr$ prior to radiogenic ingrowth), the resultant $^{87}Sr/^{86}Sr_{SS}$ in angrites is identical to those in CAI. Considering the very similar formation age of angrites, within ca. two million years after CAI formation, this indicates a homogeneous initial $^{87}Sr/^{86}Sr$ of the early solar system.

A key problem in determining the $^{87}Sr/^{86}Sr$ evolution of the bulk silicate Earth (BSE) is that its average Rb/Sr is unknown, and no representative sample is available for analysis. The reason for this is two-fold: One major obstacle is that although the Sr isotope compositions of primitive chondrites can be precisely measured, the Rb/Sr of these terrestrial building blocks are highly variable due to the volatility of Rb (half-condensation temperature of ~800 K). Loss of volatile elements, including Rb, during early solar system body collisions or depletion into the early sun or the outer solar system has likely altered the chondritic Rb/Sr (Nebel et al., 2011a). Using terrestrial Sr-Nd isotope covariations in mantle-derived rocks (Figure 2a) as a substitute yields a Sr isotope composition of $^{87}Sr/^{86}Sr_{CHUR} \sim 0.705$ in a chondritic Earth model (CHUR), or $^{87}Sr/^{86}Sr_{SCHEM} \sim 0.703 \pm 0.004$ in a subchondritic Earth model (SCHEM, (Caro and Bourdon, 2010).

Radiogenic Sr Isotopes in the Crust–Mantle System

Continental crust has formed with time mainly by partial melting of the upper mantle at convergent plate margins or in plumes. During melting processes in the mantle, Rb is less compatible than Sr, which leads to a time-integrated high Rb/Sr in the crust compared to the mantle and a correspondingly high $^{87}Sr/^{86}Sr$ in crustal rocks. A sample or entire terrane separated from the mantle at one point in Earth's history will therefore diverge from the mantle's Sr isotope evolution. However, due to substantial Rb/Sr fractionation during igneous differentiation processes, the continental
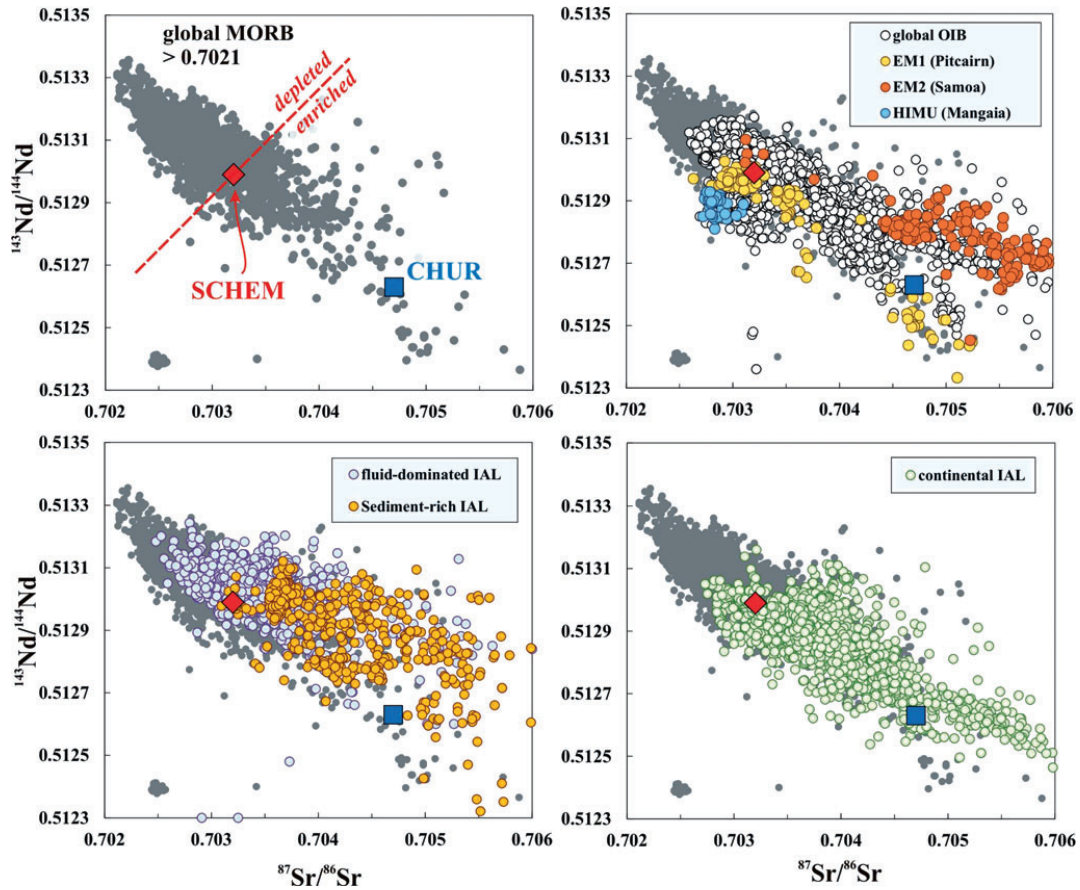
Strontium Isotopes, Figure 2 Comparison of Sr and Nd isotope ratios in global ocean floor lavas following the rational of DePaolo and Wasserburg (1977). (**a**) Mid-ocean ridge basalts (MORB) show a clear co-variation (*gray dots*). In a subchondritic Earth model (SCHEM), 1/3 of al data are isotopically enriched, tending towards the *top-left* corner in the diagram. (**b**) Ocean Island basalts (OIB) with the three isotope end members enriched-mantle 1 and 2 (EM1, EM2) and high-μ (HIMU). (**c, d**) Subduction zone data for global island arc lavas (IAL) in comparison with MORB; MORB and OIB/IAL data taken from www.earthchem.org/petdb and http://georoc.mpch-mainz.gwdg.de, respectively. SCHEM and CHUR values as listed in Caro and Bourdon (2010).

crust is highly heterogeneous in its $^{87}Sr/^{86}Sr$ with an average present day isotope composition of $^{87}Sr/^{86}Sr \sim 0.715$, based on loess samples (e.g., Yokoo et al., 2004).

The present day depleted mantle is also heterogeneous in its Sr isotope composition, owing to melt extraction and re-fertilization by recycled crust. Due to elevated $^{87}Sr/^{86}Sr$ and high Sr abundances in crustal rocks and their sedimentary products, crustal recycling has a strong effect on the Sr isotope composition of mantle rocks with less radiogenic $^{87}Sr/^{86}Sr$ (Armstrong, 1968; DePaolo, 1981). On average, global mid-ocean ridge basalts (MORB), considered representative of the upper mantle, show a depleted Sr isotope signature with the lowest reported present day value of

$^{87}Sr/^{86}Sr = 0.7021$ (Figure 2a). A key difference between the actively discussed chondritic versus subchondritic Earth models is the degree of mantle depletion. About one-third of ocean floor lavas at oceanic ridges is isotopically enriched through crustal components in a SCHEM model, opposing a nearly complete depletion in a CHUR model.

Oceanic island lavas (OIB), considered by most to be sourced by thermo-chemical anomalies from the lower mantle (plumes), also show elevated radiogenic isotope signatures associated with crustal recycling. The common model explains these signatures with a recycling process of subducted, crustal components into the lower mantle and their return to the surface in upwelling plumes (Hofmann and

White, 1982). Even though the calculated amount of crust in these rocks appears small, in the order of $< 5\%$, the radiogenic isotope character of Sr is still sufficiently indicative for the presence of crustal components in the source of these lavas. Mantle-residence times of crustal components vary substantially from < 650 Myrs in some so-called enriched mantle 1 (EM1) components (Sobolev et al., 2011), based on $^{87}Sr/^{86}Sr$ in Hawaiian lavas, to > 2.3 Ga in the most extreme HIMU lavas with remarkably low $^{87}Sr/^{86}Sr$. Samoan OIB show the most extreme Sr isotope values among OIB, which represent the so-called enriched mantle 2 (EM2) component. (Jackson et al., 2007).

The major sites for crust-mantle interaction is and Sr pollution of the mantle occurs at convergent margins, that is, in subduction zones. However, recycling into the mantle is incomplete, evidenced by elevated $^{87}Sr/^{86}Sr$ in most erupting island arc lavas (IAL) when compared to average MORB. The Sr isotope composition in IAL is broadly correlated to the amount of sediment that is being subducted in the subduction zone. Figure 2c shows a plot of arcs associated with large amounts of subducted sediment (Banda and Lesser Antilles arc) with a clear offset from MORB due to partial sediment melting. In contrast, IAL from so-called fluid-dominated arcs (Marianna, Izu-Bonin, Kermadec, and Aleutian) show intermediate signatures, often related to overprint with Sr-bearing fluids. In continental arcs (Figure 2d, Cascades, Central American and Mexican Volcanic arc), crustal assimilation plays an important role, illustrated by lower Sr isotopes for a given Nd isotope signature when compared to intraoceanic arcs.

Stable Sr Isotopes in Geochemistry

Within the current analytical limits of ± 0.02 $\delta^{88}Sr$ units (the delta notation is the deviation in $^{88}Sr/^{86}Sr$ from the NBS-987 standard times 1000), early solar system materials, including Martian rocks, are identical. In contrast, terrestrial rocks show lighter values in relation to igneous differentiation, tentatively linked to plagioclase fractionation and associated substitution of Sr^{2+} for Ca^{2+} with a preference for the heavier isotope (Charlier et al., 2012). In the low temperature environment, stable Sr isotopes show fractionation during weathering of crustal rocks and in associated soils and waters (Stevenson et al., 2016). Experimental work on biological carbonate material suggests a dependence between ambient temperature and $\delta^{88}Sr$ (Fietzke and Eisenhauer, 2006). In marine carbonates sampled throughout the Phanerozoic, however, stable Sr isotope compositions show little or no dependence with temperature. Instead, the variations in $\delta^{88}Sr$, decoupled from $^{87}Sr/^{86}Sr$, can be used to constrain the flux of Sr run-off into the oceans and associated ocean residence times (Vollstaedt et al., 2014).

Radiogenic Sr Isotopes in Surface and Ocean Water

Strontium is a large ion lithophile element (LILE) and therefore considered mobile in aqueous solutions. It has a high solubility and is readily transported in surface waters and hydrothermal fluids. In ground water, dissolution of Sr^{2+} through reaction with aquifer lithology leads to highly variable $^{87}Sr/^{86}Sr$, which can be used to trace water pathways (Jacobson and Wasserburg, 2005). Because of the radiogenic nature of the continental crust, crustal weathering results in radiogenic isotope signatures in most surface waters and open oceans with an average, present day seawater $^{87}Sr/^{86}Sr \sim$ 0.712 (Palmer and Edmond, 1989). Continental run-off of Sr into the ocean is related to continental weathering rates, and the related ocean residence time is in the order of 1 Myr to as long as 20 Myrs in the Phanerozoic Oceans (Vollstaedt et al., 2014). Consequently, enhanced weathering due to erosion of crustal terranes with associated radiogenic $^{87}Sr/^{86}Sr$, for example, during times of peak orogenesis, results in more radiogenic Sr isotope signatures in seawater. Similarly, the contribution of juvenile $^{87}Sr/^{86}Sr$ to the ocean in times of extensive seafloor spreading, for example, during continental reorganization following the break-up of supercontinents, can alter seawater Sr isotopic composition.

Strontium is easily incorporated into Ca-bearing chemical sediments (e.g., carbonates or phosphates) or biogenic carbonate-phosphate skeletons (e.g., shells, corals). Hence, with a detailed knowledge of the $^{87}Sr/^{86}Sr$ signatures of seawater through time, the isotope signatures of Ca-bearing marine sediments, for example carbonates, may be used to place them into a broader stratigraphic context. This process is known as Sr chronostratigraphy. Careful analyses of limestones and/or biogenic calcite with known age revealed a detailed Sr isotope evolution of seawater throughout the Phanerozoic (Burke et al., 1982; Veizer and Compston, 1974). Subsequent refinements of the seawater evolution curve revealed a cyclic evolution with de- and increasing isotope signatures (Figure 3). Notable is a constant decline in average Sr isotope composition from the Cambrian to the late Jurassic. A steady increase since then has led to a present day $^{87}Sr/^{86}Sr = 0.7092$, broadly matching Cambrian seawater isotope composition.

Sr Isotopes in Forensic Sciences

Strontium readily substitutes for Ca^{2+} in biogenic phosphates and with this also locks in the $^{87}Sr/^{86}Sr$ isotope code of the environment in which the organism grows. With this, Sr isotope compositions of bones and teeth are a valuable tracer in forensic sciences for provenances studies or to track migration routes. Application range in identifying historic human

Strontium Isotopes,
Figure 3 Strontium isotope evolution of Phanerozoic seawater after Veizer et al., (1999). Filled symbols represent coherent data reported in Veizer et al., (1999); open symbols are additional literature data. The *orange line* is a moving average drawn by eye to highlight the sharp changes in $^{87}Sr/^{86}Sr$. Data compilation courtesy by Jan Veizer, accessible via http://mysite.science.uottawa.ca/jveizer/isotope_data/.
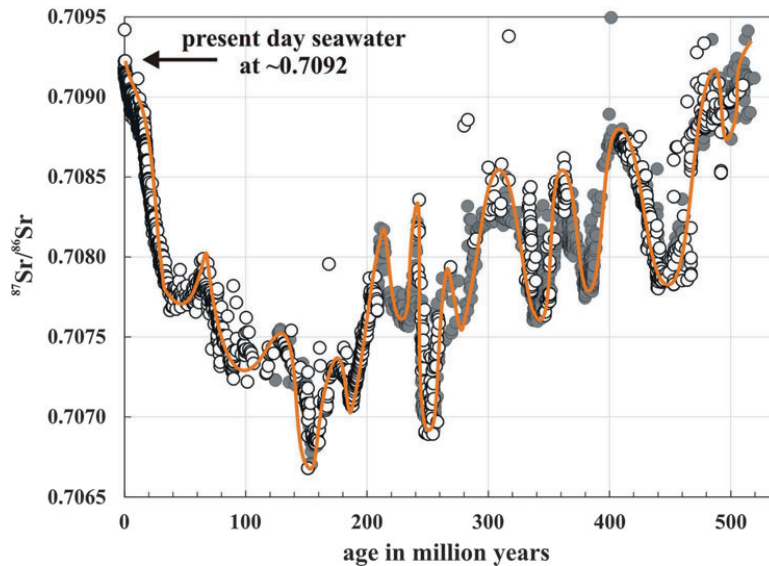
remains and their provenance using teeth, for example, the iceman discovered in Austria (Muller et al., 2003), or tracking human or bird migration through hair or feather analyses, respectively (Font et al., 2007; Font et al., 2012). Analyses in human bone, however, reflect only the last ca. 6 years of life (Price et al., 2000).

Cross-References

▶ Archeological Geochemistry
▶ Earth's Continental Crust
▶ Earth's Mantle
▶ Earth's Formation and Geochemical Evolution
▶ Inductively Coupled Plasma Mass Spectrometry
▶ Marine Geochemistry
▶ Mid-ocean Ridge Basalts
▶ Neodymium Isotopes
▶ Oceanic Island Basalts
▶ Rubidium
▶ Stable Isotope Geochemistry
▶ Strontium
▶ Thermal Ionization Mass Spectrometry

References

Armstrong, R. L., 1968. A model for the evolution of strontium and lead isotopes in a dynamic Earth. *Reviews of Geophysics*, **6**, 175–199.
Burke, W. H., et al., 1982. Variation of seawater $^{87}Sr/^{86}Sr$ through Phanerozoic time. *Geology*, **10**(10), 516–519.

Caro, G., and Bourdon, B., 2010. Non-chondritic Sm/Nd ratio in the terrestrial planets: Consequences for the geochemical evolution of the mantle crust system. *Geochimica et Cosmochimica Acta*, **74**(11), 3333–3349.
Charlier, B. L. A., et al., 2012. High temperature strontium stable isotope behaviour in the early solar system and planetary bodies. *Earth and Planetary Science Letters*, **329**, 31–40.
DePaolo, D. J., 1981. Trace element and isotopic effects of combined wall rock assimilation and fractional crystallization. *Earth and Planetary Science Letters*, **53**, 189–202.
DePaolo, D. J., and Wasserburg, G. J., 1977. Sources of island arcs as indicated by Nd and Sr isotopic studies. *Geophysical Research Letters*, **4**(10), 465–468.
Fietzke, J., and Eisenhauer, A., 2006. Determination of temperature-dependent stable strontium isotope (Sr-88/Sr-86) fractionation via bracketing standard MC-ICP-MS. *Geochemistry, Geophysics, Geosystems*, **7**.
Font, L., Nowell, G. M., Pearson, D. G., Ottley, C. J., and Willis, S. G., 2007. Sr isotope analysis of bird feathers by TIMS: a tool to trace bird migration paths and breeding sites. *Journal of Analytical Atomic Spectrometry*, **22**(5), 513–522.
Font, L., et al., 2012. Strontium and lead isotope ratios in human hair: investigating a potential tool for determining recent human geographical movements. *Journal of Analytical Atomic Spectrometry*, **27**(5), 719–732.
Hans, U., Kleine, T., and Bourdon, B., 2013. Rb-Sr chronology of volatile depletion in differentiated protoplanets: BABI, ADOR and ALL revisited. *Earth and Planetary Science Letters*, **374**, 204–214.
Hofmann, A. W., and White, W. M., 1982. Mantle plumes from ancient oceanic crust. *Earth and Planetary Science Letters*, **57**, 421–436.
Jackson, M. G., et al., 2007. The return of subducted continental crust in Samoan lavas. *Nature*, **448**(7154), 684–687.
Jacobson, A. D., and Wasserburg, G. J., 2005. Anhydrite and the Sr isotope evolution of groundwater in a carbonate aquifer. *Chemical Geology*, **214**(3-4), 331–350.
Muller, W., Fricke, H., Halliday, A. N., McCulloch, M. T., and Wartho, J. A., 2003. Origin and migration of the Alpine Iceman. *Science*, **302**(5646), 862–866.

Nebel, O., and Mezger, K., 2008. Timing of thermal stabilization of the Zimbabwe Craton deduced from high-precision Rb-Sr chronology, Great Dyke. *Precambrian Research*, **164**(3-4), 227–232.

Nebel, O., Mezger, K., and van Westrenen, W., 2011a. Rubidium isotopes in primitive chondrites: Constraints on Earth's volatile element depletion and lead isotope evolution. *Earth and Planetary Science Letters*, **305**(3-4), 309–316.

Nebel, O., Scherer, E. E., and Mezger, K., 2011b. Evaluation of the Rb-87 decay constant by age comparison against the U-Pb system. *Earth and Planetary Science Letters*, **301**(1-2), 1–8.

Palmer, M. R., and Edmond, J. M., 1989. The strontium isotope budget of the modern ocean. *Earth and Planetary Science Letters*, **92**, 11–26.

Price, T. D., Manzanilla, L., and Middleton, W. D., 2000. Immigration and the ancient city of Teotihuacan in Mexico: a study using strontium isotope ratios in human bone and teeth. *Journal of Archaeological Science*, **27**(10), 903–913.

Sobolev, A. V., Hofmann, A. W., Jochum, K. P., Kuzmin, D. V., and Stoll, B., 2011. A young source for the Hawaiian plume. *Nature*, **476**(7361), 434–437.

Stevenson, E. I., et al., 2016. Insights into combined radiogenic and stable strontium isotopes as tracers for weathering processes in subglacial environments. *Chemical Geology*, **429**, 33–43.

Veizer, J., and Compston, W., 1974. ^{87}Sr/^{86}Sr composition of seawater during the Phanerozoic. *Geochimica et Cosmochimica Acta*, **38**(9), 1461–1484.

Veizer, J., et al., 1999. Sr-87/Sr-86, delta C-13 and delta O-18 evolution of Phanerozoic seawater. *Chemical Geology*, **161**(1-3), 59–88.

Vollstaedt, H., et al., 2014. The Phanerozoic delta Sr-88/86 record of seawater: new constraints on past changes in oceanic carbonate fluxes. *Geochimica Et Cosmochimica Acta*, **128**, 249–265.

Vroon, P. Z., van der Wagt, B., Koornneef, J. M., and Davies, G. R., 2008. Problems in obtaining precise and accurate Sr isotope analysis from geological materials using laser ablation MC-ICPMS. *Analytical and Bioanalytical Chemistry*, **390**(2), 465–476.

Willigers, B. J. A., Mezger, K., and Baker, J., 2004. Development of high precision Rb–Sr phlogopite and biotite geochronology; an alternative to 40Ar/39Ar tri-octahedral mica dating. *Chemical Geology*, **213**(4), 339–358.

Zack, T., and Hogmalm, K. J., 2016. Laser ablation Rb/Sr dating by online chemical separation of Rb and Sr in an oxygen-filled reaction cell. *Chemical Geology*, **437**, 120–133.

Appendix D

Scientific Exchange Report (STSM)

Scientific Exchange Report (STSM)

Your Name:	**Jessica Alexandra Stammeier**
Your nationality:	**German**
Host Institution:	**University of Potsdam, Institute of Chemistry, Germany**
Dates of Visit:	**20-09-2015 to 03-10-2015**
Reference code:	**(ECOST-STSM-MP1202-011015-067657):**
Early Stage Researcher (less than 8 years after PhD)? Y / N	**Y**
Gender:	**Female**

Title: Understanding the formation of biomimetic organic / inorganic hybrid interfaces

Objectives:

- **F2 health/life science:**

Our project deals with the development of optimized calcium carbonate and calcium phosphate mineralization protocols in order to study reaction kinetics and mechanisms, as well as particular element and stable isotope exchange behaviour between ambient solutions and solids during the mineralization process.

- **F2_WG3a,b/ F2_WG13a,b:**

We examine how the conditions that prevail during mineral formation exert influence on mineral morphology both on an atomic-scale, i.e. unit-cell dimension, and on a microscopic scale. Also, we run a secondary set of experiments that is based on solution precipitation to determine the difference of mineral formation at hybrid interfaces and at purely inorganic conditions.

By investigating biomineral formation at hybrid interfaces we will get new insights in:

- (1) The application of (isotope-) geochemical signatures determined on the shells of marine calcifiers as archives for palaeo-climatological and -oceanographic reconstructions.
- (2) The parameters controlling the different shapes and compositions of minerals
- (3) The mineralization of bones, teeth and tendons as well as pathological mineralization e.g. the formation of dental calculus or arteriosclerosis, which is also associated with the precipitation of calcium phosphate and related minerals

We use Environmental Scanning Electron Microscopy (ESEM) as a high-resolution in-situ observational tool. This ensures, that we can analyse the minerals without disturbing their morphology or causing alteration, due to drying or solution effects. A small quantity of the minerals will furthermore be dried and analysed with ATR, XRD and TGA to explore their mineralogy and mineralization efficiency.

Brief description of the work:

We developed a set of precipitation experiments to optimize protocols for mineralization in polymer gels. The polymer gels were synthesized at the beginning of each week. They need to be prepared immediately prior to the experiments to avoid shrinkage due to drying of the gel. They were then exposed to the reacting and diffusing solutions and left to mineralize for 7 days. Moreover, the precipitation experiments from solution were conducted. In the second week, the preparation of the mineralized polymer gels were carried out in order to prepare them for further analysis.

Results :

1. Introduction:

Biominerals constitute hybrid organic-inorganic (HOI) materials that form at the organic-inorganic interface of various lifeforms. The HOI materials that are the main focus of this STSM are calcium phosphate (CP) phases. CP phases have a wide range of occurrences and uses ranging from products of biomineralization and

post-sedimentation in natural surroundings, add-ons in composites for tailored properties e.g. of cements and water treatment agents, to innovative medical-related products e.g. for remineralisation of teeth. To date, the mechanisms leading to mineral formation are not yet fully understood, with different models coexisting: Mineral formation (1) via direct, inorganic precipitation due to oversaturated aqueous solution, or indirectly through (2) microbial mediation or (3) replacement of carbonates. Mineral formation through microbial mediation can be further subdivided: (i) precipitation from microbially induced, local supersaturation or manipulation of pH; or (ii) mineralization within a gel-like biofilm produced by microbes living at the water sediment interface. The ploymer gels developed by Tauberts laboratory group represent a good approximation to these gel-like biofilms and can thus serve as a template for CP mineralization. Only few studies concentrate on the formation of CP (or calcium carbonate) in gel phases. Kniep and coworkers have shown that the reaction conditions and the gel composition may have a dramatic influence on the formation of fluorapatite[1], but similar data on hydroxyapatite is still not understood. The whole (natural) process of mineral formation is a complex interplay of numerous parameters. We are therefore concentrating on those parameters that can easily be controlled under laboratory conditions, i.e. temperature, pH, molar Ca/P ratio and availability of elements.

2. Experimental:

The overall experimental set-up is twofold and is summarized in table 1:

> (1) CPs are formed in the polymer gels.

> (2) CPs precipitate from solution using similar conditions.

Mineralization within the polymer gels was accomplished through double diffusion (see Figure 1). These experiments were set up in two groups:

> (1.A) Temperature was kept stable at 25°C during mineralization with a molar Ca/P ratio of 1:1.

> (1.B) Temperature was kept stable at 37°C during mineralization with a molar Ca/P ratio of 1:1

Both sets of gel mineralization experiments mineralize for 7 days. In these experiments only the parameters temperature (25°C & 37°C) and availability of elements were modified.

Figure 1 : Double-diffusion Gel-mineralization set-up. The small tube has a volume of 15 ml, the outer one 50 ml. The PO_4 component was always added on top of the gel. The Ca component was added from below, and remains the same for additional solutions (e.g. $MgCl_2$).

Calcium phosphate precipitation from solution (titration-experiments) was performed in four groups, each in which certain parameters were systematically modified:

> (2.A) Molar Ca/P ratio was kept stable at 5:3 = 1.67, to match that of hydroxyapatite, while the pH was adjusted over a range matching both modern and ancient seawater.

> (2.B) Molar Ca/P ratio was kept stable at 1:1, matching that of the gel-mineralization experiments while the pH was adjusted over a range. In this approach, the PO_4 component was provided using a Sörensenbuffer[2], mainly to match previous gel mineralization experiments conducted at the lab in Potsdam (unpublished data).

> (2.C) Both Molar Ca/P ratio and pH were kept stable, at 5:3 and pH 9 respectively. Additionally, certain elements were added to the solution. Each run was performed with 25 ml and 20 ml initial solution of the PO_4 component, to test whether the cations compete for the anion.

> (2.D) This group comprises only a single run, in which all parameters from the experiment at pH 9 from group B were adopted, but the Ca and PO_4 components were switched. This run was
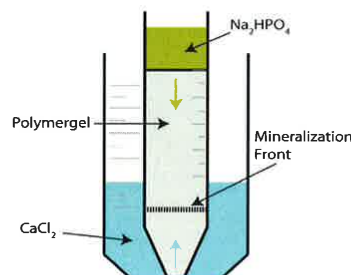
---

[1] e.g.: *K. Bleek, A. Taubert*, Acta Biomater. 2013, 9, 6283; *R. Kniep, S. Busch*, Angew. Chem. Int. Ed. Engl. 1996, 35, 2624; *H. Tlatlik, P. Simon, A. Kawska, D. Zahn, R. Kniep*, Angew. Chem. Int. Ed. 2006, 45, 1905.

conducted for demonstration only. By switching the initial solution in the titration beaker, the drop of Ca ions in the solution can be more easily monitored.

Table 1: Summary of the polymer gel mineralization experiments and titration experiments. *Mol* = molarity, *comp* = component.

Group	Samples	molarity	Comp. 1		molarity	Comp. 2		molarity	Comp. 3	Molar Ca/P
25°C	1.A.1	0.5 M	Na_2HPO_4	+	0.5 M	$CaCl_2$	+			1:1
	1.A.Mg	0.5 M	Na_2HPO_4	+	0.5 M	$CaCl_2$	+	0.01 M	$MgCl_2$	1:1
	1.A.Ba	0.5 M	Na_2HPO_4	+	0.5 M	$CaCl_2$	+	0.01 M	$BaCl_2$	1:1
	1.A.U	0.5 M	Na_2HPO_4	+	0.5 M	$CaCl_2$	+			1:1
37°C	1.B.1	0.5 M	Na_2HPO_4	+	0.5 M	$CaCl_2$				1:1
	1.B.Mg	0.5 M	Na_2HPO_4	+	0.5 M	$CaCl_2$	+	0.01 M	$MgCl_2$	1:1
	1.B.Ba	0.5 M	Na_2HPO_4	+	0.5 M	$CaCl_2$	+	0.01 M	$BaCl_2$	1:1
	1.B.All	0.5 M	Na_2HPO_4	+	0.5 M	$CaCl_2$	+	0.01 M	$NaSO_4,BaCl_2,MgCl_2$	1:1

Group	Sample		mol	Comp. 1			mol	Comp. 2		mol	Comp. 3	pH	Molar Ca/P
A	2.A.1	25 ml	0.3 M	Na_2HPO_4	+	20 ml	0.5 M	$CaCl_2$				9.5	5:3
	2.A.2	25 ml	0.3 M	Na_2HPO_4	+	20 ml	0.5 M	$CaCl_2$				9	5:3
	2.A.3	25 ml	0.3 M	Na_2HPO_4	+	20 ml	0.5 M	$CaCl_2$				8	5:3
	2.A.4	25 ml	0.3 M	Na_2HPO_4	+	20 ml	0.5 M	$CaCl_2$				7	5:3
	2.A.5	25 ml	0.3 M	Na_2HPO_4	+	20 ml	0.5 M	$CaCl_2$				6	5:3
B	2.B.1	25 ml	0.1 M	Sörensbuffer	+	20 ml	0.1 M	$CaCl_2$				7.4	1:1
	2.B.2	25 ml	0.1 M	Sörensbuffer	+	20 ml	0.1 M	$CaCl_2$				8	1:1
	2.B.3	25 ml	0.1 M	Sörensbuffer	+	20 ml	0.1 M	$CaCl_2$				6.4	1:1
C	2.C.1	20 ml	0.3 M	Na_2HPO_4	+	20 ml	0.5 M	$CaCl_2$	+	0.01 M	$MgCl_2$	9	5:3
	2.C.1.2	25 ml	0.3 M	Na_2HPO_4	+	20 ml	0.5 M	$CaCl_2$	+	0.01 M	$MgCl_2$	9	5:3
	2.C.2	20 ml	0.3 M	Na_2HPO_4	+	20 ml	0.5 M	$CaCl_2$	+	0.01 M	$BaCl_2$	9	5:3
	2.C.2.2	25 ml	0.3 M	Na_2HPO_4	+	20 ml	0.5 M	$CaCl_2$	+	0.01 M	$BaCl_2$	9	5:3
	2.C.3	20 ml	0.3 M	Na_2HPO_4	+	20 ml	0.5 M	$CaCl_2$	+	0.01 M	$NaSO_4$	9	5:3
	2.C.3.2	25 ml	0.3 M	Na_2HPO_4	+	20 ml	0.5 M	$CaCl_2$	+	0.01 M	$NaSO_4$	9	5:3
D	2.D.1	40 ml	0.3 M	Na_2HPO_4	+	40 ml	0.5 M	$CaCl_2$				9	5:3

Preliminary Results:

All gel mineralization experiments exhibit a mineralization front (compare Figure 2). In contrast to previous mineralization experiments the amount of minerals forming in the gels was more efficient. This was achieved by using higher concentrated solutions and only Na_2HPO_4 as phosphor source instead of Sörensenbuffer[2]. Initial mineralization was usually visible after 24 hours. From a purely visual point of view, no differences between the mineralizations at 25°C and at 37°C were observed. Most of the methods to analyze the gels including the minerals are time consuming and exceed the duration of this short-term stay. However, the samples from the mineralization run at 25°C were already dried, ground and handed in for XRD analysis. A small portion of the mineralization-front and the round-shaped particles were preserved for the ESEM analysis, which will be done in Graz, Austria.

The samples acquired from the experiments using a titrator are treated in a similar manner, although preparation is a bit different. We will apply the same methods to characterize these samples. After titration the solutions were filtered with a 5-13 μm filter and dried overnight in an oven at approx. 40°C. The dried samples were ground to a fine powder. The samples from the experiments conducted at pH 7-9.5 all dried into solid, ceramic like pieces. For all but three samples ATR spectra were collected. All samples could be identified as crystalline hydroxyapatite, except for samples 2.A.5 and 2.B.3 (pH 6 and pH 6.5, respectively). These two samples can be identified as the CP brushite (see figure 4).

---

[2] Phosphat-Buffer after Sörensen: A phosphate-buffer that consist of two 0.1 M solutions from (1) KH_2PO_4 and (2) Na_2HPO_4 $2H_2O$. These two components are combined to match a certain pH in the range 4.9 – 8.0.
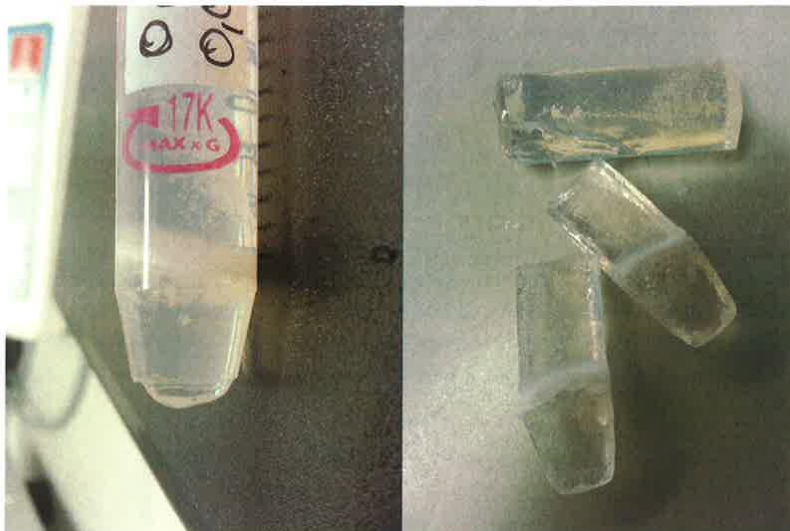
Figure 2: Mineralized polymer gel, sample 1.A.Ba. The minerals form as small particles of needle-like, sometimes star-shaped cumulates at the lower end of the gel. Above the main mineralization front, rounded particles scatter in streak-like formations.

Precipitation of a CP mineral phase always occurred instantaneous producing white slurry (Figure 3). The ATR analysis showed that the crystalline phase is hydroxyapatite, which always precipitates at pH 9.5-7. However, it is most likely that an amorphous precursor phase, ACP, precipitates first, which then subsequently crystallizes to hydroxyapatite. Crystallization of ACP to HAP occurs rapidly in the presence of water. Isolation of the amorphous phase can be achieved by filtering the solution and lyophilizing the filter cake instantly after precipitation. Therefore, no ACP is present after drying the samples at ca. 40°C overnight. For the same reason, no ACP is expected to be present in the mineralized gels. However, with ESEM we will be able to examine whether there is still some evidence of an amorphous precursor phase, as e.g. oddly shaped particles.
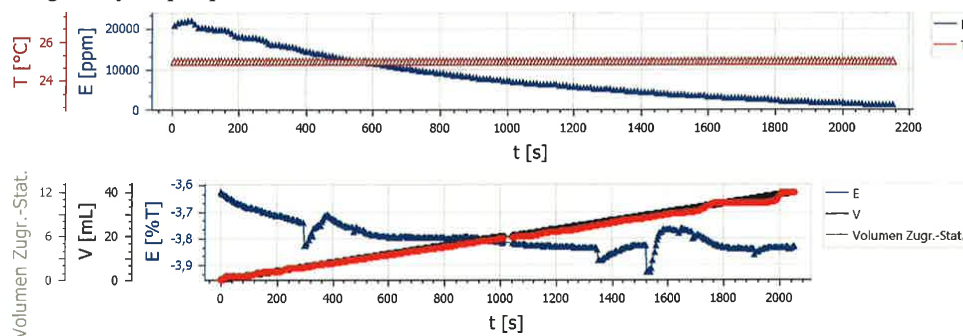

Figure 3: Log file of titration experiment 2.D.1: *E (ppm)* = Ca content in ppm; *V (ml)* = added PO_4 component; *E(%T)* = Transmission measured by the phototrode; *Volumen Zugr. – Stat.* = Added volume of base to stabilize the pH, unit in ml. The displayed value for the temperature (T) is not measured and was added to the display by the software. The free Ca content and (light-) transmission in the solution drops instantly with the addition of the PO_4 component, underlining that the reaction of Ca + PO_4 to hydroxyapatite (or the precursor phase ACP) is instantaneous.
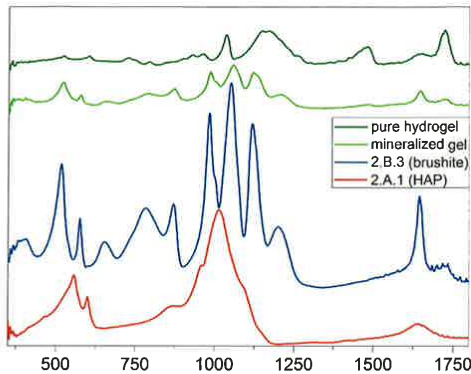
Figure 4: ATR spectra of selected samples. Y-axis: arbitrary units. Brushite precipitates from solution at pH <7, whereas apatite is formed at pH 7-9.5. The spectra of the hydrogels exhibit only peaks with lower intensity. The mineralized-gel spectrum resembles brushite. However, interference effects from the gel phase cannot be excluded. Therefore, XRD analyses are necessary to identify the mineral phase.

Outlook :

Subsequent to this short-term stay all pending methods will be applied to the samples prepared in Potsdam. Further, the set of experiments will be expanded for both temperatures, including elemental additions such as strontium and sulfate (SO_4). Further, a complementary set of experiments mineralizing calcium carbonates in the polymer gels will be conducted. In these mineralization experiments we will mainly focus on the mineral calcite, the trigonal variation of $CaCO_3$.

Further, due to thermodynamics temperature exerts an influence on kinetics, element mobility, solubility etc. It should therefore be tested whether a stable temperature, preferably matching the temperature used for gel mineralization, influences the results of the solution-precipitation in any way.

To investigate other processes of mineral formation, like replacement of carbonates, we will develop a protocol to conduct experiments in which gel-mineralized calcium carbonates are exposed to a PO_4-rich solution, without inducing shrinking or alteration of the gels.

During the STSM a collaboration of both working groups, Graz and Potsdam, was discussed and arranged. This collaboration combines the expertise of both partners: the laboratories in Graz (Technical University and Karl-Franzens-Universität Graz) will focus on the geochemistry, crystal analysis, isotope chemistry and analysis while the laboratory in Potsdam will focus on the synthesis and characterization of the hydrogels and biomineralization. The results of this project will then be published.

Acknowledgements:

I would like to thank A. Taubert for the opportunity to work in his lab; and his working group for kindly taking me in and helping me out. I am also very grateful to M. Przezdziak for assistance with the gel synthetization. Further gratitude is expressed to my supervisors D. Hippler and M. Dietzel. Last but not least, I would also like to thank Edith Stabentheiner for offering the use of the facilities at the Institute of Plant Sciences (KFU Graz).

Publication of Results:

I agree with the publication of the research results concerning this STSM on the HINT website (in the form of a short news article)

Signature:

Page to be completed by Host Institution:

Brief description of the nature of the collaboration:
Between different working groups, inside the same working group?
The collaboration took place between different workgroups. The special character of this collaboration is the fact that it took place between a chemistry and a geology research group. The two group leaders met a while ago on the occasion of a seminar at TU Graz and it turned out that there are many overlapping interests. The collaboration focused on joint experiments on the synthesis and mineralization of hydrogels that serve as model systems for biofilms. The visitor, Ms. Stammeier, was taught how to make the gels and how to perform the mineralization experiments and the host lab learned a lot about the geological significance of biofilms for geological processes. A further collaboration is planned and several samples are currently being made and exchanged between the laboratories.

Brief description of the host group and the work related to HINT scientific focus (F1-F5), objectives and the WGs and WGs Subtopics involved:

The host laboratory focuses on the synthesis and characterization of hybrid materials and has a long standing experience in biomineralization and related approaches. One of the central research areas is the development of biocompatible hybrid materials; this is a central theme in F2, especially **F2_WG3a,b / F2_WG13a,b**

Appreciation of the work performed during the visit related to the host group's subject of research:

Ms. Stammeier has been among the most successful visitors, has performed excellently and we are looking forward to a continued, interesting and very fruitful collaboration in the future. We would also be happy to have Ms. Stammeier again as a visitor in our laboratory.

Signed:
The original must be signed by host.

Prof. Andreas Taubert

Appendix E

Supplementary Material to Chapter 4

E.1 Methodology

For Mg isotope measurements bulk sample powders were leached in 3 mol l^{-1} HNO_3 for 24h at 70°C, capturing both carbonate fluorapatite (CFA) and carbonate phases (calcite and dolomite). This acid-soluble fraction was used for all consecutive elemental analysis and separations. The Mg fraction was purified with a two-step ion exchange chemistry using BioRad AG50-X12 and HNO_3 and HCl as eluent agents (see Stammeier et al. under review). Measurements were performed on a Plasma II MC-ICP-MS instrument (Nu Instruments, Wexham, UK) at the Graz University of Technology, Austria. Measurements were performed with standard-sample-bracketing (SSB) and are reported in the δ-notation as per mil (‰) deviation relative to DSM3. Repeated measurements of reference material Cambridge-1 (Romil Ltd., Waterbeach, Cambridge, UK) yielded -2.64 $\pm$ 0.10 ‰ for $\delta^{26}Mg$ and -1.36 $\pm$ 0.04 ‰ for $\delta^{25}Mg$ (2 SD, n=23), identical to previously reported values by e.g., Mavromatis, Meister, and Oelkers (2014).

E.2 Sample Description, Elemental and Isotope Information

TABLE E.1: Lithologic description of hand specimens and respective qualitative XRD results determine the major mineral phases, such as carbonate fluor apatite (CFA), quartz and calcite/dolomite. Note that the order of minerals does not reflect quantitative results. Magnesium content of the acid-soluble fraction (3 mol l^{-1} HNO_3) is as reported in Stammeier et al. (under review). Mg isotopes ($\delta^{25}Mg$ and $\delta^{26}Mg$ in ‰ DSM3) are reported as the mean of replica measurements with the uncertainty, expressed as 2s, referring to the standard deviation of the mean. In case the uncertainty of replica measurements is lower than the repeatability precision, values marked with *, the repeatability precision of ± 0.04 ‰ for $\delta^{25}Mg$ and ± 0.10 ‰ for $\delta^{26}Mg$ (2s, n = 23) for CAM-1 is reported.

Sample	Lithologic description	Mineralogy	MgO (wt. %)	$\delta^{25}Mg$ (‰DSM3)	±2s	$\delta^{26}Mg$ (‰DSM3)	±2s
KO 1	phosphatic chert	quartz, CFA, calcite	4.57	-0.21*	0.04	-0.45*	0.10
KO 2	phosphatic chert	quartz, CFA, calcite	0.89	-0.04*	0.04	0.06	0.12
KO 3.1	phosphatic chert	quartz, CFA, dolomite, calcite	2.37	-0.37	0.05	-0.77*	0.10
KO 3.2	phosphatic chert	n.d.	n.d.	0.25	0.04	0.48*	0.10
KO 04	cherty dolostone	quartz, CFA, dolomite	19.1	-0.34	0.09	-0.66	0.17
KO 6	phosphatic chert	quartz, CFA, dolomite, calcite	2.87	-0.23	0.22	-0.49	0.28
KO 9	phosphatic platy chert	quartz, CFA, dolomite, calcite	2.68	-1.16*	0.04	-2.12*	0.10
KO 10.1	contact dolostone/ phosphorite	quartz, CFA, dolomite, calcite	2.34	-0.59	0.05	-1.15*	0.10
KO 10.2	phosphorite	n.d.	n.d.	-0.65*	0.04	-1.24*	0.10
KO 11	phosphorite	quartz, CFA, dolomite, calcite,	2.98	-1.01*	0.04	-1.91*	0.10
KO 12	dolomitic phosphorite	quartz, CFA, dolomite, calcite	5.99	-0.66*	0.04	-1.42*	0.10
KO 13.1	phosphatic flat pepple conglomerate	quartz, CFA, dolomite, calcite	5.25	-0.90*	0.04	-1.85*	0.10
KO 13.2	phosphatic flat pepple conglomerate	n.d.	n.d.	-0.90	0.06	-1.69*	0.10

n.d. = not determined

E.3 Petrography

The samples predominantly represent granular phosphorites (P_2O_5> 18 wt. %) consisting of various phosphatic grains of different size. According to Trappe (1998) these granular phosphorites can be classified as well-sorted phos-grainstones and poorly-sorted phos-rudstones. Phosphatic grains include phosphatic intra clasts (Inset A) and peloids (Inset B), as well as coated grains, such as oncoids and ooids. Scanning electron microscopy (SEM) images of phos-peloids and ooids highlight the preservation of well-defined CFA nano-crystals indicating an almost pristine internal structure. Within the laminae of coated grains, the fibrous CFA nano-crystals can be radially arranged (Inset C) or as spherulitic, botryoidal aggregates within phos-peloids (inset D). The matrix of these granular phosphorites can be calcite, dolomite or chalcedony.

In most samples, the dolomite matrix forms a mosaic structure of anhedral grains (Inset A). Petrographic observations indicate depositional cycles of reworking of primary phosphate fabrics, the so-called Baturin cycling (Baturin, 1971) and thus phosphorite formation in a shallow-water, moderately to high-energy environment.
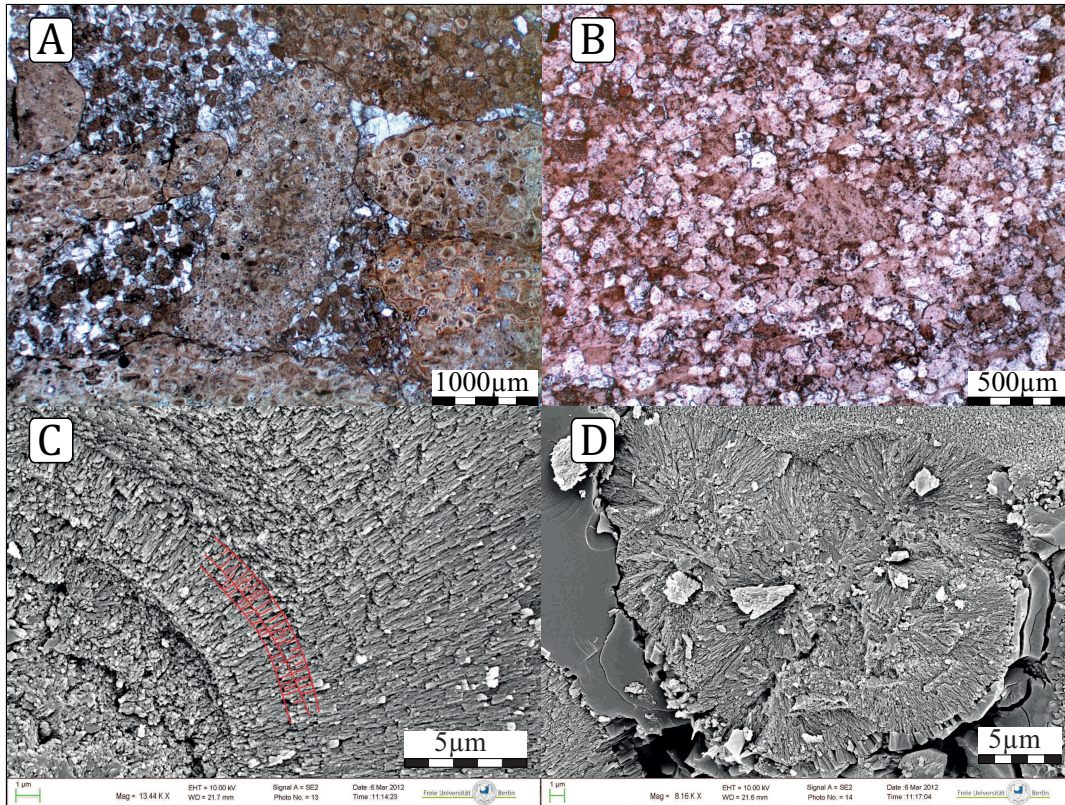

FIGURE E.1: Inset A: Poorly sorted flat-pebble phos-rudstone (KO 13) with a sparry dolomite matrix. Inset B: Well-sorted phos-grainstone, with few coated grains and sparry calcite cement (KO10). Inset C: Detailed SEM image of a phos-ooid illustrating the well-preserved, fibrous CFA crystals radially-arranged in each ooid laminae (KO13). Inset D: SEM image of the internal structure of a phos-peloid showing spherulitic, botryoidal aggregation of fibrous CFA crystals (KO13).

References

Baturin, G. N. (1971). "Stages of phosphorite formation on the ocean floor". In: *Nature Physical Science* 232. DOI: 10.1038/10.1038/PHYSCI232061A0.

Mavromatis, V., P. Meister, and E. H. Oelkers (2014). "Using stable Mg isotopes to distinguish dolomite formation mechanisms: A case study from the Peru Margin". In: *Chemical Geology* 385. DOI: 10.1016/j.chemgeo.2014.07.019.

Trappe, J. (1998). *Phanerozoic phosphorite depositional systems : a dynamic model for a sedimentary resource system.* Springer, p. 316.